Mechanical behavior of heterogeneous composite materials reinforced by fiber glass mesh

Pascale Saba

université PARIS-SACLAY

Mechanical behavior of heterogeneous composite materials reinforced by fiber glass mesh

Mécanique des matériaux composites hétérogènes à base cimentaire renforcés par des grilles de fibre de verre

Thèse de doctorat de l'université Paris-Saclay

École doctorale n° 579, Siences mécaniques et énergétiques, matériaux et géosciences (SMEMAG)
Spécialité de doctorat: Génie civil
Graduate School : Sciences de l'ingénierie et des systèmes.
Référent : ENS Paris-Saclay

Thèse préparée dans l'unité de recherche **LMPS - Laboratoire de Mécanique Paris-Saclay (Université Paris-Saclay, CentraleSupélec, ENS Paris-Saclay, CNRS)**, sous la direction de **Farid BENBOUDJEMA**, Professeur des Universités, le co-encadrement de **Tulio HONORIO DE FARIA**, Maître de conférences, la co-supervision de **Xavier BRAJER**, Chef de groupe Saint-Gobain Recherche Paris

Thèse soutenue à Paris-Saclay, le 03 juin 2022, par

Pascale SABA

Composition du jury

Membres du jury avec voix délibérative

Aveline Darquennes Professeure des Universités, Institut National des Sciences Appliquées de Rennes	Présidente
Laurie Lacarrière Professeure des Universités, Institut National des Sciences Appliquées de Toulouse	Rapportrice & Examinatrice
Nicolas Burlion Professeur des Universités, École Polytechnique Universitaire de Lille	Rapporteur & Examinateur
Barzin Mobasher Professeur, Arizona State University	Examinateur
Marco Di Prisco Professeur, Politecnico di Milano	Examinateur

THESE DE DOCTORAT
NNT : 2022UPAST084

Remerciements

Quel est le chemin le plus rapide entre un point A et un point B ? La réponse la plus évidente est « une ligne droite ». Cette ligne évoque le chemin tracé d'un programme ambitieux et détaillé que l'on se fixe avant la ligne de départ. Le futur doctorant est confiant : tout va bien se passer et tout va se dérouler comme prévu ! La première année démarre en douceur avant de rencontrer le premier obstacle, puis le deuxième, puis une pandémie mondiale (tout va bien !). La ligne droite se transforme vite en une fonction polynomiale à plusieurs inconnues. A tous ces obstacles : Merci ! Vous avez fait de moi ce que je suis aujourd'hui.

Mon aventure à l'ENS a commencé à Cachan au LMT. Je me souviens bien du premier jour de stage de fin d'étude quand je suis entrée pour la première fois dans les locaux du laboratoire. A l'accueil se dresse un « BAR » -oui oui un bar-, et une belle machine à café. Drôle d'entrée pour ce laboratoire scientifique. J'ai vite compris, comme tout nouvel entrant dans ces lieux, que c'est ici où se déroule la vie du laboratoire : les discussions autour d'un café, les événements de convivialité, les pauses déjeuner, les fameux pots tous les jeudis après les séminaires, les pots de thèses... Ne vous détrompez pas, c'est ici que les équations les plus complexes sont résolues ! J'aimerais donc commencer par remercier chaleureusement chaque personne que j'ai croisée dans ce lieu.

J'adresse mes remerciements à tous les membres du jury. Au Professeur A. Darquennes, qui m'a fait l'honneur d'avoir accepté de présider le jury. Aux Professeurs N. Burlion et L. Lacarrière d'avoir accepté d'être rapporteurs, d'avoir pris le temps de lire mon mémoire et d'avoir partagé leurs avis, commentaires et interrogations à la fois stimulants et constructifs. To the Professors B. Mobasher and M. Di Prisco, who made me the honor to come from across the Atlantic and from Italy, respectively, to be part of my jury. Je vous remercie tous pour le grand intérêt que vous avez manifesté pour mon travail ainsi que pour toutes les discussions enrichissantes que nous avons pu avoir pendant ma soutenance.

Je souhaite ensuite remercier du fond du cœur mon directeur de thèse Farid, tu as été pour moi une source d'inspiration autant sur le plan scientifique que personnel. Tu m'as soutenue pour surmonter les obstacles et tu as été un pilier scientifique qui m'a appris à questionner les limites de chaque théorie et de chaque méthode. J'admire en particulier ta patience en essayant de me remonter le moral : les blagues (réussies ? parfois !), le bon chocolat belge, les bonnes pâtisseries françaises... enfin la liste est longue. Ta présence, ton aide et ta disponibilité étaient toujours inconditionnelles. J'adresse également mes remerciements chaleureux à mon encadrant Tulio, dont je crois être la première doctorante. Toujours disponible, souriant et de bonne humeur, travailler et échanger avec toi était toujours très agréable. Tu es efficace

et tu aimes l'efficacité, c'est souvent grâce à toi que nous avons pu tenir les dates limites des diverses soumissions. Merci du fond du cœur d'avoir été là.

Mes remerciements s'adressent également à mes encadrants industriels de Saint-Gobain pour m'avoir fait confiance sur ce projet et donné l'opportunité d'intégrer leurs équipes. Mes remerciements s'adressent à O.A. Mahmood et L. Garnier avec qui j'ai commencé ce projet depuis mon stage de fin d'étude. Vous m'avez accueillie et soutenue pour naviguer dans le monde industriel. Je remercie également X. Brajer et C. Wable, vous avez toujours réussi à m'accorder du temps malgré vos agendas chargés et à veiller aux atteintes des objectifs industriels. Merci à R. Gy, vous avez toujours été présent pendant les réunions à Saint-Gobain Recherche. Votre expertise, vos conseils et votre bienveillance ont été des leviers nécessaires pour le bon déroulement du projet.

Mes remerciements vont aussi à l'ensemble des ingénieurs et techniciens du centre d'essai et du département de génie Civil. Merci particulièrement à Xavier Pinelli, Rémi Legroux, Benjamin Smaniotto et Olivier Rateau pour votre aide et votre suivi sans faille pendant mes nombreuses campagnes expérimentales.

Comment ne pas remercier mes amis du laboratoire, Livio, Arianne, Nicolas, Francesco, Sebastien, Justin, Achraf et bien d'autres ! Chaque jour était bien plus agréable grâce à votre présence. Merci pour toutes les discussions, les sorties, les rigolades, les moments précieux qu'on a partagés ensemble. Et puis Aya, mon binôme et ma complice, je garderai à jamais les souvenirs de nos discussions autour des manifestations et de la situation du Liban en buvant un thé ou un café, la décoration de notre bureau à Saclay, nos vidéos et photos... Nous avons pleuré ensemble, rigolé ensemble, et surtout traversé les trois années de thèse ensemble. Merci pour tout !

A toutes mes copines, Leila, Zamane, Lara, Rawan, Gaby, Saly et Rima. Merci pour votre soutien permanent malgré des longs mois sans vous parler. Vous n'avez jamais manqué de me montrer votre amour quand j'en avais le plus besoin ! Merci.

A ma belle-famille, Catherine, Éric et Elsi, vous m'avez accueillie les bras ouverts dans votre famille. Avec vous j'ai découvert la culture, les traditions et la gastronomie françaises ainsi que des jolis coins de la France. Avec vous j'ai partagé beaucoup, presque ma vie en France. C'est agréable de savoir que j'ai une deuxième famille sur qui je peux compter quand ça ne va pas et avec qui je peux trinquer quand ça va très bien !

A mon chéri, Natan, précieux sont nos moments ensemble ! Avec toi j'ai partagé le meilleur comme le pire. Merci tout simplement d'être présent, à mes côtés, toujours.

Enfin, à mes parents, mon frère et ma sœur ...

أبي، أمي، أخي و أختي، أشبعتموني حباً لا متناهياً، غذيتم فيّ قوةً وثقة. أنتم قدوتي منذ صغري. لن تستطيع الكلمات أن تبوح بما في داخلي. لذا سأكتفي بالقول: شكراً و أحبكم.

Résumé

De nos jours, l'énergie est devenue un besoin fondamental dont la demande ne cesse de croître. Cette dernière est essentielle pour le bien-être et la survie des humains et sa disponibilité est cruciale pour l'économie et la croissance nationales. Les crises sociales, géopolitiques et écologiques se traduisant respectivement par un manque de confort thermique dans les habitations combiné à des factures d'énergie coûteuses pour les ménages à faible revenu, la dépendance énergétique notamment en termes d'energies fossiles, et le réchauffement climatique, exigent une réduction importante de la consommation d'énergie. En France, les systèmes de chauffage des bâtiments représentent 45% de la consommation totale d'énergie et sont responsables de 27% des émissions de gaz à effet de serre. L'isolation thermique dans laquelle s'inscrit l'Isolation Thermique par l'Extérieur (ITE) permet de réduire considérablement la consommation d'énergie ainsi que les émissions de CO_2 tout en augmentant le confort thermique des habitants et en réduisant leur facture d'énergie. Le mortier de façade renforcé par la grille de fiber de verre est utilisé comme couche de protection externe des ITEs. Cependant, de nombreux défauts peuvent compromettre la performance des ITEs, en particulier la fissuration du mortier de façade. Le mortier à base cimentaire subit des déformations chimiques, thermiques et hydriques qui, lorsqu'elles sont restraintes, induisent des contraintes qui peuvent atteindre la résistance en traction du matériau conduidant à la fissuration du mortier. La grille de fibre de verre est proposée comme une solution pour la fissuration. Le comportement du mortier composite renforcé est une combinaison du comportement de chacun de ses composants, le mortier et la grille de fibre de verre. Le premier est un matériau qui évolue chimiquement et qui peut être affecté par son environnement comme son état hydrique. Le comportement du mortier de façade est donc étudié en fonction de son âge et ses conditions de conservation parmi d'autres paramètres. D'autre part, cette étude vise à comprendre les mécanismes de renfort de la grille de fibre de verre dans le mortier vis-à-vis de la fissuration. Des essais de flexion 3 et 4 points sont réalisés in-situ dans le tomographe à rayons X et plusieurs paramètres de renforcement sont considérés. La tomographie permet de dévoiler le rôle de la grille de fibre de verre sur la localisation et la propagation des fissures dans le mortier renforcé.

Abstract

In our times, energy has become essential for the welfare and the survival of humans and its availability is crucial for the national economy and growth. The social, geopolitical, and ecological, crises reflected respectively in the lack of thermal comfort in homes combined with expensive energy bills of the low-income households, the energy dependency especially in terms of fossil fuels, and the global warming demand the reduction of the energy consumption. In France, the heating systems of buildings represent 45% of the total energy consumption and are responsible for 27% of greenhouse gas emissions. Thermal insulation including the External Thermal Insulation Composite System (ETICS) has a big impact on the energy consumption and CO_2 emissions increasing, at the same time, the thermal comfort of the residents and decreasing their energy bills. The fiberglass mesh reinforced rendering mortar is used as the external protective layer of ETICS. Many defects may attain the ETICS including the cracking of the rendering mortar. These defects may impair the thermo-mechanical performance of the ETICS. The cement-based mortar undergoes chemical, thermal, and hygral strain which, when restrained, cause stress that may attain the tensile strength of the material and cause the mortar cracking. The fiberglass mesh is proposed as a solution for cracking. The behavior of the composite reinforced mortar is a combination of the behavior of each of its components, the mortar and the fiberglass mesh. The former is a chemically evolving material which may also be affected by other conditions such as its hygral conditions. The behavior of the rendering mortar is thus investigated with respect to its age and its curing conditions among other parameters. In a second part, going further in the comprehension of the reinforced mortar mechanical behavior, this study focuses on the fundamental understanding of the reinforcement mechanisms of the fiberglass mesh within the mortar with respect to cracking. X-ray tomography in-situ 3-point and 4-point bending tests are carried out and several reinforcement parameters are considered. The tomography scans enable unveiling the role of the glass fiber mesh on crack localization and crack propagation in reinforced mortar. This work provides physical insights on the reinforcement mechanisms of fiberglass mesh on mortars contributing to the optimization of the cement-based reinforced composites especially in ETICS.

Contents

List of Figures

List of Tables

Chapter 1

Introduction

1.1 Ecological, geopolitical, and social context

In the midst of an ecological, a geopolitical and a social crises, energy consumption is taking a central place in the debate. The societal, economic and environmental issues related to the comfort of humans are significant. Energy has become a basic need to which the demand is constantly increasing playing an important role not only for the welfare and survival of citizens, but also for the nations' development. The national economy and growth depend largely on the availability of energy that must be accessible at a competitive price and at a regular, uninterrupted, uniform, and stable supply. Recent national and international news, unfortunately, show that energy strongly affects purchasing power and plays a strategic role in international conflicts. To respond to the major crises of our times (the global warming, the energy dependency especially in terms of fossil fuels, and the energy bills that weigh heavily on the purchasing power), reducing the energy consumption is key. As said by former French Minister of Ecology, Nathalie Kosciusko-Morizet: "The best energy is the one we do not consume, and moreover it can be the cheapest". According to the plan of energetic renovation of the buildings [MTE, 2021], the fight against climate change to achieve carbon neutrality by 2050 requires a redoubling of efforts to reduce energy consumption and develop renewable energies in all sectors: buildings, transport, agricultural, industrial and tertiary production activities, etc. Improving the energy performance of the building stock involves reducing the energy needs of buildings, using efficient systems to limit energy consumption and finally the deployment of renewable energies. Only a combined approach to these three areas will make it possible to achieve the set objectives. At the national level, the building sector represents 45% of final energy consumption and 27% of greenhouse gas emissions [MTE, 2021]. On the European level, the Europe's building stock is responsible for 40% of total energy consumption and 36% of CO_2 emissions [EAE, 2021]. Today, 7 million homes are poorly insulated and 14% of French people are cold in their homes. In response to these numbers, the government wanted to accelerate the energy renovation of buildings. The objective is twofold: to lower energy bills and reduce energy consumption in buildings [MTE, 2021]. Over the last 5 years, the government planned to deploy around 4.2 billion euros aiming to renovate 175 thousand housing units per year belonging mainly to modest income households [MTE, 2021].

A theoretical study [Palacios-Munoz et al., 2019] investigated the impacts of 4 solutions along a 100 year-time period applied on an existing building of 50 years old: (i) passive energy refurbishment (PR), (ii) standard energy refurbishment (SR), (iii) demolition plus standard new building (SD&N), and (iv) demolition plus passive new building (PD&N). The authors conclude that PR is one of the best solutions from the CO_2 emissions perspective. Depending on the scenario, the quantity of CO_2 (eq/m^2 ·year) emitted is equal to about 33 in the case of PR, 36 in the case of SR, 40 in the case of SD&N, and 38 in the case of PD&N. Another study [Galimshina et al., 2021] shows that for a building with higher heating demand, the envelope of a building needs to be renovated regarding life cycle cost analysis and greenhouse gas emissions. However, for a building with lower heating demand, the most robust and optimal solution is the heating system replacement. The existing thermal regulation by element requires the installation of products with performances higher than the minimum characteristics when the owner decides to replace or install an insulating element [MTE, 2020]. The renovation of buildings in terms of thermal insulation concerns two categories of elements to be renovated: (i) opaque surfaces such as walls, roofs and floors, (ii) and glazed surfaces such as windows. Several types of thermal insulation exist for the renovation of the external walls of a building one of which is External Thermal Insulation Composite System (ETICS). ETICS are also known as Exterior Insulation Finishing System (EIFS) and as Exterior Wall Insulation (EWI).

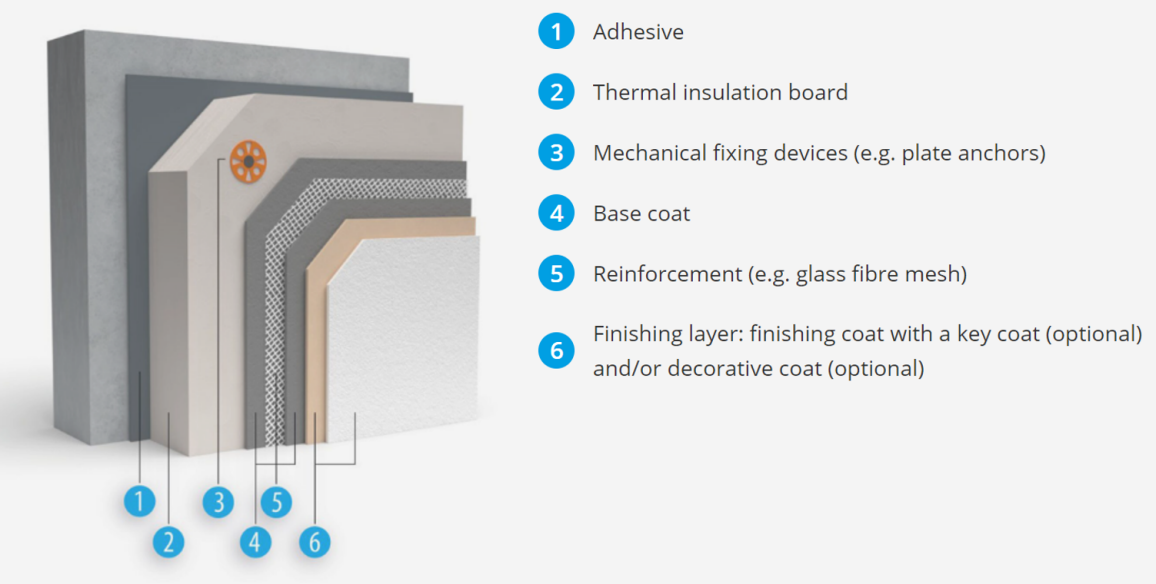

Figure 1.1: Typical system components in ETICS [EAE, 2021].

The popularity of the ETICS technology grew due to its advantages regarding other techniques of insulation. ETICS guarantees the reduction of the thermal bridges and greater thermal comfort due to the higher interior thermal inertia, providing a finished appearance similar to the traditional rendering [Barreira and de Freitas, 2015]. From the construction point of view, ETICS allows thinner exterior walls and increases the facades' durability. Three very relevant aspects in the construction industry must be added to the advantages above: low cost, ease of application, and the possibility to be installed without disturbing the building's

dwellers, which is particularly important in refurbishment [Barreira and de Freitas, 2015]. ETICS allows saving up to 30% of the building's energy consumption by limiting heat loss through the walls, which represent on average 25 to 30% of total losses (example of a house dating from 1975 without insulation, according to the *Agency for the Environment and Energy Management*), but also reduces the 5 to 10% of heat losses corresponding to thermal bridges (junctions with joinery and intermediate floors). It is therefore strongly encouraged by the public authorities [Boughriet, 2018]. The components of an ETICS are shown in figure 1.1. Elements 4 and 5 combined form the fiberglass mesh reinforced rendering mortar that protects the insulating system and that will be the center of this study.

1.2 Industrial context

Fiberglass fabric market was valued USD 8.74 Billion in 2016 and is projected to reach USD 13.48 Billion by 2022, at a Compound Annual Growth Rate (CAGR) of 7.62% between 2017 and 2022 [MaM, 2017]. The use of fiberglass fabric is gaining high importance in the wind energy, transportation, electrical and electronics, marine, construction, and aerospace and defense, among other sectors. In the construction sector, several geometries, shapes and dimensions of fiberglass mesh are found in the market offering reinforcement solutions for a very wide range of applications such as reinforcement for facades, interior wall, profile, marble and mosaic, and for the rendering mortar covering the ETICS.

However, many defects may weaken the performance as well as the market of ETICS. A literature review [Kvande et al., 2018] shows several cases of defects in ETICS systems depending on the country. In Sweden, North America and Germany, moisture defects and mold growth were reported in timber frame walls [Samuelson, 2002, Samuelson et al., 2007, Köhler, 2008] since the end of the 1980s. Currently, ETICS durability and moisture problems are studied even in countries around the Mediterranean sea, even if they encounter less precipitation than Nordic countries. A field investigation on 61 buildings with ETICS defects has been realized in the period between 1993 and 2017. It shows that the rendering is the main source of defect (figure 1.2). The defects are related to the reinforcing mesh (use of insufficient quantity of reinforcement, placement of the mesh touching the insulator or extending too far out the render layer) and the mortar (insufficient thickness, faulty render mix, too much shrinkage or thermal strain). Other causes can also be incorrect placement conditions (direct sunlight, too much wind exposure, very low temperatures). Similar observations have been recorded in France [AQC, 2019].

Cracking in the fiberglass mesh reinforced mortar is investigated in this study. The visible cracking is critical because of two main reasons: (i) From the technical point of view, the cracks decease the waterproofing capacity of the rendering. The eventual water penetration inside the cracks may cause the insulator to lose its thermal properties affecting the efficiency and the durability of the system. (ii) from the marketing point of view, visible cracking on the facades increases the complaints rate and affects negatively the sales volume. Oriented and non-oriented cracking and visibility of joints are among the main anomalies encountered [Amaro et al., 2013, Nilica and Harmuth, 2005, Pereira et al., 2018]. The glass

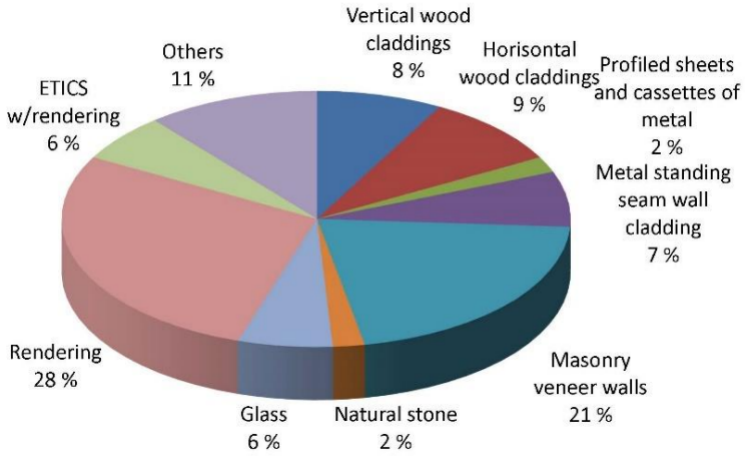

Figure 1.2: Distribution of defect cases to external walls above ground depending on the type of cladding. Taken from SINTEF Building Defect Archive (period 1993–2002 [Lisø and Kvande, 2007].

fiber mesh is proposed as a solution for cracking known, among the professionals of the sector, for decreasing the crack width. However, the application of the the fiberglass mesh is still empirical and mainly based on the feedback and trial-and-error from construction sites. The absence of regulations for the fiberglass mesh application in ETICS shows that more research is needed in order to establish the good practices, especially regarding the choice between mesh types and the design of new products thus affecting negatively the market volume.

This PhD project is part of a larger R&D vision that aims:

- The prevention of cracking in rendering mortars under environmental cyclic loading.
- The tailored choice of reinforcement types according to the application and the loading.
- The development of new products for new applications such as structural reinforcement of walls.
- The development of experimental and numerical tools in order to design more performing products.

1.3 Scientific challenges and objectives of the study

Fiberglass mesh reinforced rendering mortar is used as a protection layer for ETICS. It is a composite material constituted by the cement base heterogeneous mortar and the fiberglass mesh. As all contentious materials, the rendering mortar undergoes continuous chemical, thermal, and hygral changes causing strains which when restrained induce stress that can attain the tensile strength of the material causing it to crack.

Two types of zones can be differentiated in a rendering mortar on a facade:

- Stress concentration zones such as the window corners, the thermal joints, and the wall corners shown in figure 1.3. These zone are considered as geometrical singular zones where stress is localized and where cracking may be induced.
- Plane zones on the other hand are the zone without structural geometrical singularities. In the plane zones, the stress concentrations are governed on the microstructure of the material. Thus the cracking in the rendering mortar may be initiated on two different levels, on the structural level in the stress concentration zones or on the microstructural level in the plain zones.

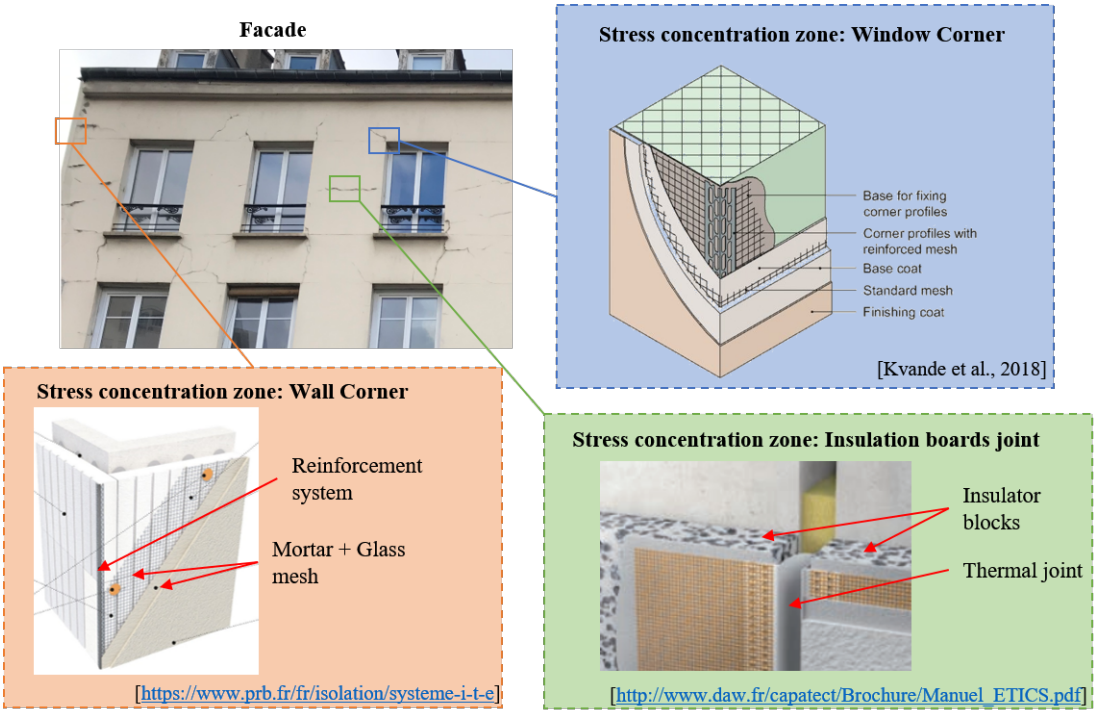

Figure 1.3: Stress concentration zones on a facade inducing localized cracking.

On the microstructural level, cracking may be induced by the heterogeneities of the material (i.e. the sand grains, the pores, and the fiberglass mesh shown in figure 1.4). When the strains of the mortar are restrained, either by the substrates that constitute the ETICS (i.e. the insulator and the wall shown in figure 1.4) or by the rigid inclusions in the mortar (i.e. the sand grains and the fiberglass mesh), stress concentrations are induced and may lead to cracking. The behavior of the fiberglass mesh rendering mortar is a combination of the behaviors of two materials: the mortar and the fiber glass mesh. As shown in figure 1.4, both are heterogeneous materials with complex microstructures. However, the interface between both materials will play an important role as well in the overall behavior of the composite.

This project aims to clarify the role that plays a fiberglass mesh in the rendering mortar. Since the behavior of the mortar take an important place in the behavior of the composite, and since it is a constantly changing material due to its chemical evolution and to the hygral and thermal exchange with the environment, the behavior of the rendering mortar is investigated and the effect of several parameters such as relative humidity and age are considered. In addition, to understand the cracking mechanisms in the reinforced rendering mortar, and to clarify the role of the fiber glass mesh and its reinforcing mechanisms within the mortar and with respect to cracking, mechanical tests are carried out on fiberglass mesh reinforced mortar samples. The mechanical tests are designed to be representative of either the stress concentration zones or the plain zones in the mortar. In addition, the tests are carried out in-situ X-ray computed tomography to investigate the 3D volume of samples and visualize cracking within the specimens rather than the surface.

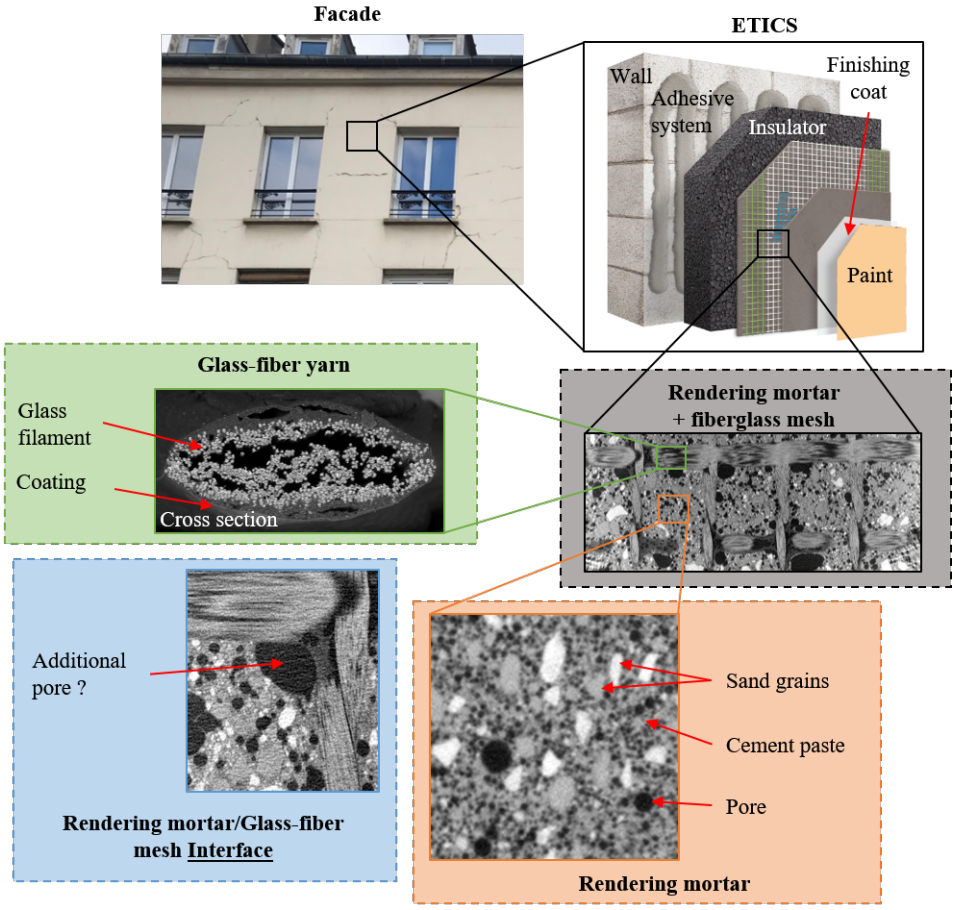

Figure 1.4: Rendering mortar in ETICS: a multi-scale heterogeneous composite material.

1.4 Outline

This manuscript is divided in two main chapters followed by the conclusion:

- Chapter 2 investigates the behavior of the rendering mortar from its early-age to its mature age. Early measurements including weight loss, shrinkage strains, and isothermal calorimetry to track the heat generation of the hydration reaction are carried out to investigate the early-age behavior of the mortar. On the other hand, its mechanical behavior is investigated by 3-point bending. The effect of several parameters such as drying, rehumidification and age in the mechanical properties of the mortar are considered.

- Chapter 3 studies the cracking mechanisms of the reinforced rendering mortar the role of the mesh with respect to cracking, thus the reinforcement mechanisms of the fiberglass mesh within the mortar. In-situ X-ray tomography 3-point and 4-point bending mechanical tests are carried out. The effect of several parameters such as the type of mesh, the direction of the mesh within the specimens, and the distance between the mesh and the tensile surface are considered.

- Finally, chapter 4 will discuss the main conclusions of this work and set perspectives for further research and industrial development.

Chapter 2

Behavior of the rendering mortar

The fiber-glass reinforced mortar used in ETICS is a cement composite constituted of the mortar and the fiber-glass mesh. The global behavior of the composite material is a combination of the behavior of both, the mortar and the fiber-glass mesh, as well as the interaction between the two materials. For this reason, although the fiber-glass mesh is in the center of the study, the behavior of the mortar is also studied and is the topic of this chapter.
Being cementitious materials, rendering mortars are in a continuous interaction with the environment. When the relative humidity of the surrounding environment changes, the internal hygral state of the mortar also changes leading to a modification of its mechanical properties.

2.1 Introduction

As mentioned in the introduction of this manuscript, this study focuses on the mechanical behavior of the fiber glass reinforced rendering mortar used as a protective layer for the insulator in ETICS. The behavior of this composite material is a combination of the behavior of each of its components (i.e. the rendering mortar and the fiber-glass mesh), as well as the interaction between them. For this reason, it is important to understand the behavior of the rendering mortar used in ETICS.

ETICS are assessed by the EOTA ETAG 004 certification test [EOTA, 2013] which includes a series of tests to verify a demanding level of characteristics including (i) mechanical resistance and stability, (ii) safety in case of fire, (iii) hygiene, health and environment, (iv) safety in use, (v) protection against noise, (vi) energy economy and heat retention and (vii) aspects of durability and serviceability. The hygrothermal cycles and particularly the heat and rain cycles in figure 2.1 are one of the tests in the EOTA ETAG 004 certification during which temperature variations (including increases up to 70°C simulating a severe heat condition) are followed by water sprays simulating rain accompanied by a sharp temperature decrease. All 80 cycles of this test represent a portion of the environmental conditions experienced by the ETICS that can lead to cracking in the rendering mortar protecting the insulation. However, the internal humidity of the rendering mortar will also change. Its internal relative humidity will therefore vary during the 80 cycles of the test affecting it mechanical behavior.

Like all cementitious materials, rendering mortars are subject to cracking. The interactions with the environment changing temperature and relative humidity lead to thermal and hygral strains, which when restrained, may lead to stresses that can attain the tensile strength of the material causing then the mortar cracking, thus affecting it's mechanical properties.

This chapter investigates the behavior of the rendering mortar from its early-age to its mature age. This chapter is presented as follows. First, a review of the literature is carried out focusing on the drying and drying shrinkage mechanisms in cementitious materials, the influence of drying on the cracking, thus on the mechanical behavior of cementitious materials, as well as the influence of additives such as polymer latex and cellulose ethers on the behavior of mortars. Then, the experimental characterization of the rendering mortar is presented in two parts: (i) early measurements including weight loss, shrinkage strains, and isothermal calorimetry to track the heat generation of the hydration reaction; and (ii) the mechanical behavior of the rendering mortar investigated by 3-point bending. The effect of several parameters such as drying, rehumidification and age in the mechanical properties of the mortar are considered.

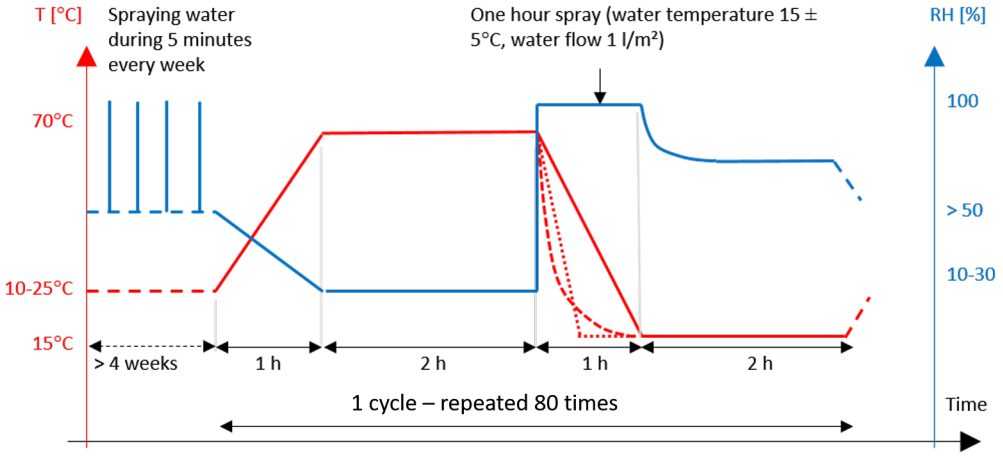

Figure 2.1: Certification test EOTA ETAG 004: heat and rain cycles.

2.2 State of the art

A mortar is a heterogeneous cementitious material composed of the cement paste, sand grains and porosity at its mesoscale. Depending on their use in the field of structures and buildings, performance specifications regarding certain properties such as viscosity, adhesion, and mechanical resistance should be met [Coussot, 2005]. For rendering mortars, used as a protection layer in ETICS for example, a certain workability that can facilitate their application is demanded, as well as a sufficient adherence to the vertical substrate and a mechanical resistance to the changing temperature and relative humidity of the environment is required. For this reason, mortars are often adjuvanted with additives such as latex polymers and cellulose ethers that impact their fresh state as well as their hardened state properties.

The hierarchical porous nature of the mortar makes it a material prone to drying and resulting repercussions (drying shrinkage and cracking). The drying process of porous structures are complex and can induce several mechanisms within the structure, such as drying shrinkage, affecting the behavior of the material.

In this section, a brief review of the literature is elaborated. The drying and the shrinkage mechanisms are detailed. The drying effect on the mechanical behavior of cementitious materials is investigated according to several authors. Last but not least, a review of the additives that are often used in mortars as well as their impact on the material's behavior is established.

2.2.1 Porous structure of cementitious materials

It is important to look at the porous structure of the material. Pores are the place of "storage" of the water available within the material. Their structure has a strong influence on the properties of the material in general, and on the natural desiccation in particular. A porous structure is characterized by the total volume of porosity, the distribution of pore sizes, and the porous network features such as the tortuosity, the constrictivity and the connectivity. These parameters, although difficult to characterize, play an important role in the drying process [Shen and Chen, 2007, Van Brakel and Heertjes, 1974]. Two cement-based materials with equal porosity might not have the same transport properties whether the porosity is connected or not or depending on the pore size distribution. Various methods are available to characterize the porosity including porosimetry (NF P18-459) or mercury porosimetry (ISO 15901-1: 2016). These two methods allow to quantify the total volume of pores. The second has the advantage of giving a qualitative pore size distribution curve. Various classification norms separate the pores according to their size. In the International Union of Pure and Applied Chemistry (IUPAC) classification of pore size, the micropore width is taken to not exceed about 2 nm, the mesopore width to be in the range 2–50 nm and the macropore width to be above about 50 nm [Sing, 1991]. The different pore classes described above will have a different influence on the behavior of the cementitious material. The macropores and the mesopores will influence the mechanical behavior and transfer properties, while the micropores will play a role in the long-term mechanisms such as shrinkage and creep [Kumar and Bhattacharjee, 2003].

2.2.2 Drying mechanisms in porous materials

In porous materials, such as cementitious materials, the moisture transfer is caused by relative humidity disequilibrium between the material and the surrounding environment. This moisture transfer may occur at any moment during the life of the cementitious structure, before, during, or after setting, until reaching a hygral equilibrium between the two environments.

The pores that form the porous network in the material contain two phases. A liquid phase which is the liquid water present inside the pore, and a gaseous phase that contains the dry air and the water vapor. Depending on the hygral conditions, the pores of the material can be more of less saturated. The movement of the moisture, whether it is liquid or gaseous, is governed by several mechanisms that are often coupled. The importance of each mechanism

varies depending on the degree of saturation of the material as shown in 2.2 and detailed below.

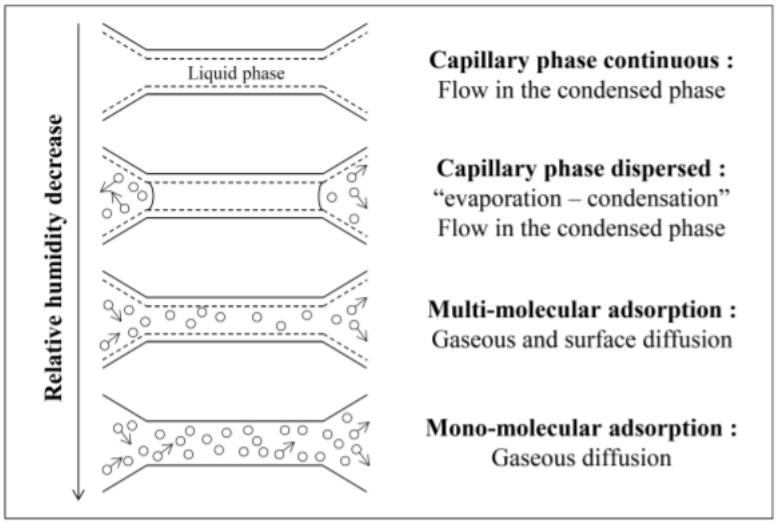

Figure 2.2: Schematics of the water transfers depending on the environmental relative humidity [Baroghel-Bouny, 1994].

Permeation of the liquid phase

In the porous media initially saturated, liquid water fills the capillary network. As soon as the relative humidity drops, a flow is set and liquid water starts to migrate from the interior to the exterior of the material due to a liquid water pressure gradient generated by the evaporation on the surface of the material.

Evaporation and Condensation

When the liquid water and the gaseous water coexists in the pores at a medium relative humidity, the continuity of the liquid phase is disturbed. Water movement continues an exchange between the liquid water and the gaseous phase via evaporation and condensation cycles and is coupled with a flow in the condensed phase. The migration of liquid water, water vapor and dry air coexist.

Gaseous and surface diffusion

At a low relative humidity, water is mainly present as vapor in the gaseous phase. Nevertheless, some adsorbed liquid water can be present in the pores, creating water films at the surface of the pores. A migration of the water molecules can be observed and is called surface diffusion. When relative humidity drops to a very low level and the adsorbed water disappears, the moisture migration is governed mainly by gaseous diffusion of the water vapor due to a concentration gradient, as well as the advection of water vapor during the permeation of dry air and water vapor mixture.

2.2.3 Drying shrinkage mechanisms of cementitious materials

As a cementitious and porous material, the rendering mortar undergoes several types of shrinkage that may occur at different stages during its lifespan. From autogenous shrinkage [Tazawa et al., 1995] at early-age to carbonation shrinkage [Houst, 1997] at a mature age, each type can affect the behavior of the rendering mortar.
Drying shrinkage for instance, or more generally hygral strains, takes place at all stages of life of the cementitious material (Figure 2.3).

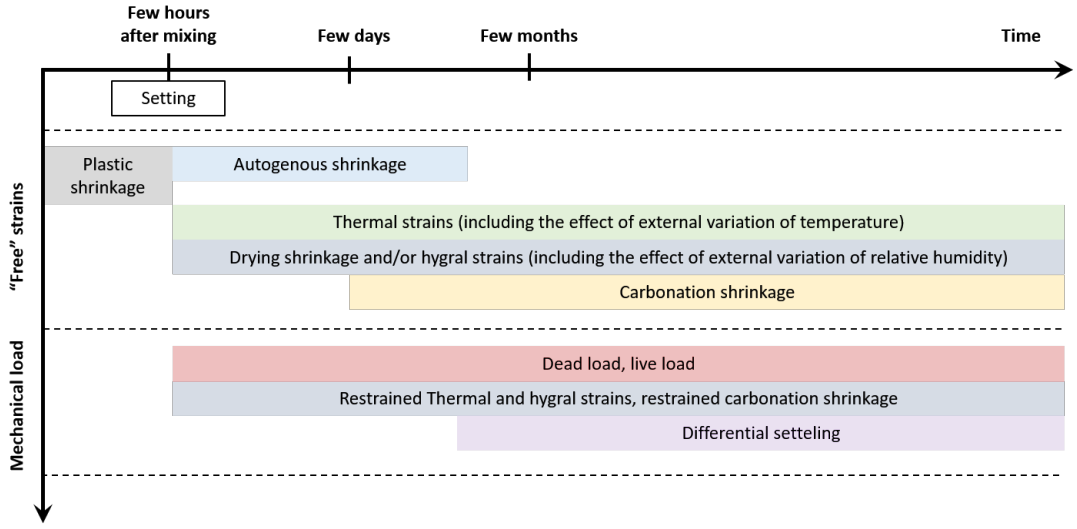

Figure 2.3: Some strain causing loads during the lifespan of a cementitious material.

The drying shrinkage is the deformation caused by the desiccation of the material, or in other terms, by the water loss.
The drying of porous materials has been studied for a long time empirically given the complexity of the structures [Swanson, 1981, Kolodzie, 1980]. The drying of the material can cause structural changes and strains which can be elastic or cause micro-cracks that can lead to minor impacts up to the failure of the structure [Shin and Santamarina, 2011]. The fluid transfers taking place during this phenomenon lead to the displacement of particles or ions, which can concentrate to the point of crystallizing and deforming the porous structure or deplete the structure [Eloukabi et al., 2013]. Thus, it becomes necessary to understand these mechanisms [Lerouge, 2019]. Three main mechanisms have been identified [Baroghel-Bouny, 1994, Baron, 1982], they are highlighted as follows.

2.2.3.1 Capillary tension

The formation of menisci in the capillary pores (see the transition area in 2.4) of the hardened cement paste, when it is subjected to drying, causes tensile stresses in the capillary water. The balance between the tensile stresses and the compressive stresses in the surrounding solid causes elastic [1] shrinkage strains in the solid skeleton. This mechanism happens at high rel-

[1] Creep strains caused by the stress in th solid skeleton can contribute to drying shrinkage.

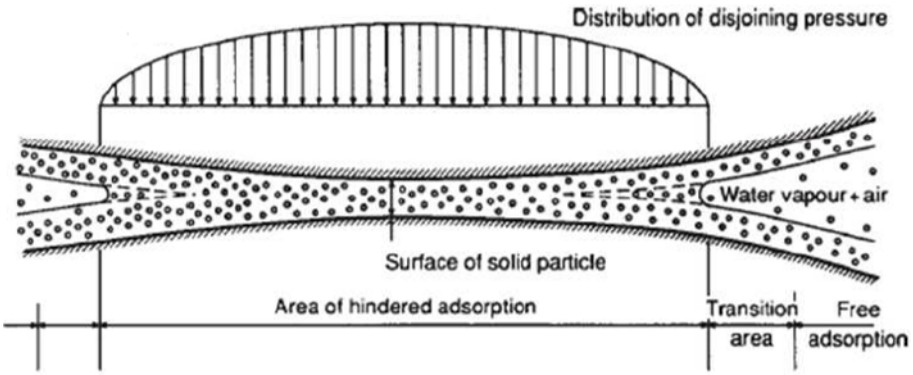

Figure 2.4: Hindered adsorption area and the development of disjoining pressure [Idiart, 2009].

ative humidity ranges (between 50% and 100%) since it fails to explain shrinkage strains at low relative humidity ranges [Acker, 1988, Baroghel-Bouny, 1994].

2.2.3.2 Surface tension

The molecules of solid material are in an equilibrium state because of the attraction and repulsion forces from neighboring molecules. The molecules at the surface of the material are subjected to a perpendicular force due to the lack of symmetry, which causes contraction in the molecules. The tension in the surface is considered as surface tension which causes compressive stresses in the material and leads to elastic [2] strains. The large surface-to-volume ratios of the C-S-H particles make the volume reduction non-negligible and affect the water layers adsorbed on the surface of the material. The generated compressive stresses will be effective due to the presence of the adsorbed water layer causing an increase or swelling in the volume. And then due to drying, this layer could disappear and lead to a volume reduction or shrinkage based on the surface tension. This mechanism is valid at low relative humidity regimes only [Wittmann, 1982].

2.2.3.3 Disjoining pressure or disjunction pressure

The local relative humidity determines the thickness of the adsorbed water layer at a fixed temperature. Any increase in the relative humidity leads to an increase of the adsorbed water layer thickness. When the distance between the different surfaces is very small (on the order of the size of a few water molecules), the water layers could not be fully developed under the surrounding relative humidity and cause the formation of hindered adsorption areas, where disjoining pressures develop (see area of hindered adsorption in 2.4). The developed pressure separates the two surfaces and causes the swelling of the material. Water ordering in small pores determines the equilibrium distance between two pore surfaces in micropores, this distance is associated with large cohesion and is expected to be affected by the relative humidity [Qomi et al., 2021]. When drying occurs, the applied pressures decrease, and the

[2] Creep strains caused by the stress in th solid skeleton can contribute to drying shrinkage.

adjacent particle separation decreases leading to shrinkage strains. This mechanism could explain the continued shrinkage for relative humidity below 40% and the hygral expansion for relative humidity above 50% [Wittmann, 1982].

These mechanisms may be more or less coupled depending on the relative humidity of the material as shown in 2.5.

	Relative humidity					
	0	20	40	60	80	100
Powers (1965)	←	Disjunction pressure				→
				←	Capillary pressure	→
Ishai (1965)	←	Surface energy	→	←	Capillary pressure	→
Feldman & Sereda (1970)		←	Capillary pressure + Surface energy			→
Wittmann (1968)	←	Surface energy	→	←	Disjunction pressure	→

Figure 2.5: Drying shrinkage mechanisms according to [Soroka, 1979]

2.2.3.4 Movement of interlayer water

Another mechanism could take place when the relative humidity drops to about 10%. It is the movement of interlayer water. This interlayer water could migrate out of the C-S-H sheets and reduce the distance between the layers and lead to macroscopic shrinkage strains [Idiart, 2009]. The driving forces for this dehydration involves the change in the hygral conditions in the neighboring meso- and macropores, with which the interlayer pore must be in osmotic equilibrium [Qomi et al., 2021]. This phenomenon is intimately associated with the development of disjoining pressure described above [Qomi et al., 2021]. It must be noted however that the dynamics of water confined in C-S-H is pore-size dependent, being extremely reduced in interlayer pores (0.04% to 0.06% of the self-diffusion of bulk water [Stora et al., 2008, Honorio et al., 2022]. This highlights the slow nature of drying processes when micropores are involved.

2.2.4 Cracking of cementitious materials due to drying shrinkage

The direct consequence of drying is drying shrinkage. The latter is associated to the variation of the water content within the material [Benboudjema et al., 2005]. The desiccation may lead to both surface and core degradation. Core degradation occurs due to the water gradients and the internal restrain induced by rigid inclusions (i.e. sand grains and aggregates) on the cement matrix. The resulting degradation will play a role in the mechanical properties (i.e. Young's modulus, compressive and tensile strength), transfer properties, and failure processes of mortars and concretes. Three mechanisms were identified occurring at three different scales.

2.2.4.1 Macroscopic scale: gradient effect

Drying starts on the surface of the structures where the surface is exposed to a less humid environment. If the structure is relatively thick, drying in the center can occur later than on

the surface. A hydric gradient is therefore obtained between the center of the structure and the drying surface. The hydric gradient will induce a differential shrinkage between the center and the drying surface, creating tensile stresses on the surface that are self-equilibrated by compression in the center of the structure as shown in 2.6. Tensile stresses on the surface can lead to cracking if they exceed the tensile strength of the material [Bazant and Wittmann, 1982, Acker, 1988, Acker, 1991, Neville, 2000]. As the drying progresses, the tensile zone moves toward the core of the material, potentially leading to the cracking of the core [Benboudjema, 2002].

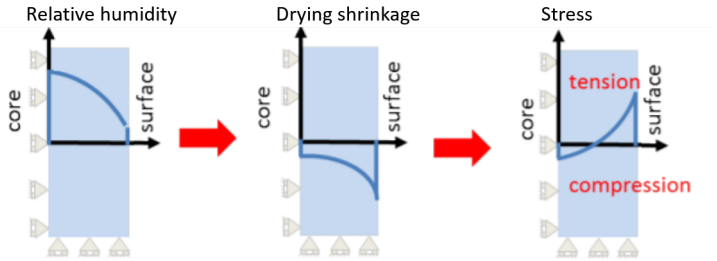

Figure 2.6: Cracking mechanisms induced by the hydric gradient [De Sa, 2007]

2.2.4.2 Mesoscopic scale: aggregate restraint

Cementitious materials are very heterogeneous. They are composed of aggregates, fine sand, the cement paste, and the porosity. As opposed to cementitious materials, aggregates usually display a low porosity and are usually more rigid than the cement paste. Therefore they remain unaltered by drying and drying shrinkage, whereas the cement paste shrinks significantly especially for hight water to cement ratio mixes. A strain incompatibility between the cement paste and the aggregates is thus induced. The shrinkage in the cement paste is restrained by the rigid aggregates inducing tensile stresses at the interface and the transitional zone as shown in 2.7. If the stresses attain the tensile strength of the material, radial and circumferential cracking are initiated around the aggregate as shown in 2.8 [Bisschop et al., 2001].

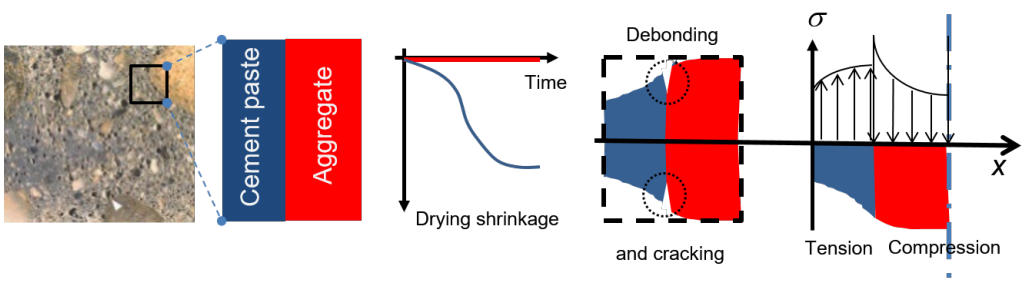

Figure 2.7: Cracking mechanisms induced by the aggregate restraint [De Sa, 2007]

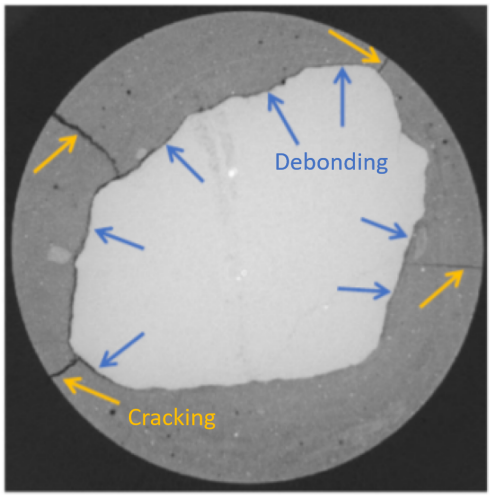

Figure 2.8: 2D projection of the X-Ray radiograph of a cement paste and aggregate sample after 24 hours of drying at 50% RH. [Malbois, 2019]

2.2.4.3 Microscopic scale: local effects

The cracking mechanism described at the mesoscopic scale between cement paste and aggregates can be observed at a nanoscopic scale. Cement paste, which is mainly made of C-S-H, shrinks during drying. On the contrary, both portlandite and ettringite crystals shrink with drying but only for very low relative humidities ($< 10\%$) [Baquerizo et al., 2016, Honorio et al., 2021, Baquerizo et al., 2015]. This leads to the same path of mechanisms and the possible appearance of radial and circumferential cracking around portlandite and ettringite particles [Hearn, 1999, Baroghel-Bouny, 1994, Neville, 2000]. In addition, at microscopic scale, this phenomenon is observed between hydrated cement paste and anhydrous cement particles as shown in 2.9 and between the cement paste and fine aggregates or sand grains.

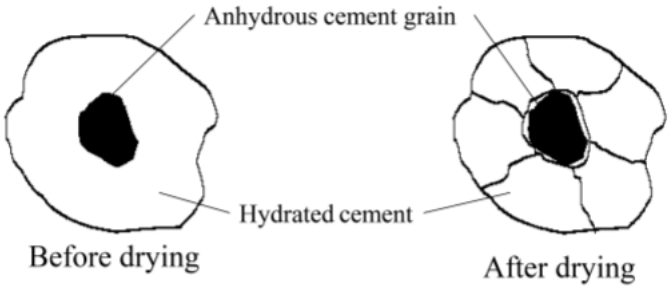

Figure 2.9: Radial and circumferential cracking around an anhydrous cement grain [Hearn, 1999].

In addition, microscopic arrangement of the heterogeneities (rigid inclusion or pores) is also reported to affect the mechanical response. The increase in the disorder of the arrangements of these heterogeneities lead to a degradation of the elastic modulus and strength [Laubie et al., 2017a, Laubie et al., 2017b].

2.2.5 Effect of drying on the mechanical behavior of cementitious materials

Drying have an impact on the mechanical behavior of the cementitious materials affecting the elastic response and mechanical strength. In the previous section 2.2.4, several drying induced cracking mechanisms are detailed and have indeed a negative effect on the mechanical behavior of the material.
In addition, considering the hydration reaction of cementitious materials, the water present in the material is necessary for the progress of this reaction is partially lost. Thus, the advancement of the hydration is limited and the mechanical properties will not fully develop affecting negatively the mechanical behavior of the material. A minimal water content is necessary to fully hydrate the cement [Flatt et al., 2011] and the hydration of the main clinker mineral stops below 80% relative humidity [Hansen, 1986].

Nevertheless, the compressive stress on the solid skeleton induced by the capillary tension discussed in section 2.2.3 can have a positive effect on the mechanical behavior of the material.

The competitions of all factors will result in either an improvement or a deterioration of the mechanical properties of the material. In general, it is considered that a uniformly dry material is more resistant [Baroghel-Bouny, 1994]. The presence of adsorbed water in C-S-H expands the C-S-H sheets and tends to decrease the surface forces between the solid particles [Mills, 1960]. Thus, the properties of the material depend directly on its state of saturation. This state depends on the conservation conditions as well as its duration, but also on the geometry of the structure. Due to the low permeability of cementitious materials and the slow phenomenon of desiccation, it is often difficult to obtain a homogeneous state of the material. This implies that the properties obtained during a mechanical test, with a non-homogeneous drying state, are no longer the result of a material test only, but also of a structural test [Hordijk and Reinhardt, 1990]. These different parameters explain why the results in the literature do not always show a consensus.

Considering the compressive strength, several authors [Butcher, 1958,Mills, 1960,Wittmann, 1968,Burlion et al., 2005] observe an increase of the compressive strength with drying, Whereas other authors [Wittmann, 1985, Torrenti, 1987, Yurtdas, 2003] observe a decrease.
As for tensile strength obtained by direct unilateral tensile tests, [Van Vliet and Van Mier, 2000, Hordijk and Reinhardt, 1990, Brooks and Neville, 1977] report an increase of the tensile strength with desiccation, while [Walker and Bloem, 1957] reports a decrease followed by an increase of the tensile strength.
The same divergence is true for the splitting test, [Butcher, 1958, Mills, 1960, Pihlajavaara, 1974] find an increase in splitting strength with desiccation. This increase seems logical according to [Yurtdas, 2003]. Indeed, in this type of test, the specimen is diametrically solicited. The effect of confinement of the core by the drying surface is thus more important than that of the induced microcracking. However, divergent results are proposed by [Hanson, 1968]. He reports an increase and then a decrease if the splitting strength in the cylindrical specimen, subjected to drying for two years at 50% relative humidity.
Finally, as for flexural tensile strength, divergent results are also obtained. [Pihlajavaara, 1974,

Chan, 2021] report an increase of the flexural strength with drying, while [Mills, 1960, Malbois, 2019] report a decrease.
[Soleilhet, 2018] reports an increase of the resistance for some specimens, tested in compression, direct tension, bending, and splitting, and a decrease for others with drying depending on the surrounding relative humidity and drying duration.

Young's modulus seems to be negatively affected by the drying of the material. Whether in tension [Brooks and Neville, 1977, Toutlemonde, 1994] or in compression [Torrenti, 1987, Burlion et al., 2005, Yurtdas et al., 2006], a decrease in the elasticity modulus is observed with drying. According to [Bucher et al., 2017], a higher degree of saturation is linked to a higher compressibility, thus to a greater Young's modulus.

It seems that the different experimental results do not present a consensus on the impact of desiccation on the mechanical properties. This is mainly due to the difference between the studied geometries (massive or fine), the formulations and types of cementitious materials (mortar or concrete), the hygral conditions imposed and finally the drying duration. It is important to remember that the positive effects such as the capillary pressure are in competition with the negative effects such as microcracking. The final effect of drying on the mechanical behavior of the material depends on whether the negative or the positive effects are predominant depending on the geometry, the formulation, as well as the curing and the testing conditions. Therefore, the competition between the two previous phenomena is specific to each cementitious material, whose influence depends on the type of stress applied to the material [Peng, 2009].

2.2.6 Additives in rendering mortars

2.2.6.1 Polymers in mortars

In this section, the interest is focused on Polymer Modified Mortars (PMM). These materials have been developed to meet certain needs in the field of construction and public works. They are used as tile adhesives, facade coatings, and as repair materials in structures and buildings. The goal was to obtain materials that are easy to work with and have a better performance than the regular mortars. The rendering mortar of this study used as a protection layer for the External Thermal Insulation Composite System belongs to this category of mortars. To better understand the behavior of these materials, it is necessary to understand the properties of the polymers alone as well as their effect on the behavior of the mortars from early-age at the liquid state to the solid aging state.

For the formulation of repair or protection mortars, it is frequent to use synthetic latexes, resulting from emulsion polymerization [Keddie and Routh, 2010]. Synthetic latexes are colloidal dispersions of polymer particles (i.e. polymer particles suspended in an aqueous phase, usually water). The polymer particles size ranges from 100 to 500 nm in most cases. The latexes used for civil engineering applications are commonly synthesized from a wide range of monomers including acrylates, styrenes, vinyl acetates and ethylenes. These latexes are made up of long chains of monomers, containing carbon, hydrogen or oxygen atoms. It is common to

use latexes copolymers (e.g. styrene-acrylate, styrene-butadiene), or even terpolymers [Kardon, 1997,Bureau et al., 2001]. The advantage of these latexes is that they are easy to handle (water being a non-toxic solvent, and the polymer/water mixture is not very viscous), and they can be adjusted to the final properties of the material by using different monomers.

Effect of polymers on the mechanical behavior of mortars The consequences of adding latex are visible on the rheology and mechanical properties of the early-age and hardened mortar mix. The main effect caused by the addition of latex in the cementitious materials is a clear improvement in its workability. This property is interesting because it allows reducing the water content of the mixture when increasing the polymer content to obtain the desired consistency [Barluenga and Hernandez-Olivares, 2004, Saija, 1995]. Thus, at a fixed water to cement ratio, a mortar mix containing polymers is more fluid than an unmodified mortar mix.
As for mechanical properties of PMMs having the same viscosity thus different water/cement ratio, it has been shown that mechanical strength determined in tension, compression and three point bending increases for higher polymer contents [Kardon, 1997,Chandra and Ohama, 1994, Ōhama et al., 1964, Shaker et al., 1997], while elastic modulus decreases [Kardon, 1997, Folic and Radonjanin, 1998, Shaker et al., 1997]. Moreover, the polymer would improve the water retention capability of these materials limiting their drying for the benefit of the cement hydration [Kardon, 1997,Chandra and Ohama, 1994,Folic and Radonjanin, 1998]. It has also been shown that PMMs are more resistant to freeze-thaw cycles and, more generally, would ensure a better protection against environmental stress [Kardon, 1997, Chandra and Ohama, 1994, Ōhama et al., 1964] which is particularly important when the mortar is used as a protection layer (e.g. the studies rending mortar in ETICS). However, since both the water/cement ratio and the polymer content are varied, it is difficult to prove the influence of the polymer on the properties of the modified mortar.
Various authors [Kardon, 1997, Sakai and Sugita, 1995, Sujjavanich and Lundy, 1998, Pascal et al., 2004] showed that for PMMs with identical water/cement ratio, the compressive strength decreases for higher polymer content while the flexural strength increases. The latter is explained by a reinforced Interfacial Transition Zone between the cement matrix and the aggregates [Kardon, 1997,Ohama, 2020], and by the bridging of the cement matrix micro-cracks, due to drying, by the polymer [Kardon, 1997,Bureau et al., 2001,Kardon, 1997]. It has been shown by [Justnes and Øye, 1990] that for Latex rubber modified mortars, the latex forms a continuous network, that would be the origin of the improvement, for polymer contents that exceed $10 wt.\%$.
In the next two paragraphs, the formation of the continuous polymer network is explained by the drying of latex and the microstructure development of PMMs.

Drying of latex and formation of continuous polymer films The drying of latexes is a heterogeneous complex phenomenon [Charmeau et al., 1999, Gerin et al., 1999, Hwa, 1964]. Figure 2.10 shows the different stages of polymer film formation during drying [Goto, 2006]. When polymer particles are dispersed in an aqueous phase (stage a) and when the latter evaporates due to drying, the polymer particles move closer together and their volume fraction increases. The polymer particles form a stack of spheres in contact which can be ordered or disordered (stage b). During this step, the evaporation rate is constant until the

contact created between the particles is irreversible. The evaporation of the remaining water in the interstices is more difficult, thus the evaporation rate decreases. The polymer particles deform into dodecahedrons if specific temperature conditions are met (stage c). The particles begin to coalesce, they merge until forming a continuous and homogeneous film of polymer (stage d).

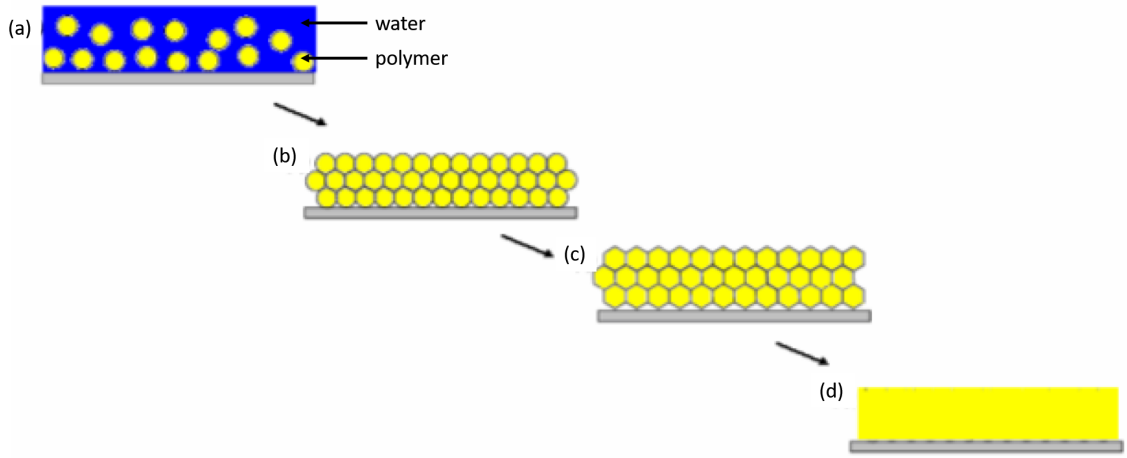

Figure 2.10: Schematic representation of the formation stages of polymer films [Goto, 2006].

Microstructure formation and influence of curing When the cement and the water come into contact, the hydration of the cement is initiated, implying the consumption of this water. This self-drying mechanism initiates, in the case of PMMs, the filmification process of the polymer described in the previous paragraph. These two processes, which take place simultaneously, modify the setting of the mortar-polymer composite. Many authors [Ohama, 1998, Su et al., 1996, Van Gemert et al., 2005] have been interested in the process of formation of the microstructure of the mortar-polymer composites. These studies have led to the establishment of a theoretical model describing the various stages of formation of the microstructure of these materials. A four-step process is represented in figure 2.11.

Step (a): immediately after bringing into contact the cement and the water, the polymer particles are dispersed in the aqueous phase while the cement is about to hydrate.

Step (b): while the cement continues to hydrate and forms cement gel, part of the polymers particles attach to the surface of the cement grains and aggregates. Some particles coalesce and form films that partially or totally coat the cement grains.

Step (c): hydration continues with the formation of hydrates which combine with the polymers. The formation of polymer films goes on under certain curing conditions, and some of the polymers remain isolated in the matrix.

Step (d): as the water depletion progresses, the polymer films are formed within the hydrates. Thus a polymer/cement co-matrix is formed.

Figure 2.12 shows the polymer film formation at the capillary scale of the cementitious matrix.

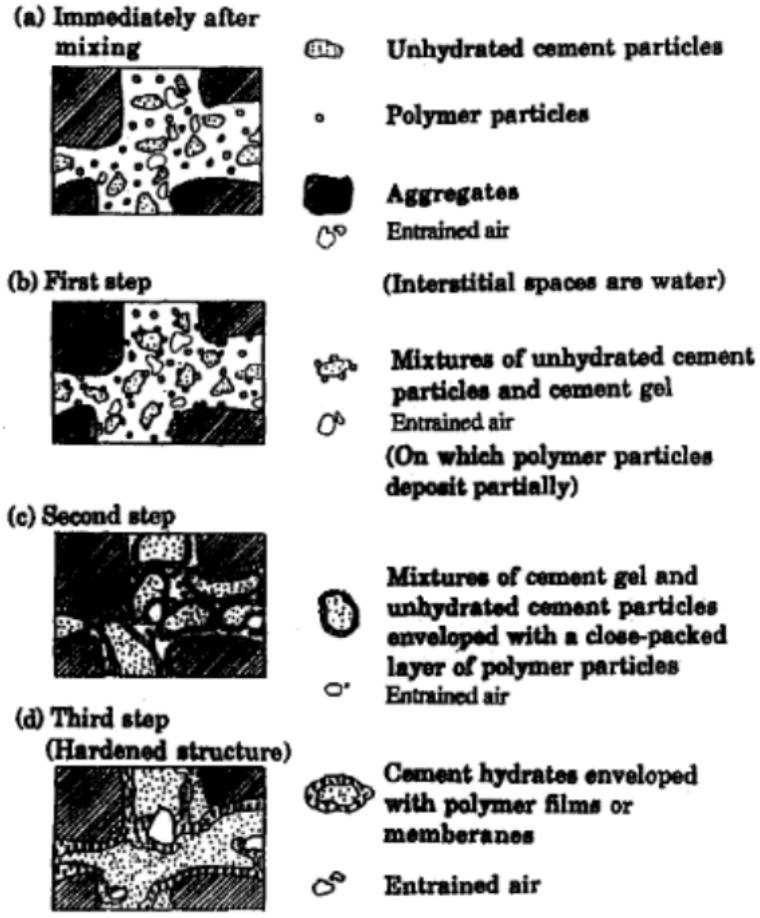

Figure 2.11: Simplified model of formation of polymer cement co-matrix [Ohama, 1998].

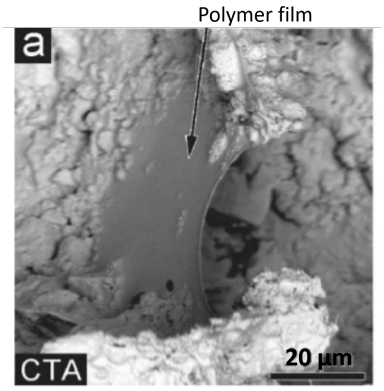

Figure 2.12: Latex film formation at the capillary scale of the cementitious material [Herwegh et al., 2006].

2.2.6.2 Cellulose ethers

Cellulose ethers are polysaccharides commonly used as admixtures in hydraulic mortars for their water retention and homogenization properties. They are dispersed as particles within the

mortar mixture (cement, filler, sand, and other additives). Despite the small quantities generally used (less than $4wt.\%$), they significantly modify the kinetics of development as well as the morphology of the microstructure of the mortar. The types of cellulose ethers commonly used in the construction industry are hydroxyalkyl cellulose ethers, such as hydroxyethyl cellulose (HEC), methyl hydroxypropyl cellulose (MHPC), and methyl hydroxyethyl cellulose (MHEC).

The understanding of the behavior of cellulose ethers in simple media is still under study due to the large number of parameters that can influence the interactions of the molecules between them. In the case of cementitious materials, whose microstructure and physico-chemical features evolve rapidly at a young age, the phenomena related to the incorporation of cellulose ethers are generally characterized macroscopically without clearly identifying the action of the ethers at finer scales.

Cellulose ethers, when added to cementitious materials such as mortars, can have an impact on the behavior of the mortar at both fresh and hardened state. Several authors studied the impact of cellulose ethers on the fresh state properties of cementitious materials. [Khayat, 1998, Knaus and Bauer-Heim, 2003, Paiva et al., 2006, Paiva et al., 2009, Lin and Huang, 2010, Lachemi et al., 2004] for example studied the effect of ethers on the rheology of the material. Others [Weyer et al., 2005, Betioli et al., 2009, Pourchez et al., 2009, Peschard, 2003, Knapen and Van Gemert, 2009] studied the effect of ethers on the hydration. The impact of ethers on the properties of hardened cementitious materials will me detailed in the following paragraph.

Impact of cellulose ethers on the properties of the hardened mortar Many authors [Pourchez et al., 2010, Silva and Monteiro, 2006] studied the influence of cellulose ethers on the microstructure of hardened cementitious materials. According to [Knapen and Van Gemert, 2009], cellulose ethers appear to alter the morphology of portlandite crystals. Scanning Electron Microscopy observations show methyl cellulose films are formed between the portlandite crystals. These films would strengthen the microstructure according to the author.
The same study [Knapen and Van Gemert, 2009] also shows that the incorporation of cellulose ethers promotes, at a mesoscopic level, the cohesion of the hardened cement matrix. For mortar specimens conditioned for 5 days in a room at 93% relative humidity then subjected to several days of drying at 60%, Backscattered electron observations, shown in figure 2.13, reveal that the cementitious matrix is less micro-cracked if the material is modified.

Few studies adress the impact of cellulose ethers on the mechanical properties of hardened cementitious materials. Most of the studies indicate that the addition of ethers descreases the tensile strength, compressive strength, and the Young's modulus [Khayat, 1998, Knapen and Gemert, 2009, Balayssac et al., 2011]. Tests carried out by [Khayat, 1998] on concrete stored in water for 34 days, indicate 5 to 10% decrease of the compressive strength and about 12% of the flexural tensile strength (three-point bending) when the materials are modified with ethers. Similarly, [Knapen and Gemert, 2009] show that for a cellulose ether/cement ratio of 1%, the compressive strength as well as the tensile strength (by splitting test) of mortar specimens stored for 90 days at a relative humidity of 90% decrease. In the case of these two studies, the decrease is explained by the increase of the proportion of entrained air caused by

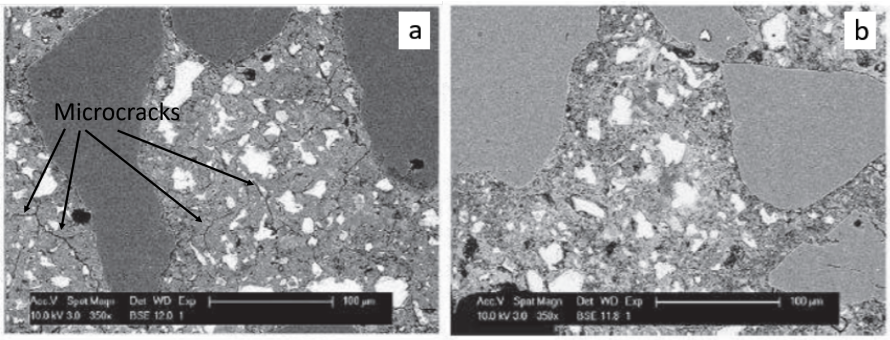

Figure 2.13: Backscattered electron (BSE) image of crack formation in (a) unmodified mortars and (b) HEC modified mortar [Knapen and Van Gemert, 2009].

the presence of the ethers. [Mauroux, 2011] measured a 132% increase of of the entrained air with the increase of the cellulose ether dosage from $1wt.\%$ to $4wt.\%$ to.
However, [Singh et al., 2003] carried out tests on mortars with different proportions of ethers. The authors show that the impact of ethers on the development of the mechanical properties of the cementitious materials is more complex. In addition, for mortars composed of a low proportion of ethers (less than 0.5%), the results indicate a higher compressive strength at 91 days than those obtained for non-adjuvanted mortars. No explanation is provided by the authors.
On the other hand, [Knapen and Gemert, 2009] show that the curing conditions have an important impact on the tensile strength of the adjuvanted mortars. In this study, mortar samples were kept for 91 days at 90% relative humidity in order to ensure a "complete" hydration of the cementitious material. One part of the specimens was kept under the same conditions for another 56 days, while the other part was placed in water for 28 days and placed in "drying" conditions at 60% relative humidity for another 28 days. The mechanical tests carried out on these specimens show an increase on the tensile strength of the mortar when the specimens are placed in "drying" conditions. The authors assume that this increase is related to the presence or not of ether films within the cementitious matrix. Thus, under wet conditions, the polymer films are dissolved and transported into the cementitious matrix, while under dry conditions, the ether films are deposited in the pore space promoting the cohesion of the material. Nevertheless, Scanning Electron Microscopy observations did not allow these authors to observe and validate the presence of ether films in the hardened material under drying conditions.
[Mauroux, 2011] tested the effect of both the dosage of cellulose ethers as well as the curing conditions on the mechanical properties of mortars. As shown in figure 2.14, for the adjuvanted mortar with 0.1% cellulose ethers content, a significant increase of the tensile strength for the specimens placed in drying conditions is noticed compared to the specimens placed in "wet" conditions. No explanation is provided by the author.

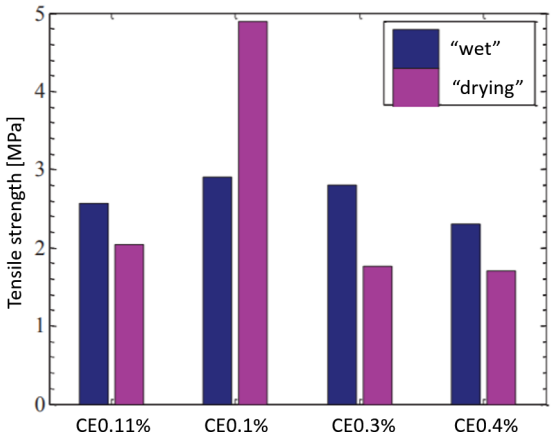

Figure 2.14: Impact of mortar conditioning on its tensile strength at 30 days [Mauroux, 2011].

2.3 Material, mixing protocol, and curing conditions

2.3.1 Material

The rendering mortar used as the protection layer in ETICS is studied. It is an industrial premix and marketed as a basecoat for ETICS. The premix is composed of aerial lime, a hydraulic binder, a siliceous sand, a limestone filler, and additives (i.e. latex polymers and cellulose ethers). Given of the confidential character of this study, neither the reference of the premix nor the ratios of the composition could be detailed. The mortar's microstructure via X-ray tomography (X-ray tomogrpahy technique is detailed in section 3.2.4.1) is shown in figure 2.15.

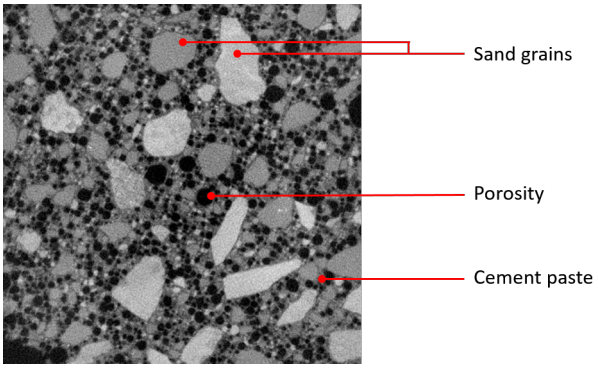

Figure 2.15: X-ray tomography slice of the microstructure of the mortar - Image resolution 10 µm.

The heterogeneous and porous character of the mortar is clearly noticed in figure 2.15. To determine the size range of the sand used in the premix, a Particle Size Distribution (PSD) is carried out by sieving all the components of the premix. As shown in figure 2.16, almost $78wt.\%$ of the premix grains have a particle size smaller than 0.63 mm, and $70wt.\%$ of the particle sizes are smaller than 0.4 mm. According to most of the classification norms (e.g. CSSC, USDA, System ISSS, UNIFIED, AASHO), the majority of the premix particles fall in "Fine Sand" category [Kroetsch and Wang, 2008].

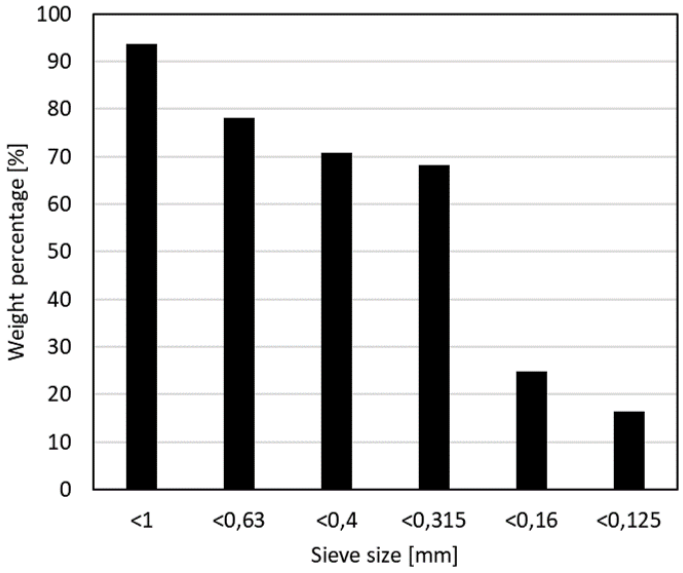

Figure 2.16: PSD of the mortar premix by sieve analysis.

2.3.2 Mixing protocol and casting: Preliminary analysis

The mortar manufacturer recommends 6 L of water for a 25 kg bag of premix. They recommend using an electric hand mixer at 500 rpm for 3 minutes to mix the water and premix, then letting the mixture sit for 5 to 10 minutes before application. Since an electric hand mixer is not available and to limit the non-repeatability associated with human intervention during mixing, an automatic stand mixer is used. Nevertheless, the maximum speed of the automatic stand mixer is lower than the 500 rpm recommended by the manufacturer, thus, some modifications are required to adjust the mixing protocol of the mortar. To study the impact of the mixing protocol on the behavior of the rendering mortar, three mixing protocols are tested.

In total, four batches are cast in order to investigate the effect of, not only the mixing protocol, but also the dimension of the samples as well as their curing conditions. Two dimensions of prismatic samples are considered $4\times4\times16$ cm^3 (called thereafter 4 cm thickness specimens) and $1\times4\times16$ cm^3 (called thereafter 1 cm thickness specimens), as well as two curing conditions, wet and dry. Figures 2.17a and 2.17b show respectively the mean weight loss ($\pm$ standard deviation) of the three $4\times4\times16$ cm^3 and the three $1\times4\times16$ cm^3 tested specimens, stored in drying conditions at 50%$\pm$5% relative humidity and a temperature of 25°C$\pm$2°C, for each of the four cast batches. Note that the specimens were protected from drying during 1 day before demolding, and when drying specimens dry by all 6 facets. Weight loss measurements are chosen. They are easy to perform, reliable and representative to porosity characteristics, drying shrinkage, and mechanical properties. The influence of the mixing protocol on the weight loss curves is clearly noticeable especially on the final weight loss value. The 4 cm thickness specimens cast according to protocols 1, 2, and 3 attain a final value of weight loss of 12%, 10%, and 14% respectively as shown in figure 2.17a. While the specimens of both

batches 3 and 4 cast according to protocol 3, attain almost the same final weight loss value of 14%. This shows the importance of choosing a specific mixing protocol with minimum human intervention in order to insure a repeatable process and to limit the variability of the material's properties caused by a non-repeatability of the mixing protocol, thus influencing the interpretation of certain phenomena related to other modified conditions. The influence of mixing protocols on the properties of cementitious materials is widely studied according to several aspects [Jézéquel and Collin, 2007, da Silva and Lordsleem Jr, 2021, De França et al., 2019].
However, the weight loss of the 1 cm thickness specimens differs from that of the 4 cm thickness specimens. As shown in figure 2.17b, the 1 cm thickness specimens of batch 2 cast following protocol 2 attain the same weight loss value as that of the specimens of batches 3 and 4 cast according to protocol 3, which is not the case for the 4 cm thickness specimens that lost the least percentage of water. This demonstrates that in addition to the influence of the mixing protocol on the early-age drying of the specimens, the dimensions (i.e. the thickness in this case) of the specimens have an impact on the early-age properties of the material. Further early-age properties such as weight loss and shrinkage will be discussed in section 2.4.

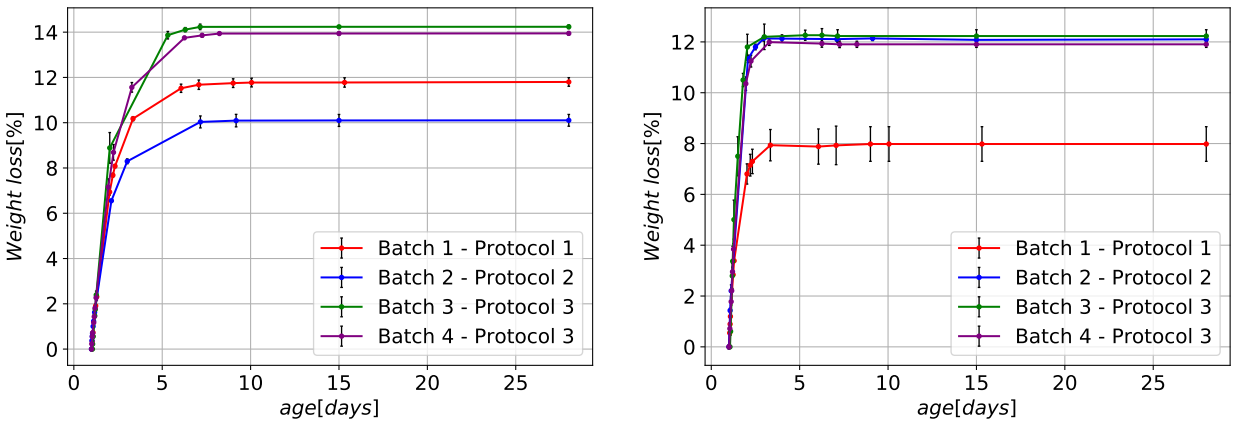

(a) 4×4×16 cm^3 (b) 1×4×16 cm^3

Figure 2.17: Mean weight loss vs. age of the specimens of the 4 cast batches (drying starting 1 day after demolding).

Adopted mixing protocol

As mentioned above, the mixing protocol of the studied rendering mortar recommended by the manufacturer needs to be modified and adopted for research purposes. The mixing protocol needs to ensure a sufficient repeatability by limiting the human intervention in the process. The adopted mixing protocol, detailed in table 2.1 is adapted from the mixing protocol of mortars of the norm "NF EN 196-1".

An Ibermix normalized automatic stand mixer is used. The process starts by adding the premix to the bowl of the mixer and mixing the premix alone at low speed (140 rpm) before

Table 2.1: Adopted mixing protocol.

Step	Speed [rpm]	Duration [s]
Mixing the premix before adding water	140	60
Mixing while progressively adding water	140	60
Mixing at high-speed	300	90
Mixing with a trowel to scrape the sides	NA	60
Mixing at high-speed	300	60
Leave the mixture to "rest"	NA	5 to 10 minutes

adding any water in order to ensure a uniform distribution of all the components. The water is then added gradually while mixing at low speed during 1 minute. Once the water is fully incorporated, the mixer passes automatically to high speed (300 rpm) for 90 seconds. The only needed intervention of the operator is to scrape the sides and the bottom of the bowl to ensure that all the premix initially added is combined to the mix. Finally, the whole is mixed at high speed for another 90 seconds. Before casting into the molds, the fresh mortar sits for 5 to 10 minutes as recommended by the manufacturer. The fresh mortar is then cast into standard 4×4×16 cm^3 molds and custom made 1×4×16 cm^3 molds. No vibration is needed, since the rendering mortar is never vibrated in real life conditions. The molds are immediately protected with several layers of cellophane wrap for 24 hours until demolding.

2.3.3 Specimens and curing conditions

As mentioned earlier, this chapter aims to explore behavior of the rendering mortar at early-age as well as at a mature age. The effect of several parameters (i.e. the mixing protocol, scale effect, curing conditions, and age) is studied. This section details the specimens needed as well as their curing conditions for each of the studied cases.

2.3.3.1 Mixing protocol, curing conditions, and dimensions effects

As mentioned and shown in section 2.3.2, the effect of the mixing protocol, dimensions of the specimens, and the curing conditions on the early-age hygral behavior as well as on the mature age mechanical behavior of the mortar are studied. Four batches are cast according to three different mixing protocols. Each batch includes two thickness specimens, 4 cm and 1 cm thickness specimens that corresponds respectively to the 4×4×16 cm^3 and 1×4×16 cm^3 prismatic geometries. The specimens are demolded and stored in either autogenous or drying curing conditions 24 hours after casting, during which the specimens are protected from drying in their molds with several layers of cellophane films (except D01-2 specimens, see thereafter). The specimens in autogenous conditions are protected with three layers of cellophane film and two layers of adhesive aluminum and stored in a temperature regulated room at 25°C±2°C. The specimens in drying conditions are directly stored after demolding in the same temperature and relative humidity regulated room at 50%±5% relative humidity and a temperature of 25°C±2°C without any protection. The table 2.2 details the specimens of each batch, their dimensions, their curing conditions, their curing time before the mechanical test, their number, and their designation.

Table 2.2: Specimens and curing conditions for studying the effect of mixing protocol, curing conditions, and dimensions on hydrochemical and mechanical properties of the mortar.

Mixing protocol	Batch	Dimensions [cm^3]	Curing conditions	Curing time [days]	Number of specimens	Designation
1	1	4×4×16	Drying	28±2	3	D4-1
			Autogenous		3	A4-1
		1×4×16	Drying	90±10	1	D1-1
2	2	4×4×16	Drying	90±10	3	D4-2
			Autogenous		3	A4-2
		1×4×16	Drying		3	D1-2
			Drying age ZERO		3	D01-2
			Autogenous		3	A1-2
3	3	4×4×16	Drying	90±10	3	D4-3
			Autogenous		3	A4-3
		1×4×16	Drying		3	D1-3
			Autogenous		3	A1-3
	4	4×4×16	Drying	40±5	3	D4-4
			Autogenous		3	A4-4
		1×4×16	Drying		3	D1-4
			Autogenous		3	A1-4

In the table 2.2 above, the designation of the specimens is chosen according to the curing conditions, the thickness of specimens and to the batch number. Thus, the first letter stand for the curing condition of the specimens (i.e. "D" for drying and "A" for autogenous), the second character stands for the thickness of the specimens (i.e. "4" and "1" for 4 cm and 1 cm thickness specimens respectively), the last character stands for the batch number. As an example, the "D4-1" specimens stands for the 4 cm thickness specimens of the first batch stored in drying curing conditions.
The "D01-2" specimens are the only exception. They were not protected from drying with the cellophane film during the first 24 hours after casting. Thus, the drying of these specimens started at age ZERO of the material which is representative of the real conditions of a rendering mortar.

2.3.3.2 Hydration/drying competition study

Drying and hydration may occur simultaneously in cementitious materials. As soon as the water comes into contact with the cement, the hydration is initiated. In addition, depending on the relative humidity of the surrounding environment, the drying of the material is induced. Thus, the free water is transported out of the material, limiting the available water for the hydration reaction in case of a non-abundance quantity of water. In that sense, drying and hydration are coupled. Rendering mortars for instance are subject to drying as soon as they are applied. The complete hydration of the material may thus not be achieved. It can be suggested that the mechanical properties of the material will therefore not be optimal. For low water to cement ratio materials, partial hydration leads to better mechanical properties

since cement grains are more resistant that hydrates. Nevertheless, a sufficient hydration is required to form enough C-S-H to glue the grains. It is not the case for high water to cement ratio materials (e.g. rendering mortars), since cement content is low and porosity is high. Large hydration is required to reduce porosity [Benboudjema et al., 2005]. The effect of the competition between the two phenomena on the mechanical behavior of the material is thus studied. Table 2.3 details the specimens cast for this study, their dimensions, and their curing conditions.

Table 2.3: Specimens and curing conditions for studying the effect of hydration/drying competition on the mechanical properties of the mortar.

Dimensions of the specimens	Curing conditions		Number of specimens	Designation
	7 days	7 days		
4×4×16 cm^3	Water	Drying	3	WD4
	Drying		3	D4
1×4×16 cm^3	Water	Drying	3	WD1
	Drying		3	D1
	Drying		3	D01

Two dimensions of specimens, 1 cm and 4 cm thickness specimens, are cast according to the mixing protocol detailed in table 2.1 to study the scale effect on the mechanical properties of the material on one hand. On the other hand, to study the effect of the drying/hydration competition, the specimens are stored after demolding either in drying conditions for all the 14-day drying period (i.e. specimens D4, D1, and D01) during which the two phenomena are coupled and can both occur simultaneously, or stored in water for 7 days followed by a 7-day drying period (i.e. specimens WD4 and WD1). When specimens are stored in water, there is no drying affecting hydration, thus full hydration may take place for the first 7 days. When in drying conditions, the specimens are stored in a temperature and relative humidity controlled room at 20°C±2°C and 35%±5% respectively. Before demolding, all specimens are protected from drying with several layers of cellophane film for 24 hours except for D01 specimens that were allowed to dry starting age ZERO to further trigger the drying/hydration competition. Note that drying occurs on the six facets of the specimens.

2.3.3.3 Relative humidity effect

Depending on the environmental conditions, the kinetics as well as the degree of drying differ. As discussed in section 2.2.5, drying have an impact on the mechanical behavior of the cementitious materials. To study this impact on the rendering mortar, 1 cm thickness specimens (prismatic 1×4×16 cm^3 specimens) are cast into custom made molds according to the mixing protocol detailed in table 2.1. They are protected from drying in the molds with several layers of cellophane film for 24 hours until demolding. After demolding, the specimens are stored in various curing conditions for 14 days. "W" specimens are stored in water, "A" specimens are stored in autogenous conditions (protected from drying with three layers of cellophane film and two layers of adhesive aluminum), while "D85", "D65", "D50", and "D35" are stored in drying conditions in desiccators containing a corresponding salt solution that regulates the relative humidity inside each desiccator where relative humidity

is continuously measured by sensors. Note that drying occurs on the six facets for the drying specimens. Table 2.4 details the curing conditions of all the cast specimens for this study.

Table 2.4: Specimens and curing conditions for studying the effect of external relative humidity on the mechanical properties of the mortar.

Curing conditions 14 days	Storage	Number of specimens	Designation
Water	Water	3	W
Autogenous	Cellophane film and adhesive aluminum	3	A
85% ± 5%	Potassium chloride saturated solution	3	D85
65% ± 5%	Ammonium nitrate saturated solution	3	D65
50% ± 5%	Magnesium nitrate saturated solution	3	D50
35% ± 5%	Magnesium chloride saturated solution	3	D35

2.3.3.4 Wetting effect

Drying has an impact on the mechanical behavior of cementitious materials in general and on the rendering mortar in particular. Nevertheless, the moisture transfer can occur from the mortar to the surrounding environment in case of drying, but it can also occur in the inverse direction when the relative humidity of the surrounding environment exceeds that of the mortar (e.g. in case of rain). For this reason, the impact of re-humidification after a first phase of drying on the mechanical behavior of the mortar is studied.

Table 2.5: Specimens and curing conditions for studying the effect of re-humidifying after a first phase of drying on the mechanical properties of the mortar.

Curing conditions		Number of specimens	Designation
14 days	14 days		
Water		3	W
Drying		3	D
Drying	Water	3	DW

Table 2.5 details the curing conditions of the cast specimens to be tested for this study. 1 cm thickness specimens (prismatic 1×4×16 cm^3 specimens) are cast in custom made molds according to the mixing protocol detailed in table 2.1. The specimens are protected from drying with several layers of cellophane film during 24 hours until demolding. Once demolded, the specimens are stored either in water for 28 days ("W" specipmens), either in drying conditions in a temperature and relative humidity controlled room at 20°C±2°C and 35%±5% respectively for 28 days ("D" specimens), or in the latter drying conditions for 14 days followed

by re-humidification period of 14 days in water ("DW" specimens). Note that all surfaces of the specimens are exposed to the surrounding environment.

2.3.3.5 Age effect

To further understand the behavior of the rendering mortar, the evolution of its behavior with time studied. 1 cm thickness specimens (prismatic 1×4×16 cm^3 specimens) are cast in custom made molds according to the mixing protocol detailed in table 2.1. The specimens are protected from drying with several layers of cellophane film during 24 hours until demolding. Once demolded, are stored in drying conditions in a temperature and relative humidity controlled room at 20°C±2°C and 35%±5% respectively for different periods of time, 3, 7, 14, 28, and 90 days before being mechanically tested as detailed in table 2.6.

Table 2.6: Specimens and curing conditions for studying the effect of age of the mortar on its mechanical properties.

Drying time before mechanical test [days]	Number of specimens	Designation
3	3	D3
7	3	D7
14	3	D14
28	3	D28
90	3	D90

2.4 Early-age characterization

In this section, the early-age behavior of the mortar is studied. As soon as the water comes into contact with the cement, two main phenomena are initiated, the hydration and the drying responsible for the autogenous and drying shrinkage respectively. To understand the early-age hydrochemical behavior of the studied rendering mortar, weight loss and shrinkage are monitored during the early-age of the material. In addition, isothermal calorimetry is carried out to follow the heat generation due to the hydration reaction and get information about the hydration kinetics.

2.4.1 Weight loss and shrinkage

The weight loss and shrinkage measurements are carried out on the specimens of table 2.2 at early-age. The mass of D4 and D1 specimens of the 4 cast batches is measured to follow the water weight loss during the drying period according to the mixing protocol and to the dimensions of the specimens. An electronic digital scale with a 0.1 g precision is used. The weight variation is calculated in equation 2.1. In this study, the weight variation is considered to be negative when the material loses weight (drying corresponds to a positive weight loss), and positive when the material gains weight in case of humidification.

$$\frac{\Delta m}{m}[\%] = \frac{m_t - m_i}{m_i} \times 100 \tag{2.1}$$

where m_t is the actual mass of the specimen at age t,
and m_i is the initial mass of the specimen at age 1 day directly after demolding.

In addition, the shrinkage strains are measured for D4 and A4 specimens. The shrinkage strains measured for D4 specimens subject to drying are a combination of drying and autogenous shrinkage, whereas those of A4 specimens stored in autogenous curing conditions correspond to autogenous shrinkage only. D4 and A4 specimens are cast in specific molds. The sides of the molds corresponding to the bases of the specimens are pierced along the longitudinal axis to allow the fixing by screws of the studs intended for the measurements according to the norm "NF P15-433". To measure shrinkage strains, a digital retractometer shown in figure 2.18 is used. The retractometer is equipped with two probes fitted with a rectified ball with a diameter between 6 and 7 mm. The procedure for measuring shrinkage strains is in conformity with the norm "NF P15-433".

Figure 2.18: Controlab digital retractometer E0078M

The mean weight loss (± standard deviation) and the mean shrinkage strains (± standard deviation) of D4 specimens of the four cast batches according to three different mixing protocols are shown in figures 2.19a and 2.19b, respectively. It is noticeable in these figures the effect of mixing protocol on both the weight loss and the shrinkage of the material. As shown in figure 2.19a, D4-1 specimens attain a final weight loss value of approximately 12%, D4-2 specimens attain a final weight loss value of approximately 10%, and D4-3 and D4-4 specimens cast according to the same mixing protocol 3 attain the same final weight loss value of approximately 14%. Mixing allows to break the cement flocs. When the mixing speed increases, more cement flocs are broken affecting the hydration kinetics and therefore the properties of the material. In addition, when increasing the mixing speed, the quantity of entrained air increases thus the porosity increases which directly linked to final value of weight loss for a given relative humidity.

Drying shrinkage strains can be directly linked to the weight loss of the material. When the weight loss increases reflecting a more important drying, the drying shrinkage increases.

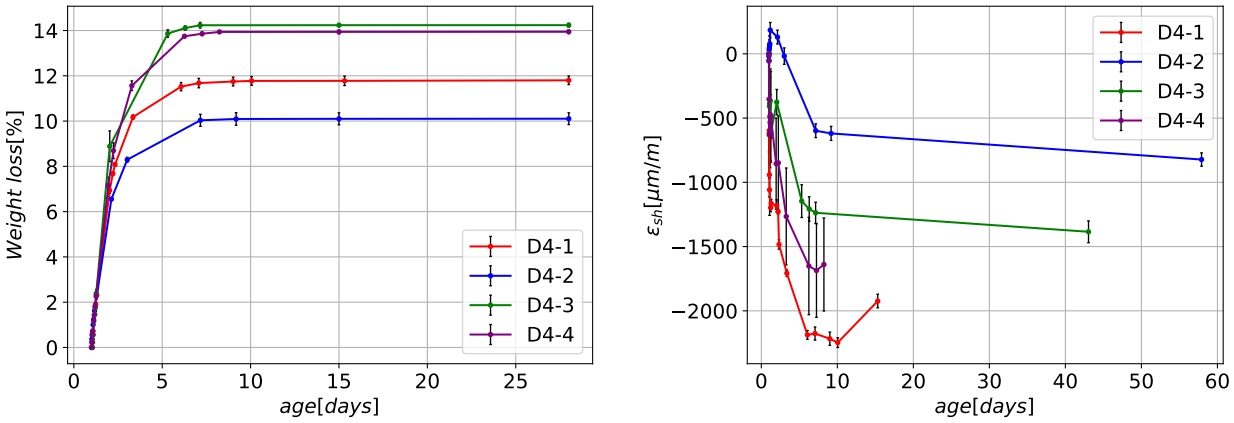

(a) (b)

Figure 2.19: (a) Mean weight loss and (b) mean total measured shrinkage strains vs. age of D4 specimens of the four cast batches.

Nevertheless, this tendency is not obtained for the D4 specimens. As shown in figure 2.19b, D4-1 specimens attain a shrinkage strain of 2000 µm/m exceeding the the shrinkage strains of D4-3 and D4-4 specimens that lost more water. This observation can be explained by the fact that the shrinkage strains measured on D4 specimens includes both autogenous and drying strains, thus drying and hydration are coupled during these measurement making it difficult to properly link the total measured shrinkage strains directly to the weight loss. In addition, autogenous strains of A4 specimens shown in figure 2.20 shows the impact of the mixing protocol on the measured autogenous strains reflecting the impact of the mixing protocol on hydration affecting equally the total shrinkage measured on D4 specimens undergoing both drying and autogenous strains.

It is important to mention the significant uncertainty of the measurements of the strains using the retractometer. It was specifically studied in the PhD thesis of [Chan, 2021] on a large number of specimens. Several factors may increase the uncertainty of these measurements such as dust or grease on the probes or the rectified balls, loosening of the studs, and of course the error induced by the human intervention in the process. According to the norm "NF P15-433", if the measured length variation of one of the three specimens exceeds 0.02 mm that of the specimen having the least length variation, the specimen should be discarded. Thus the mean value should not include this "false" measurement. None of the measurements are discarded in the mean values of the figures 2.19b and 2.20 explaining some large standard deviation values especially in the case of D4-3 measurements.

In addition to studying the mixing protocol on the early-age behavior of the rendering mortar, the scale effect is also studied. To this end, 4 cm and 1 cm thickness are cast. The advantage of working with 4×4×16 cm^3 specimens is the normalized molds and processes that can facilitate the various measurements such as the shrinkage strains measurements. Nevertheless, in real application scenarios, the rendering mortar is applied in a thin layer of 5 mm thickness recommended by the manufacturer. For this reason, it is important to study

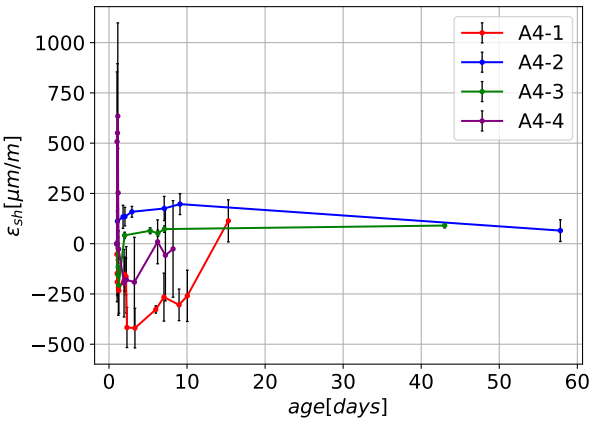

Figure 2.20: Mean measured autogenous shrinkage strains vs. age of A4 specimens of the four cast batches

the mortar's behavior on specimens whose thickness is close to that of the mortar in real application. The 1 cm thickness of the 1×4×16 cm^3 specimens is chosen according to the drying scheme of the specimen. A 5 mm thickness mortar in a real life scenario dries only on the exposed external surface as shown in figure 2.21, whereas the 1 cm thickness specimen dries on both upper and lower surfaces implying a drying length of 5 mm caused by the symmetry of the geometry as well as that of the external hygral loading conditions.

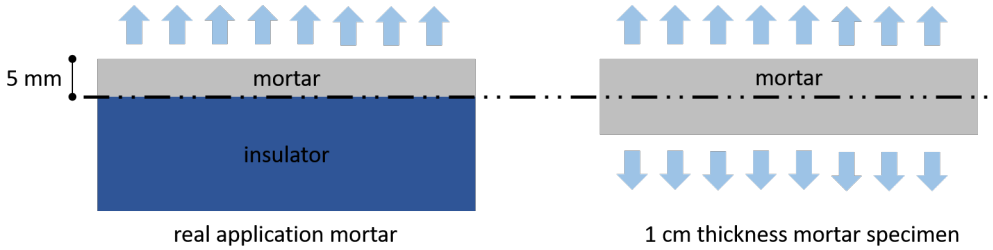

Figure 2.21: Drying of the real application mortar compared to the that of the 1 cm thickness study specimen.

To understand the scale effect on the drying of the mortar, the mean weight loss of D4 and D1 specimens of the four cast batches is plotted in figure 2.23 as a function of $\sqrt{\text{age}}/R_{eq}$ where R_{eq} is the equivalent radius of the geometry of the specimen (also called the notional size of member in code models) defined in equation 2.2 (Refer to appendix A). In figure 2.23, the age ZERO of the material corresponds to the beginning of drying which is at 1 day for D4 and D1 specimens and 0 days for D01 specimens.

$$R_{eq} = \frac{2S}{P} \tag{2.2}$$

where S is the area of the section of the prismatic specimen defined as $h \times b$ (h and b are shown in figure 2.22),
and P is the perimeter of the section of the prismatic specimen defined as $2 \times (h + b)$.

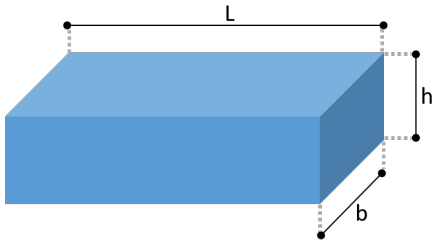

Figure 2.22: Designation of the dimensions of the a prismatic specimen.

It is clearly noticeable in figure 2.23 that the scale effect on the drying of the material represented by its weight loss is not due to pure migration of water in the mortar. The drying of the mortar differs between D4 and D1 specimens in terms of its kinetics shown in the weight loss slope, and in terms of the quantity of the lost water shown in the final weight loss value. D4 specimens for instance of the batches 1, 3, and 4 shown in figures 2.23a,2.23c, and 2.23d, respectively, show a greater weight loss slope as well as a greater final weight loss value compared to D1 specimens. The drying kinetics is generally related to the liquid permeability and vapor diffusivity of the material, while the final quantity of lost water is related to the total porosity of the material for a given relative humidity. This means that D4 specimens of batches 1, 3, and 4 have greater equivalent permeability as well as a greater porosity compared to D1 specimens when both 4 cm and 1 cm specimens are supposed to have the same properties if they are cast from the same batch 1, 3, or 4. The equivalent permeability of the material is related to the porosity of the material, the size of the pores, and to the connectivity of the porous structure. This highlights the difference in the microstructure between the 4 cm and the 1 cm specimens. This is due to the strong coupling between drying and hydration of the material affecting differently the microstructure of the 4 cm and 1 cm thickness specimens.

On the other hand, figure 2.23b show the weight loss curves of the specimen of the batch 2. D4-2 specimens show a greater weight loss slope thus a greater equivalent permeability than D1-2 specimen, but a smaller final weight loss value thus a lower porosity than D1-2 specimens. In addition to the drying/hydration coupling that affects the microstucture of the material, the mixing protocol shows once again an impact on the drying as well as on the hydration of the material leading to a material that have a hydral early-age behavior that differs from that of a mortar cast according to a different mixing protocol.
The geometry and curing conditions of D01-2 specimens are most similar to those of a mortar in a real application where the mortar starts drying as soon as it is applied. However, the weight loss curve of D01-2 specimens shown in figure 2.23b demonstrates that an important part of the drying history of the material is lost since the weight loss monitoring can not be carried when the specimens are still in their molds. Thus, for research purposes, it is preferable to prevent the drying of the material until it is demolded in accordance with the norm "NF EN 196-1" that suggests to store the specimens before demolding in a moist air room where relative humidity should be maintained at not less than 90%.

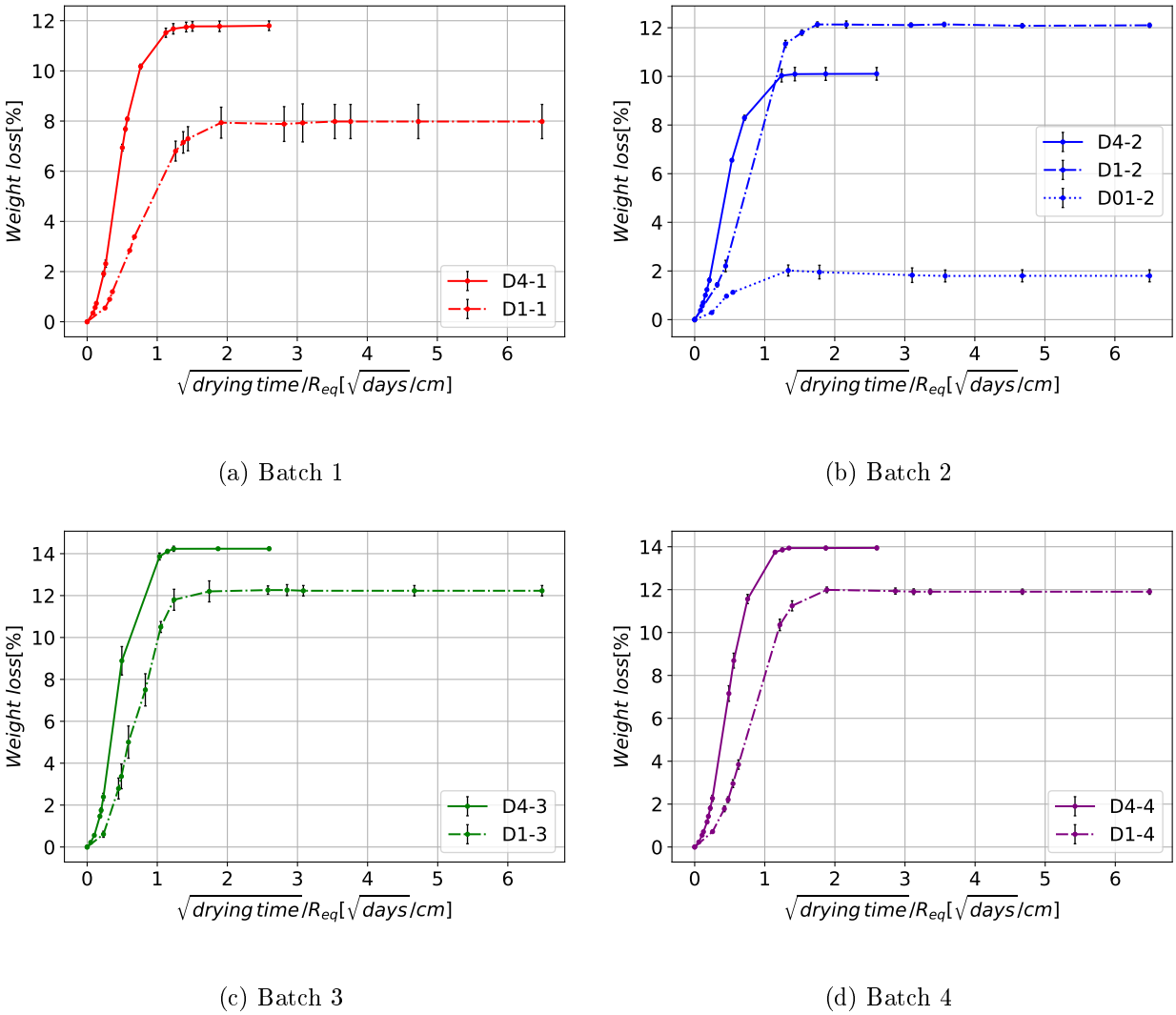

(a) Batch 1

(b) Batch 2

(c) Batch 3

(d) Batch 4

Figure 2.23: Mean weight loss vs. $\sqrt{age}/\mathrm{R}_{eq}$ of the 4 cm and 1 cm thickness specimens stored in drying conditions of the 4 cast batches.

2.4.2 Isothermal calorimetry

As mentioned earlier, isothermal calorimetry is carried out to follow the heat generation due to the exothermal hydration reaction of the rendering mortar. The amount of heat released provides information on the kinetics and the intensity of the reactions. Isothermal calorimetry [Wadsö, 2005] is a technique that consists in maintaining the sample at a constant temperature and measuring its heat flux released, compared to a reference placed in the same cell. The reference contains a non reactive mixture with the same heat capacity as the studied cimetitious material. A thermostat ensures a constant temperature which avoids the heat accumulation problems existing in the adiabatic calorimeters and which could modify the hydration kinetics of the heat-sensitive binder components.

The calorimeter used in this study is an isothermal microcalorimeter "Tam Air" shown in figure 2.24 containing eight cells with an accuracy of $\pm 20\mu W$.

Figure 2.24: Adapted explanatory scheme of the TAM AIR microcalorimeter [Kaci, 2021]

After following the baseline for a duration of at least 12 hours during which the device attain a thermal stabilization, a freshly mixed 5 g mortar sample placed in an ampoule is introduced into the measuring cell. A 5 g non reactive reference is introduced into same cell. In total, 8 mortar samples are introduced into the 8 cells of the calorimeter in addition to 8 references. Two types of references are used, a 5 g mixture of silica sand and water with a water/sand ratio = 0.5 on one hand introduced into 4 cells, and 5 g of water are introduced into the 4 remaining cells as a reference on the other hand.

Figure 2.25 shows the mean cumulative heat flux (± standard deviation) of the 8 samples. The vertical dashed gray line on figure 2.25 corresponds to 1 day age of the samples. 65% of the total heat generated by the hydration reaction at 28 days corresponds to the heat generated during the first 24 hours of the life of the rendering mortar. This result implies that the hydration reaction of the studied rendering mortar is fast and most of the hydration reaction occurs during the first 24 hours of the life of the rendering mortar. In the case of the samples used for the several studies mentioned in section 2.3.3, the mortar is protected from drying during the 24 hours before demolding. This suggests that when the specimens dry after demolding depending of their drying conditions, the competition between the drying of the sepcimens and the hydration reaction is not high.

2.5 Mechanical characterization

2.5.1 Experimental method

The mechanical characterization of the rendering mortar is carried out on all the samples of tables 2.3, 2.4, 2.5, and 2.6 by performing three-point bending tests using the setup detailed in figure 2.26. The upper support applying the load is connected to a 2 kN load cell of an Instron

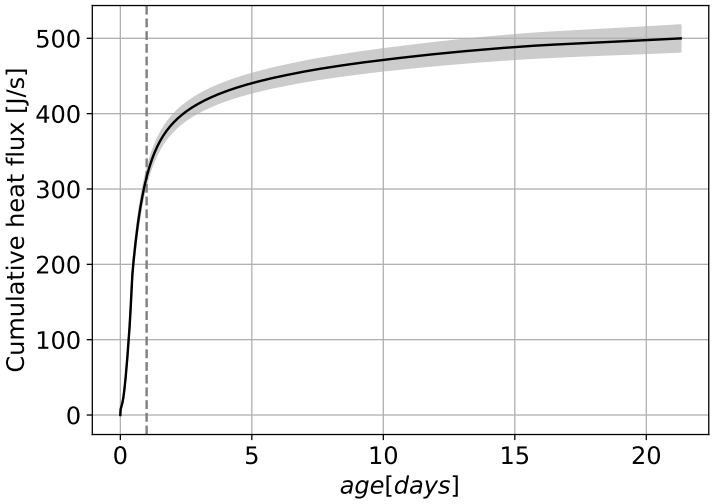

Figure 2.25: Cumulative heat flux measured by isothermal calorimetry

testing machine. The right lower support can rotate around a horizontal axis parallel to the length of the specimen. This rotation allows a homogeneous contact between the surface of the specimen and the support avoiding any concentrated load caused by geometrical defects in the specimen. The distance between the two lower supports is 12 cm. An LVDT sensor is fixed on the lower surface of the specimen to measure the horizontal displacement called "Crack Mouth Opening Displacement" (CMOD). The CMOD measured by the LVDT sensor allows computing the Young's modulus of the material more reliably compared to the machine's displacement that integrates the supports' settlements and the strains in all the elements that transmit the load as well as the the crushing of the mortar and the friction and sliding between elements. Since the focus of the study is the mechanical behavior of the mortar until rupture to determine its mechanical properties (i.e. the tensile strength and Young's modulus) rather than the fracture energy, the mechanical test is controlled by the vertical displacement.

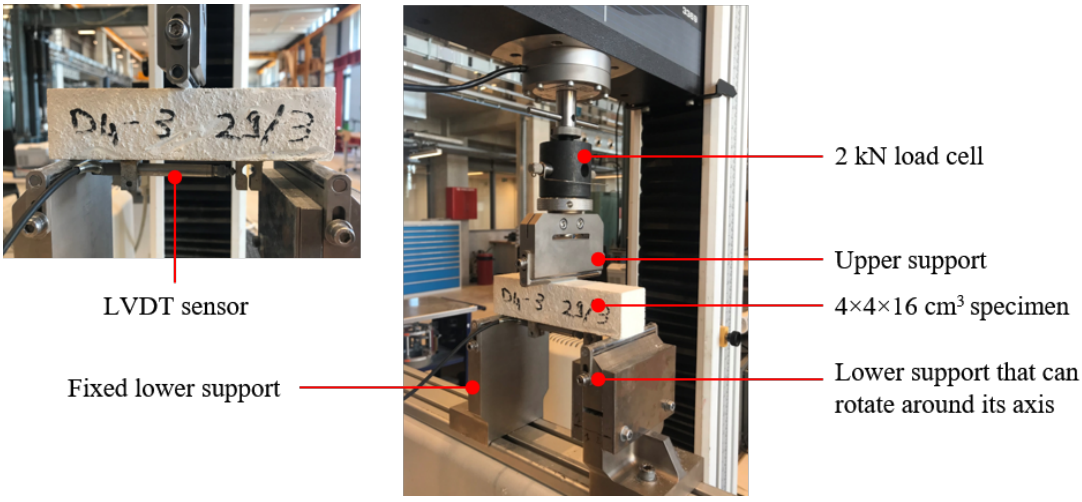

Figure 2.26: Three-point bending test set-up

2.5.2 Results and discussions

2.5.2.1 Hydration/drying competition and scale effect

The rendering mortars are subjected to drying as soon as they are applied. The water needed to hydrate the mortar may therefore be lost by drying. The complete hydration of the material may thus not be achieved. It can be suggested that the mechanical properties of the material will therefore not be optimal. In addition, it has been shown in section 2.4.1 that the drying and the hydration are strongly coupled affecting the early-age behavior of the rendering mortar in terms of weight loss and shrinkage. This campaign investigates the effect of the competition between drying and hydration as well as the scale effect between two different dimensions of specimens the 4 cm and the 1 cm thickness specimens on the mechanical behavior of the rendering mortar. The tested specimens as well as their curing conditions are detailed in section 2.3.3.2.

As shown in figure 2.27a, WD4 specimens that had a curing period in water before drying present a higher failure force than D4 specimens that underwent drying during all the curing period. Similarly, the same tendency goes for the 1 cm thickness specimens as observed in figure 2.27b. WD1 specimens present a greater failure force than that of D1 specimens. In addition, D01 specimens that underwent drying during the first 24 hours before demolding show the lowest failure force. These observations are translated in the flexural tensile strength presented in table 2.7 as the earlier the starting age of drying the smaller the tensile strength. The same tendency applies for the Young's modulus of the mortar presented in table 2.7. These results can be explained by the presence of a competition between drying and hydration. During drying, the specimens lose water that can be necessary for the progression of hydration. The optimum mechanical properties can thus not be attained. The earlier the starting age of drying, the stronger the hydration/drying competition leading to weaker mechanical properties.

Table 2.7: Flexural tensile strength f_t and Young's modulus E (mean value $\pm$ standard deviation) of WD4, D4, WD1, D1, and D01 specimens.

Specimens	f_t [MPa]	E [GPa]
WD4	2.64 $\pm$ 0.22	4.68 $\pm$ 0.56
D4	2.35 $\pm$ 0.02	4.12 $\pm$ 0.29
WD1	2.72 $\pm$ 0.22	4.19 $\pm$ 0.65
D1	1.75 $\pm$ 0.24	3.73 $\pm$ 0.63
D01	1.29 $\pm$ 0.09	2.9 $\pm$ 0.53

Considering the scale effect, although the difference between WD4 and WD1 specimens is not significant, a slight increase in the tensile strength of WD1 specimens compared to WD4 specimens is noticed. This result is expected in mechanical testing and such size-effects can be explained by the Weibull theory [Jayatilaka, 1979]. The larger the dimensions of the specimen, the higher the probability of the presence of defects causing thus a decrease in the tensile strength. On the contrary, the tensile strength of D4 specimens is greater than that of

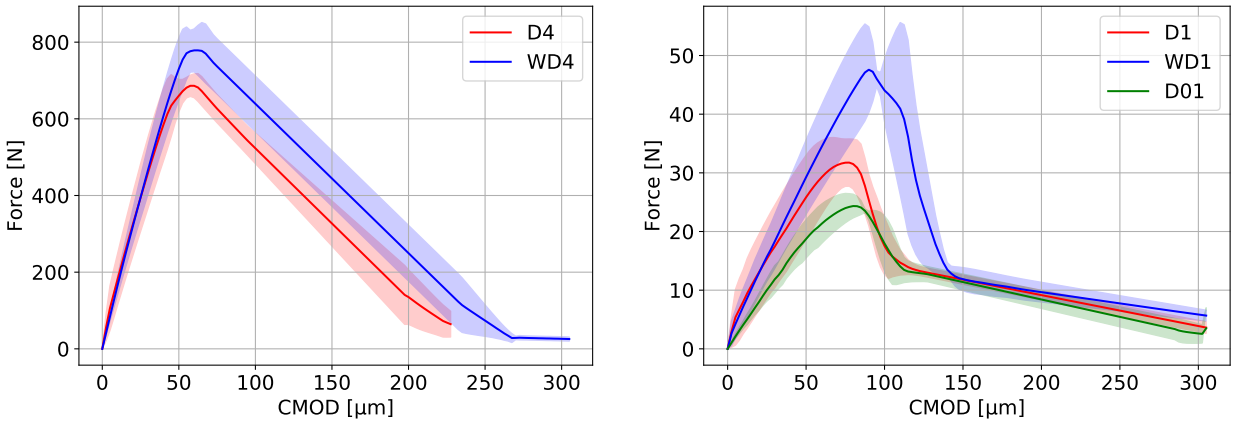

(a) (b)

Figure 2.27: Force vs. CMOD of the (a) 4×4×16 cm^3 specimens and (b) 1×4×16 cm^3 specimens

D1 specimens. The D1 specimens dries faster than D4 specimens. Therefore, the hydration is expected to be lower in D1 specimens leading to higher strength in D4 specimens compared to D1 specimens. This result shows the complexity of the material and of the coupling of hydration and drying.

2.5.2.2 Effect of drying on the mechanical behavior of the rendering mortar

In this section, the effect of drying on the mechanical properties of the rendering mortar is studied. Dry conditions at relative humidities ranging from 30% up to 85%, as well as wet curing conditions (in water and autogenous) are considered to determine the influence of the hygral state of the mortar on its mechanical properties. The tested specimens as well as their curing conditions are detailed in table 2.4.

The evolution of the weight of the specimens in function of their age is shown in figure 2.28. The samples in water show a slight weight gain with time, the samples in autogenous conditions show a constant weight, while the drying samples show a weight loss that is more or less important depending on the ambient relative humidity. However, figure 2.28 shows that the samples stored at a relative humidity of 50% (D50) have lost less water than the samples stored at a relative humidity of 65% (D65). This due to the real ambient relative humidity in the desiccator. Since the water present in the sample migrates towards the environment of the desiccator and because of the small volume of the desiccator, the real relative humidity in the desiccator increases. For that reason, we will present the mechanical properties obtained in the function of the weight variation instead of the theoretical relative humidity of the desiccators. On the other hand, "W" specimens stored in water show a weight gain with time. When stored in water, "W" specimens do not undergo auto-desiccation during which the present water in material is consumed by the hydration reaction. This consumed water is replaced by migrating water from the storing solution explaining the weight increase of "W"

specimens. In addition, entrapped air bubbles created during the mixing and the casting of the mortar may be filled with water if they are connected to the open porosity.

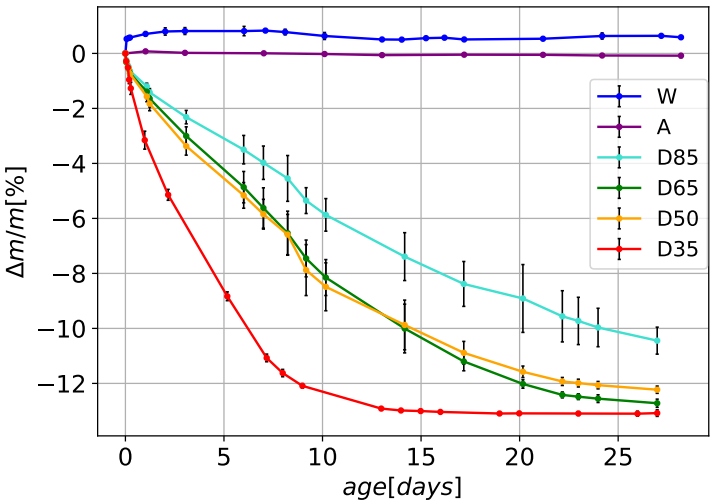

Figure 2.28: Mean weight variation vs. age of the specimens stored in different curing conditions

A clear correlation between the weight variation and the flexural tensile strength is noticed in figure 2.29a. The more the weight loss the higher the flexural tensile strength meaning the stronger the drying the greater the resistance of the material. Moreover, the specimens stored in wet curing conditions, autogenous corresponding to 0% weight variation and in water corresponding to a positive weight variation, present a flexural tensile strength that is significantly lower than that of the specimens stored in drying curing conditions corresponding to the negative weight variation. Thus, drying have a positive impact on the mechanical resistance of the studied industrial rendering mortar. In addition, the difference in the flexural tensile strength between the specimens in the autogenous conditions and in water is significant although both categories of specimens "W" and "A" specimens are stored in wet curing conditions. This can be explained by the excess water present in the specimens stored in water whereas the specimens stored in autogenous conditions undergo the "auto-desiccation" leading to the decrease of the free water in the material.

To further understand the effect of drying on the rendering mortar, the microstructure of the mortar is investigated. X-ray tomography scan are carried out on 1 cm^3 mortar samples extracted from specimens stored in wet ad drying conditions. X-ray tomography is a non-destructive imaging technique that provides a 3D image of the scanned object. It is based on the variation of the absorption coefficient along the path of the incident beam. The absorption coefficient is related to the density and the atomic number of the different materials crossed by the incident beam. Each of the present phases will return a specific gray level that will allow to distinguish it, within the resolution of the image, in the reconstructed 3D volume. Figure 2.15 shows a crop of a 3D X-ray image of the mortar. X-ray tomography will be further detailed in section 3.2.4.1.

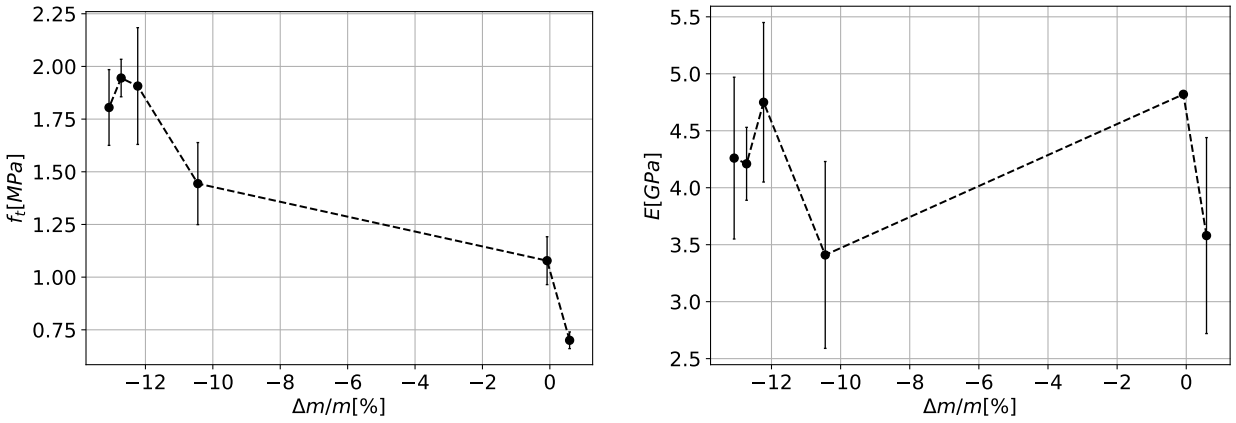

(a) (b)

Figure 2.29: (a) Mean flexural tensile strength f_t and (b) Mean Young's modulus E vs. weight variation

Two post-processing algorithms for tomographic images are then used. The "Multi-Otsu Thresholding" algorithm [Liao et al., 2001] allows to perform a multi-level thresholding. It is used to separate the different phases present in the microstructure of the rendering mortar, including the porosity. Once separated, the porosity is then analyzed by the "3D Object Counter" algorithm [Bolte and Cordelières, 2006] which has the function of calculating several characteristics of each 3D object selected by thresholding, including volume and surface area. This provides the Particle Size Distribution (PSD) of the porosity of each scanned sample. PSD of the porosity of "A" specimens stored in autogenous curing conditions as well as "D50" specimens stored in drying curing conditions is shown in figure 2.30, where it is noticeable a decrease in pore size especially for the porosity of 100 µm diameter and above for "D50" specimens compared to "A" specimens. Therefore, drying affects the microstructure of the rendering mortar by decreasing the size of the larger porosity. This observation can be explained by the drying shrinkage of the material affecting both the solid skeleton and the pores. In addition, in polymer modified mortars such as the studied industrial mortars, drying leads to the formation of a continuous polymer film that can fill the porous network as discussed in section 2.2.6.1.

The increase of the flexural tensile strength shown in 2.29a is not expected in cementitious materials. As discussed in section 2.2.5, the effect of drying on the mechanical behavior of cementitious materials diverge between authors. Nevertheless, in most cases, drying leads to a decrease in tensile strength as well as the Young's modulus of cementitious materials. Several phenomena occur during drying and can lead to a modification of the mechanical behavior of cementitious materials:

- The presence of heterogeneities and particularly the aggregates in cementitious materials can be at the origin of the decrease of the mechanical resistance. The different hygral behavior between the cement paste and the aggregates leads to the incompatibility of

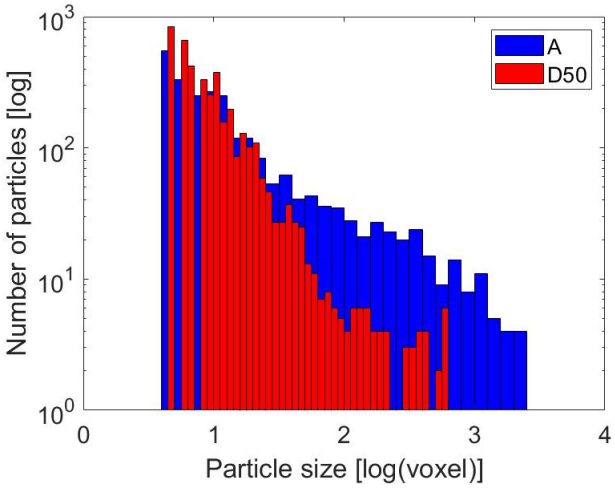

Figure 2.30: PSD of the porosity

hygral strains. During the drying process, the aggregates restrain the drying shrinkage strains of the cement paste. This causes tensile stresses in the cement paste. Cracks in the cement paste or debonding between the cement paste and the aggregates can therefore occur as discussed in sections 2.2.4.2 and 2.2.4.3 at multiple scales.

- The drying of cement materials is a slow phenomenon with an inhomogeneous character. It is more important on the surface, zone exposed to drying than in the core. The desiccation shrinkage is, therefore, more important on the surface than on the core. Tensile stresses are generated on the surface and are balanced by compressive stresses in the core. Surface cracks can appear if the stresses in this area reach the tensile strength of the material as explained in section 2.2.4.1.

- The water present in cementitious materials is necessary for the hydration reaction to proceed and gain strength. However, the water lost through drying can limit the hydration advancement preventing the cementitious materials from reaching their optimum mechanical properties.
  On the other hand, figure 2.29b doesn't show any correlation between the weight variation and the Young's modulus.

In the case of rendering mortars, the increase in the flexural tensile strength of the mortar after drying can be explained by several elements.
The negative effects of drying on the mechanical properties of the standard cementitious materials mentioned above do not seem to be predominant in the case of the studied industrial rendering mortar:

- No microcracks were observed in the tomographic images of the drying specimens within the limit of the image resolution (10 µm). This can be explained by the small size of the sand grains present in the mortar. The PSD of sand and aggregates can have an impact on the microcracking related to aggregate restraint of drying shrinkage as discussed in section 2.2.4.2.

- The water gradient is weak because of the small thickness of the rendering mortar (the manufacturer recommends the application of a layer of 5 mm) as well as the large total porosity in the rendering mortar (ranging from 35 to 40% and calculated using the 3D X-ray images) favoring a relatively rapid drying. In addition, the short linearity of the weight loss curves of figure 2.23 indicates that the core of the specimens starts to dry rapidly proving the weak water gradient along the thickness of the specimens.

- Although the drying/hydration coupling has been proved in section 2.5.2.1, its effect on the mechanical behavior of the mortar seems to be subsidiary compared to the positive impact of drying on the mechanical properties of the rendering mortar. This is certainly due to the additives present in the industrial rendering mortar used for ETICS such as cellulose ethers that have water retaining properties as well as polymer latex. The presence of the latter in the composition of these types of mortar is indeed one of the main causes of the gain in tensile strength observed after drying. They are added to give the rendering mortar more grip and flexibility. During drying, polymers in the form of latex particles form water-resistant films. They are formed at the level of the capillary pores of the cementitious matrix in structures in the form of veils binding the mineral grains. The effects of the latex polymers on the mechanical behavior of cementitious mortar are discussed more in section 2.2.6.1.

In addition, porosity size distribution carried out on drying and non-drying samples shows a decrease in pore size for drying samples as shown in figure 2.30. Porosity is a local defect in the material that is a source of stress concentration in the tensile zone. The smaller the porosity, the lower the stress concentration level for the same loading level, thus delaying the moment of rupture.

2.5.2.3 Effect of rehumidification on the mechanical behavior of the rendering mortar

In the previous section, drying proved to have a positive impact on the mechanical behavior of the rendering mortar especially in terms of mechanical resistance. In this section, the reversibility of the mechanical resistance gain due to drying is investigated. To this end, previously dried samples are rehumidified to be tested mechanically afterwards. D, W and DW specimens of table 2.5are tested mechanically. The mechanical behavior of the specimens stored in the three different curing conditions are compared.

Figure 2.31 shows the mechanical response of D, W, and DW specimens. As discussed in the previous section 2.5.2.2 and clearly noticeable on the force-CMOD curve of D and W specimens in figure 2.31, drying increases significantly the failure force, thus the flexural tensile strength, of the rendering mortar. In addition, the green curve in figure 2.31 of DW specimens shows that, after rehumidification, the failure force of the mortar decreases, thus a part of the strength gained after drying is lost. Nevertheless, the Young's modulus seems to be positively affected by the rehumidifaction. Table 2.8 resumes the mechanical properties of the tested specimens in terms of flexural tensile strength and Young's modulus.

The increase of tensile strength due to drying is mainly due to the formation of ether and polymer films within porous structure of modified mortars such as the studied rendering

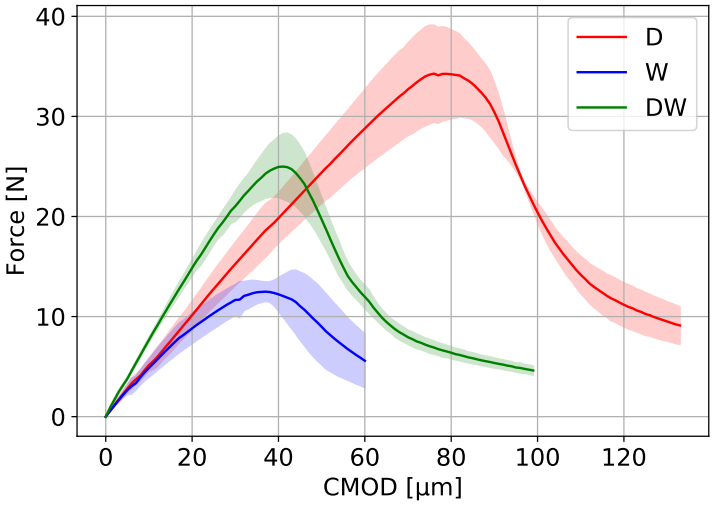

Figure 2.31: Force vs. CMOD

Table 2.8: Flexural tensile strength f_t and Young's modulus E (mean value ± standard deviation) of D, W, and DW specimens.

Specimens	f_t [MPa]	E [GPa]
W	0.7 ± 0.03	3.58 ± 0.86
D	1.82 ± 0.25	3.9 ± 0.54
DW	1.32 ± 0.17	5.81 ± 0.34

mortars. Nevertheless, under wet conditions, the ether films are dissolved and transported into the cementitious matrix, whereas polymer films are water resistant as discussed in section 2.2.6. This explain the loss of part of the mechanical resistance of the rendering mortar that still greater that that of the specimens that never underwent drying.

2.5.2.4 Evolution of the mechanical strength of the rendering mortar with time

As soon as the water comes into contact with the cement, the hydration is initiated. The hydration reaction progresses with time and is directly linked to the evolution of the mechanical properties of cementitious materials. In the section, the rendering mortar is mechanically tested 3, 7, 14, 28, and 90 days after mixing. The aim is to track the evolution of the mechanical properties of the rendering mortar in terms felxural tensile strength and Young's modulus with time.

Figure 2.32a show the evolution of the flexural tensile strength of the mortar with time. Except the tensile strength of the D90 specimens tested at 90 days, the resistance of the mortar seems rather stable between 3 and 28 days after mixing. This is probably due to the highly rapid hydration reaction of this mortar as discussed in section 2.4.2, where the results of isothermal calorimetry of figure 2.25 show that almost 24 hours after mixing, the cumulative heat flux generated by the hydration reaction reaches a plateau. This means that the mechanical properties of the material are mostly reached during the first 24 hours after

mixing. On the other hand, to investigate the decease of resistance at 90 days, observations of the surface one of the D90 specimens is carried out using Keyence digital optical microscope that reveal, as shonw in figure 2.33, some micro-cracking due to severe drying for 90 days at 35% relative humidity.

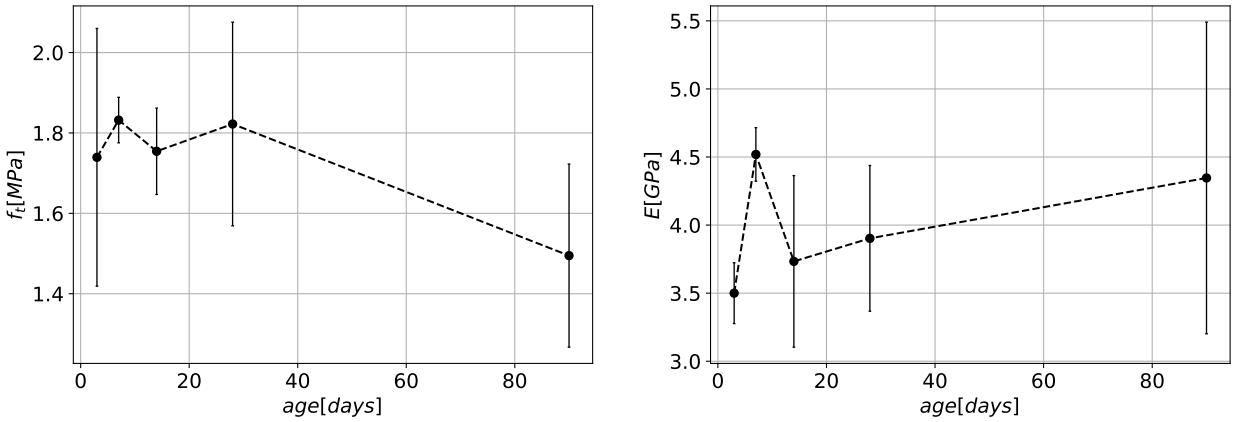

(a) (b)

Figure 2.32: (a) Mean flexural tensile strength f_t and (b) Mean Young's modulus E vs. age of the specimens

Figure 2.32b show the evolution of the Young's modulus of the mortar with time. Despite the second point of the figure which corresponds to D7 specimens, a small increase of the Young's modulus of the mortar with time is noticed. Nevertheless, this increase does not exceed the standard deviation represented by the error bar and thus might not be significant.

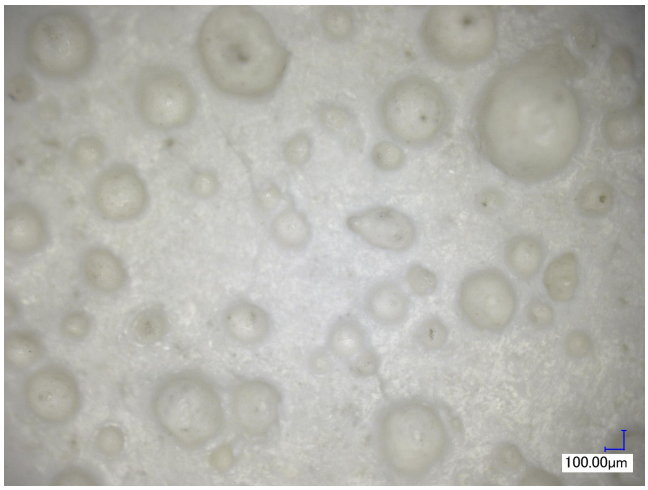

Figure 2.33: Keyence digital optical microscope observation on a D90 specimen

2.6 Conclusion

This chapter deals with the comprehension of the early-age hygro-chemical behavior as well as the mechanical behavior of the rendering mortar used as the protection layer for ETICS. This layer is composite material composed of the rendering mortar and its reinforcement, the glass fiber mesh.

As all cementitious materials, the rendering mortar is in a continuous changing state. The hydration reaction, on one hand, that starts as soon as the premix gets in touch with water, affects the microstructure of the materials and is responsible for its mechanical properties. On the other hand, as a porous materials, the rendering mortar is in continuous exchange of migrating moisture with the surrounding environment depending on the relative humidity of the later. Each of these two phenomena, hydration and drying, as well as the coupling between them will affect the behavior of the rendering mortar.

In this chapter, an experimental campaing focusing on the hygro-mechancial behaviour of the rendering mortar at early-age has been carried out in order to clarify the influence of the mixing protocol, curing conditions and age on the microstructure development and mechanical behavior of the rendering mortar.
The early-age characterization in terms of weight loss and shrinkage has been carried out to study the influence of the mixing protocol, the size of the specimens, and the curing conditions of the early-age behavior of the rendering mortar. It has been shown that a repeatable mixing protocol with minimum human intervention is needed to limit the scatter in the early-age measurements such as weight loss and shrinkage strains. In addition, the scale effect of the drying is highlighted placing in advance the coupling between the hydration of the material and the drying.
Isothermal calorimetry has shown that the hydration reaction of the rendering mortar is fast and most of the hydration reaction occurs during the first 24 hours of the life of the rendering mortar. This suggests that when the specimens start drying at an age of 1 day after demolding depending of their drying conditions, the competition between the drying of the specimens and the hydration reaction is not high. Thus, the mechanical properties of the mortar specimens are not affected by the loss of water that is important for the hydration reaction.
The effect of coupling between the hydration and drying as well as the scale effect on the machanical behavior of the rendering mortar is studied in section 2.5.2.1. It has been shown that the earlier the starting age of drying, the stronger the hydration/drying competition leading to weaker mechanical properties. On the other hand, the scale effect seems to be dependent on the curing conditions of the specimens.
The effect of drying at several relative humidities on the mechanical behavior of the rendering mortar is studied and discussed in section 2.5.2.2. It has been shown that drying have a positive impact on the mechanical resistance of the studied industrial rendering mortar. A clear correlation between the degree of drying and the flexural tensile strength of the material is obtained showing that the stronger the drying the greater the resistance of the material. The gain in tensile strength due to drying is attributed to the presence of latex polymer particles and cellulose ethers that coalesce and form films binding the mineral grains.
In addition, the effect of rehumidification on the mechanical behavior of the rendering mortar

has been studied and discussed in section 2.5.2.3. Part of the mechanical resistance gain of the rendering mortar due to drying is lost after rehumidification. Nevertheless, the tensile strength of the rehumidified samples is still greater than that of the specimens that never underwent drying. The partial loss of the resistance of the mortar is due to the dissolution of the ether films that are not resistant to water unlike the polymer films that are water resistant.
Finally, the evolution of the mechanical properties of the rendering mortar with time is studied. Section 2.5.2.4 shows that between the 3 days age and 90 days age, the mechanical properties seem to be stable. This is probably due to the highly rapid hydration reaction of the studied rendering mortar.

The main conclusion regarding the optimum mechanical behavior, in terms of flexural tensile strength, of this type of rendering mortar, is to store the mortar in wet conditions for an early-age without the intervention of drying that can affect the progress of hydration, then to allow the mortar to dry to let it develop its full potential of resistance. This conclusion is indeed research-based and applies to laboratory-size samples. In a real-life scenario, it will be impossible to store the fresly applied mortar in water or in autogenous conditions. Nevertheless, high relative humidity of the environment is preferred for an early age. Thus, we can choose the application date of the mortar depending on the weather condition. We are conscious of the difficulties and the deadlines imposed on-site during construction projects. Therefore, engineers cannot always wait for the right weather conditions to apply the mortar. Nevertheless, drying conditions allow to attain greater mechanical properties, thus they are preferred.

Although the mechanical behavior of the rendering mortar is important to delay the cracking as much as possible, cracking may eventually occur. The complementary study of the fiberglass mesh, which is the reinforcement of the rendering mortar used for ETICS, is necessary. A full understanding of the cracking mechanisms of the reinforced rendering mortar, the reinforcement mechanisms of the fiberglass mesh as well as the interactions between the reinforcement and the mortar will allow a better dimensioning of the reinforcing meshes. The following chapter highlights these points. The aim is to limit the crack openings as much as possible to better protect the insulator and obtain the most performing and durable ETICS.

Chapter 3

Characterization of the fiber glass reinforced rendering mortar

Reinforced cement-based rendering mortars are used as the protection layer in ETICS. The interactions with the environment changing temperature and relative humidity lead to thermal and hygral strains, which when restrained, may lead to stresses that can attain the tensile strength of the material causing then the mortar cracking. Here, we focus on the cracking development in the reinforced mortar layer using experimental techniques. To understand the crack initiation and propagation in the reinforced mortar layer, and the role of the fiber-glass mesh as reinforcement inside the mortar, new mechanical set-ups are developed. These setup are designed to perform 3-point and 4-point bending tests using in-situ X-ray tomography. The latter allows observing the cracks inside the mortar sample shedding lights on the reinforcement mechanisms of the fiber-glass mesh and its impact on the initiation and the propagation of the cracks. The role of the mortar heterogeneities is also analyzed.

3.1 Introduction

Fiberglass reinforced rendering mortars are used as the protection layer in ETICS. The interaction with the environment changing temperature and relative humidity lead to thermal and hygral strains, which when restrained, may lead to stresses that can attain the tensile strength of the material causing then the mortar cracking. The glass fiber mesh fabric is proposed as a solution for cracking as the base coat reinforcement in ETICS. The previous chapter investigated the effect of relative humidity on the mechanical behavior of the rendering mortars affecting particularly its tensile strength. However, aside from the tensile strength of the mortar, the thermal and hygral loading undergone by the mortar, generates strain restraints induced by the sand grains in the mortar, the thermal insulator, the rigid wall on which the ETICS is installed, and the fiberglass mesh that are either hydrically invariant or have different thermal properties than those of the mortar.

The reinforced rendering mortar is a composite cement-based heterogeneous material containing 4 phases at its meso-scale: the cement paste matrix, the sand grains, the porosity, and the glass fiber mesh. These heterogeneities can concentrate stress and be the source of

initiation and/or localization for cracks. Nevertheless, cracking in the rendering mortar can also be initiated at the structure scale. Geometrical singularities, such as window corners and thermal joints, can be a source of localization of cracks.

The aim of this chapter is to investigate the cracking mechanisms of the reinforced rendering mortar and to understand the role of the mesh with respect to cracking, thus understand the reinforcement mechanisms of the fiberglass mesh. Ideally, the reinforced rendering mortar should be tested under a real environmental load such as the heat and rain cycles applied during the EOTA ETAG 004 tests [EOTA, 2013] discussed in the introduction of the previous chapter 2.1. However, these types of tests are time-consuming and hard to implement and can not be implemented combined with a 3D imaging technique such as the X-ray computed tomography that we aim to use in order to properly visualize the crack within the specimen and not only on the surface of the specimen. In addition, many conditions of restraints need to be implemented (e.g. the restraining wall, geometrical singularities, lateral restrains) to be able to actually create a crack in the mortar. For all these reasons, in-situ X-ray tomography 3-point and 4-point bending mechanical tests are used.

This chapter is presented as follows. First, a review of the literature is carried out focusing on the types, forms and applications of fiberglass, the mechanical behavior of the textile reinforced mortars and concretes and the mechanical characterization techniques used to characterize these materials, and the X-ray tomography technique as well as a brief review of the mechanical testing methods carried-out in-situ X-ray tomography. Then, the experimental characterization of the reinforced rendering mortar is presented in two parts: (i) the 3-point bending tests and (ii) the 4-point bending tests. The effect of several parameters such as the type of mesh, the direction of the mesh within the specimens, and the distance between the mesh and the tensile surface are considered.

3.2 State of the art

Fiber-glass reinforced mortars belong to the family of textile reinforced composites. Composites are characterized by being multiphase materials within which the phase distribution and geometry have been deliberately tailored to optimize one or more properties [Bader, 1997]. Usually, a certain combination of fiber and matrix forms the textile reinforced composites. The range of materials is large. However, a cementitious based industrial mortar matrix and a glass fiber mesh reinforcement will be the subject of this chapter, as the glass fiber mesh reinforced rendering mortar used as a protection layer in ETICS is the center of the study.

The state of the art of this chapter will cover several aspects of the fiberglass, such as the glass types, the fabrication process of the fiberglass meshes, the types of glass fibers and glass fiber textiles present on the market, the eventual coating of the glass fibers, and finally the fiberglass mesh applications. In addition, studies coping with the characterization of macroscopic mechanical behavior of textile reinforced composites are reviewed with focus on the mechanical testing methods that have been deployed.

3.2.1 Glass fiber: materials, types and forms, fabrication process, and applications

Several types of glass and glass fibers exist on the market, each is sold and used for a specific type of applications. In this section, types and forms of glass fibers as well as their applications will be detailed.

3.2.1.1 Types of glass fibers

Depending on the constituent raw materials and their composition, the glass fibers have the following classification [Berthereau and Dallies, 2008].

- **A-glass** Also known as alkali glass or soda-lime glass made with soda lime silicate. It is the most commonly available type of fiberglass. A-glass or soda-lime glass is the predominant glass used for containers and windowpanes.
- **AR-glass** Alkali Resistant glass made with zirconium silicates. Used in Portland cement substrates.
- **C-glass** Chemical glass, made with calcium borosilicates, shows the highest resistance to chemical impact. Used in acid corrosive environments as surface tissue for pipes and tanks that hold water and chemicals.
- **D-glass** Low dielectric constant glass due to the presence of boron trioxide in its composition in addition to borosilicate. Due to this characteristic, D-glass is the ideal type of fiberglass to be used in optical cables and is often used in electrical appliances and cookware.
- **E-glass** Commonly known as electrical glass, it is a lightweight composite material that is used in aerospace, marine, and industrial applications. It is an industry-standard glass that provides a balance between performance and cost. E-glass is known in the industry as a general-purpose fiber for its strength and electrical resistance. It is the most commonly used fiber in the fiber-reinforced polymer composite industry.
- **ECR-glass** An E-glass with higher acid corrosion resistance made with calcium aluminosilicates. Used where strength, electrical conductivity, and acid corrosion resistance are needed.

Other types of glass fibers are be found on the market such as **R-glass**, **S-glass**, **T-glass**, **S2-glass**, **M-glass**, and **Z-glass**. Nevertheless, their production volume is lower, which means that their cost is relatively higher. They are high-performance fiberglass and are used only in specific industries.

3.2.1.2 Fiber and fabric terminology - Forms of fiberglass

The following list defines some of the terminology around the glass fiber and fiberglass textiles [Mobasher, 2011].

- **Filament** A single long and continuous fiber with a predominantly circular shape.

- **Yarn** A bundle of several hundreds up to thousand elementary fibers or filaments.
- **Roving** A process where filaments are spun into larger diameter threads.
- **Fiber fabric** Web-form fabric that has both warp and weft directions.
- **Fiber mats** Nonwoven mats of glass fibers. They are manufactured using chopped or continuous fibers (see **nonwoven** in figure 3.1).
- **Chopped fiber glass** Filaments that are cut between 3 and 26 mm.
- **Glass fiber short strands** Filaments that are cut between 0.2 and 0.3 mm.
- **Woven fabric** A fabric that is manufactured by intertwining two rectangular crossing yarn systems defined as warp and weft called "weaving pattern".
- **Woven** A fabric that is formed by weaving. Note that other fabrics manufactured with other fabrication methods exist such as **braided** fabric, **weft knit** fabric, **warp knit** fabric, and **tufted** fabric (see figure 3.1).
- **Warp** The yarn running along the length of the loom.
- **Weft** The yarn running in the cross direction.

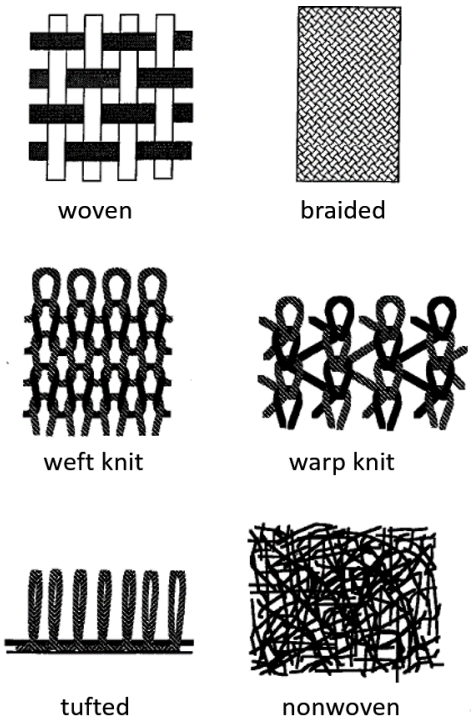

Figure 3.1: Fabrication methods of fabrics [In-house document].

Within the woven fabric category, several types of weaving exist. Figure 3.2 show the **plain** weave, the **twill** weave, the **satin** weave, and the **leno** weave.

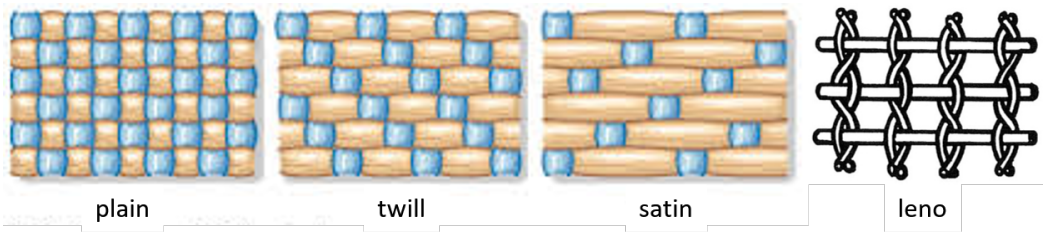

Figure 3.2: Fabric weaving types [In-house document].

Several forms of glass fibers are found on the market, some are shown in figure 3.3. A **roving** is a collection of parallel continuous filaments. It is a thicker version of the **yarn**. Rovings may be woven into heavy, coarse-weave fabric called **woven roving**. The latter is one of many woven **fabric** types. Finally, nonwoven fabric called **mats** such as **surface mats** that are very thin veils of single continuous filaments, **chopped strand mats** that are formed by distributing chopped fiberglass filaments onto a horizontal plane and binding them together with an appropriate chemical binder, and **continuous strand mats** that consist of unchopped continuous filaments of fiberglass deposited and interlocked with a binder onto an horizontal surface.

Figure 3.3: Forms of glass fibers [Sundar, 2020].

3.2.1.3 Coating

When glass fibers were first used as reinforcement in cementitious materials, their main weakness was their low alkali resistance. The rapid deterioration process of glass fibers in cementitious matrices can be attributed to the breakdown of the $Si-O-Si$ bonds, that make up the fiber backbone, by the OH^- ions that are highly concentrated in the alkaline pore solution [Bompadre and Donnini, 2021, Vollpracht et al., 2016]. In the late 1960s, zirconium dioxide ZrO_2 has been added to glass raw material mixture by Majumdar [Bompadre and Donnini, 2021, Paul, 1977]. This addition ensured a higher chemical stability in alkaline solution to the AR-glass compared to the traditionally used E-glass. However, the ZrO_2 layer formed on the glass surface can only slow down the diffusion of the OH^- ions into the glass network, but can not prevent them to react with the silicone dioxide SiO_2. Thus, AR-glass do have a service life longer than that of E-glass fiber, nevertheless, they do not have complete resistance to alkali attack during their service life. In addition, other mechanisms can be responsible for the degradation in glass fiber reinforced matrices such as the microstructural changes that occur over time in the cementitious matrix [Bentur, 2000, Butler et al., 2010]. Thus, the modification of the fibers surface is commonly adopted to preserve the performance of the composite.

A coating can be generally defined as a continuous or discontinuous layer of some compound which is applied on a substrate for functional and/or decorative purposes. Three types of surface modification are distinguished.

- **Sizing** A thin polymeric film that is applied to freshly pulled glass fibers. Sizing formulations usually contains an organofunctional silane, a polymeric film former, and a lubricant.

- **Organic coatings** The application of organic coatings is widely deployed in the industry for the modification of fibers surface and finishing of textiles [Shim, 2013, Joshi and Butola, 2013]. A great variety of organic polymers exist on the market offering an extended range of products by varying the chemical formulation of the coating to meet specific needs. Originally, organic coatings were used to improve the alkali-resistance of glass fibers. However, the impregnation of a multi-filament fabric or textile is also proposed to improve the stress transfer between filaments. Epoxy resins and styrene-butadiene copolymer are used and studied as organic coatings. It has been shown that an epoxy resin coating improved the load bearing capacity of the Fabric Reinforced Cementitious Matrix (FRCM) [Messori et al., 2018, Hegger and Voss, 2008, Büttner et al., 2008, Yin et al., 2015]. The increased mechanical performance observed for coated systems, compared to the dry one, is attributed to the ability of the resin to penetrate into the yarn, increasing the stress transfer between the single filaments (see figure 3.4). Styrene-butadiene coatings are reported to improve the interaction at the fiber-matrix interface [Mäder et al., 2004, Scheffler et al., 2009, Gao et al., 2004].

- **Inorganic coatings** Inorganic coatings are proposed by some studies [Cohen and Peled, 2012, Homoro et al., 2020, Mechtcherine et al., 2020] to replace polymer based coatings judged to compromise the fire resistance of the composite [Donnini et al., 2017, Silva et al., 2014].

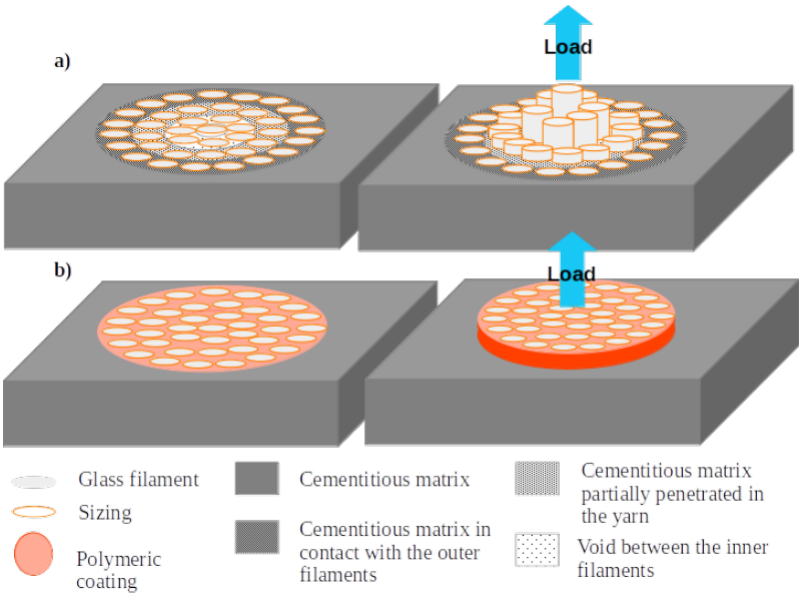

Figure 3.4: Schematic representation of (a) uncoated and (b) coated yarn embedded in a cementitious matrix [Bompadre and Donnini, 2021].

3.2.1.4 Applications of fiberglass mesh

Glass fibers have a wide range of applications. They are used in food and beverage containers, in windowpanes, in optical cables, in electrical appliances, in pipes ans tanks and many other application.
Fiberglass mesh fabrics in particular are commonly used in construction. They can be used as a reinforcement for interior plaster walls, for facade renovations, for flooring creed and profile reinforcement, for marble and mosaic reinforcement, and as reinforcement for the rendering mortar protecting the ETICS, which is the type of fiberglass mesh studied in this project.

3.2.2 Fiberglass reinforced mortars: General mechanical behavior

Fiberglass mesh reinforced mortars belongs to the wide family of Textile Reinforced Mortar (TRM). The stress-strain curve usually obtained for TRMs under uniaxial tensile load is shown in figure 3.5. It is also representative of the tensile behavior of Textile Reinforced Concrete (TRC) which has been schematized by other authors [Colombo et al., 2013, Yao et al., 2015, Rampini et al., 2019, Barhum and Mechtcherine, 2013]

The stress-strain curve shown in figure 3.5 can be divided into three stages: (I) the uncracked stage, (IIa) the multi-cracking stage, and (IIb) the cracks widening stage. During the stage (I), the specimen is in the elastic stage and is still uncracked. The end of the stage (I) is marked by the the appearance of the first crack when the linear behavior ends. With the load increase after the first crack, the specimen enters the stage (IIa) during which new cracks appear successively, due to load transfer between the textile and the matrix, until they are evenly distributed on the surface of the specimen. When the crack spacing is no longer sufficient to transfer the load and create another crack, the specimen enters the stage (IIb)

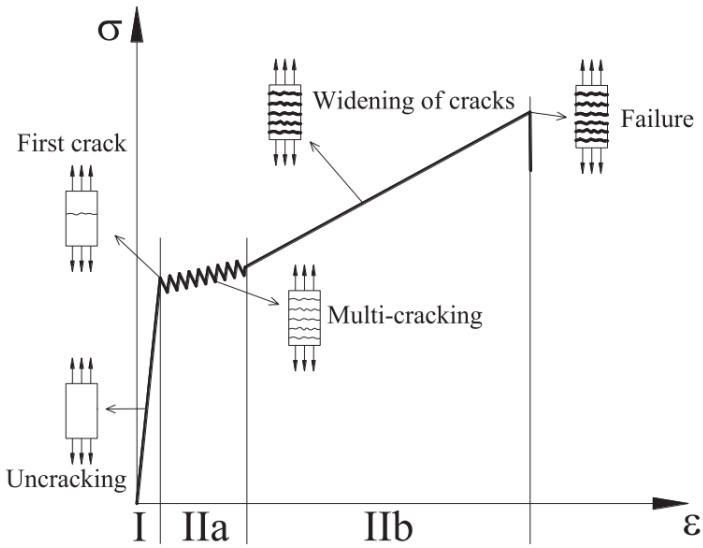

Figure 3.5: Typical stress-strain curves of TRM under uniaxial tensile load [Dong et al., 2020].

during which the cracks gradually widen with the increase of the tensile load. The matrix is out of work and all the load is carried by the textile until its failure.

3.2.3 Mechanical testing review

Few authors investigated the mechanical behavior response of TRCs and/or TRMs. In this section, some of the mechanical testing methods and the main results are discussed to provide an general review. TRCs are often tested under direct uniaxial tension.

[Colombo et al., 2013] studied the tensile behavior of TRC under direct uniaxial tensile tests. Several design parameters were investigated to define their influence on the TRC tensile behavior, such as the reinforcement ratio and position, the fabric geometry, the curing conditions, the testing strain rate, and the size effect. It has been shown that a higher reinforcement ratio of the same fabric results generally in a higher first crack stress. However, for the same reinforcement ratio, the textile position influences both the first crack stress and the cracking pattern. Two layers of the same fabric separated by a 2 mm-thickness layer of concrete ensure a better bond between the textile and the matrix compared to two fabrics in direct contact with each other in the middle of the thickness of the specimen resulting in a higher tense strength for the former situation and a denser cracking pattern. The role of transverse yarn (the yarn perpendicular to the load direction) has been highlighted as a mechanical anchor in the matrix preventing the sliding of the textile. However, it can also act as a defect in the matrix favoring delamination and/or crack propagation. This conclusion came after observing that the lowest first cracking strength is observed in specimen with smallest weft spacing. The influence of curing conditions has been also investigated. The specimen stored in water showed the smallest first cracking strength and least number of cracks compared to the air stored specimen who showed the highest first cracking strength the denser multi-cracking pattern. The authors explain this results by considering that water penetration within the

specimen damages the textile and reduces the bond strength, while desiccation shrinkage undergone by the air dried specimens benefits the bond between the matrix and the textile. The conclusions of the author are based on the stress-strain curves and on the cracking patterns observed on the surface of the specimens.

[Yao et al., 2015] investigated the tension stiffening in TRCs under high speed tensile load. The behavior of non-reinforced mortar specimens is compared to that of a textile reinforced mortars, an Alkali Resistant Glass (ARG) fiber reinforced mortar, and both textile and fiber reinforced mortar. The specimens are tested under direct uniaxial tension. A high speed camera is installed to take images of the specimens during the tests to be analyzed by Digital Image Correlation (DIC) technique. The textile reinforced mortar showed a first cracking stress that is significantly greater than that of the plain mortar highlighting, not only the tensile stiffening behavior of the TRM, but also the ability of the textile reinforcement to delay the appearance of the first crack. Mortars reinforced with both textile and ARG did not show a significant increase of their tensile strength compared to TRM. However, the former samples exhibit the smaller crack widths and higher post-cracking stiffness at equivalent stress levels. The strain fields calculated by DIC, allow not only the crack detection but also the identification of three zones shown in figure 3.6: (i) the localization zone which contains the crack, (ii) the shear lag zone where the slip between the matrix and the textile is predominant, and (iii) the uniform zone where no cracks are formed and where the slip is negligible. DIC allows also the calculation of the crack widths and the cracks spacing.

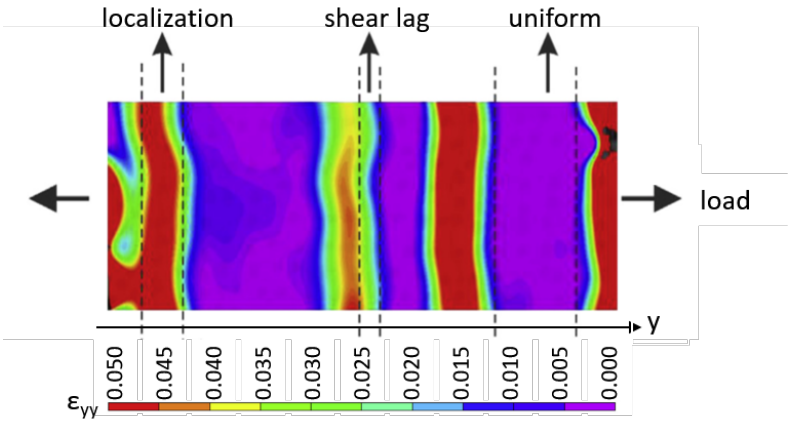

Figure 3.6: Strain field (ε_{yy}) obtained by DIC allowing the identification of three zones: localization, shear lag, and uniform strain. Adapted from [Yao et al., 2015].

[Rampini et al., 2019] characterized the mechanical behavior of TRC composites comparing two types of matrix and 7 fabrics. The fabrics differ by the grid spacing varying between 5 and 38 mm as well as by their coating. Styrene-butadiene rubber (SBR) and epoxy coatings are considered. Direct uniaxial tensile tests are carried out on the TRC specimens. The tests are displacement controlled at 0.02 mm/s and two linear variable differential transformers (LVDT) measured the longitudinal displacement of the specimens known as the crack mouth opening displacement (CMOD) as shown in figure 3.7. The author highlights the increase of

the mechanical capacity of the specimens reinforced with an epoxy coated textile compared to the SBR coated textile. The use of epoxy coating increased the number of cracks. This can be explained by the higher matrix/textile adhesion offered by the epoxy coating allowing the load transfer between the textile and the matrix. A stiffer response is obtained for dense grammage fabrics and a greater damage control is obtained for low to medium grammage fabrics.

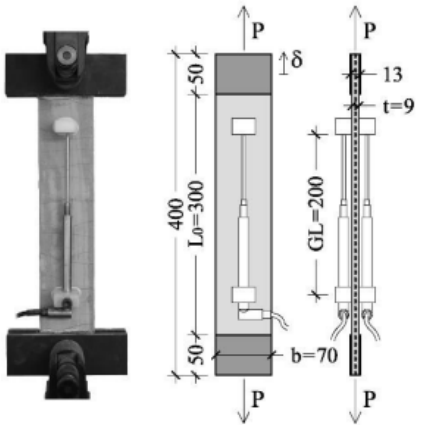

Figure 3.7: Textile reinforced concrete (TRC) specimens: uniaxial tensile test setups and nominal geometries (measures expressed in mm) [Rampini et al., 2019].

Similarly, [Contamine et al., 2011] investigated TRC specimens under direct uniaxial tensile load. Two LVDTs are placed centrally on each side of the specimen to measure the CMOD. In addition, a camera is used to record images to be analysed by DIC. E-glass, AR-glass, Basalt, and Para-aramid fabrics of the same geometry are compared. [Dong et al., 2020], placed an extensometer to measure the longitudinal displacement of a TRM specimen under direct uniaxial tension.

[Genovés et al., 2017] studied an ultrasonic monitoring technique for the detection of cracks in glass-fiber reinforced cement (GRC) tested in 4-point bending. The mechanical testing set-up is shown in figure 3.8. This technique allows the detection of the moment of the crack during the test. However, it does not allow to localize the crack nor to calculate its crack width.

3.2.4 X-ray in-situ mechanical testing

X-ray Computed Tomography (XCT) has become a powerful tool for the acquisition of 3D images and is widely used in material science, from static 3D images used for morphological and quantitative microstructure characterization, to the observation of microstructural changes caused by aggressive environment exposure or thermo-hydro-mechanical loadings. Numerous examples can be cited for cementitious material applications for microstructure characterization due to their high heterogeneity and complex compositions [Brisard et al., 2020]. Several authors [Bentz et al., 1994, Garboczi and Bullard, 2004, He et al., 2010, Roubin et al., 2019] carried out studied on the aggregate and cement paste shapes, others [Bentz et al., 2000, Lu

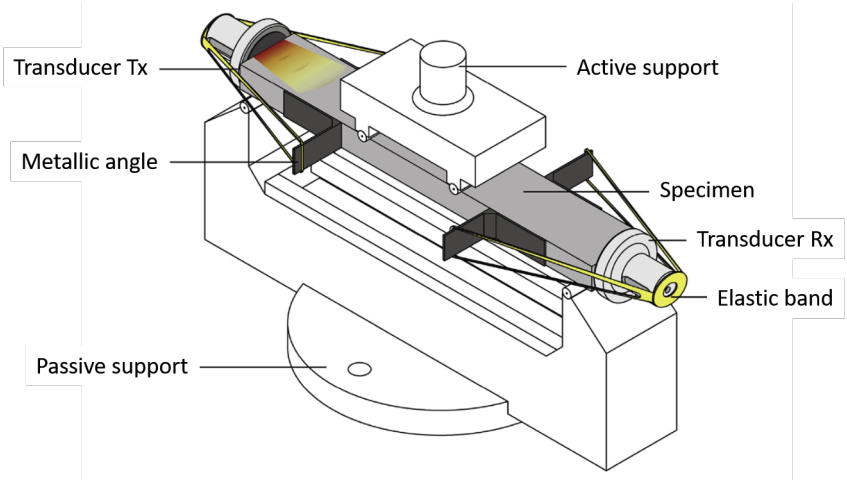

Figure 3.8: Experimental layout used in the ultrasonically monitored bending test. Four metallic angles are attached to the sides of the plate to support the elastic bands that keep constant the pressure between the faces of the transducers and the specimen [Genovés et al., 2017].

et al., 2006,Xu et al., 2021] studied the pore and crack networks, and [Bentz, 1997] among others studied the cement paste morphology. Beyond the static imaging, microstructural changes can be observed. Studies on cementitious materials subject to leaching [Burlion et al., 2006], sulfate attacks [Stock et al., 2002], corrosion [Bernachy-Barbe et al., 2020], and water migration [Powierza et al., 2019] can be cited. An extension to this technique is the X-ray in-situ mechanical testing as in the work of [Riccardi, 2020, Tsitova, 2022, Bouterf, 2014, Ren et al., 2018] among others.

In the previous section, some mechanical testing methods applied on TRCs from the literature are explored. Little to no imaging techniques are used. 2D surface imaging techniques coupled with DIC calculations are useful to measure the displacement fields on the surface of the specimens to locate the cracks (visible and invisible) and to calculate their "apparent" surface width. However, a 3D imaging technique, such as X-ray tomography, can be of a great interest to offer a 3D image of the cracked sample, allowing to correlate the crack localization to textile parameters for example. In this section, the X-ray tomography imaging technique is explained, and some of the X-ray in-situ mechanical testing set-ups of the literature are explored.

3.2.4.1 X-ray tomography

X-ray tomography is a non-destructive technique that allows obtaining a three-dimensional image. It is an imaging technique that generates a data set, called tomogram, which is a three-dimensional representation of the structure. Each three-dimensional point in the tomogram is called a voxel.
In a tomography experiment(see figure 3.9), 3D information is gathered by acquiring a series of 2D images while rotating the sample typically between 0 and 360°. Polychromatic X-rays from a micro-focus X-ray source are used to probe the specimen and an X-ray camera is used to

record the X-ray transmission radiograph. To generate the tomogram, a series of radiographs are collected at different viewing angles by rotating the specimen. This set of radiographs, called projection data, are processed with a reconstruction algorithm to generate the tomogram of the specimen.
X-ray tomography is based on the variations in absorption coefficient along the path of the X-ray beam. The absorption coefficient is linked to the density and the atomic number of the different materials that the beam encounters as it passes through the sample. This is translated by Beer-Lambert law that links the transmit-ted beam intensity to material attenuation coefficient.

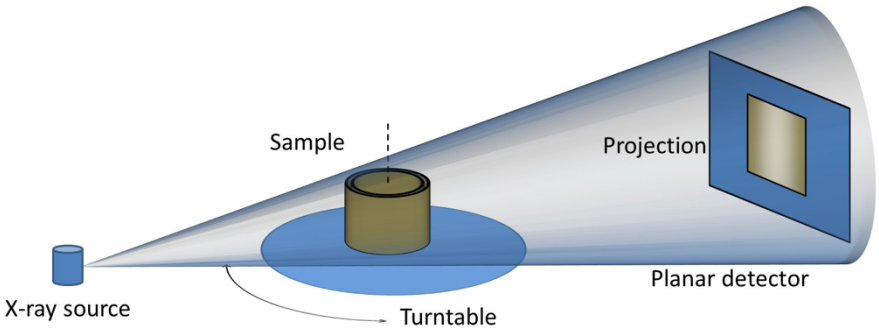

Figure 3.9: Principal components of conventional X-ray tomography system (cone-beam example) [Chen, 2017].

In case of monochromatic X-ray beams, the transmitted beam intensity is calculated as:

$$I = I_0 \cdot exp[\,\Sigma_i(\,-\mu_i x_i)\,] \tag{3.1}$$

where I_0 and I are the X-ray intensities of the incident and transmitted beams, μ_i denotes the linear attenuation coefficient, and x_i the linear extent of the i^{th} material traversed by the beam. In case of polychromatic beams containing a large spectrum of energies, the beam flux is much higher and the exposure time is reduced. The transmitted beam intensity becomes:

$$I = \int I_0(\,E)\,\cdot exp[\,\Sigma_i(\,-\mu_i(\,E)\,x_i)\,]\;dE \tag{3.2}$$

where both I_0 and μ_i are related to the energy E of the incident beam.

3.2.4.2 X-ray in-situ mechanical testing brief review

To the author's knowledge, X-ray in-situ mechanical testing has not been used on textile reinforced concrete or mortars. However, X-ray tomography imaging has been used to visualize the 3D volume of the samples after being mechanically tested [Gopinath et al., 2018, Tlaiji et al., 2020]. This method includes unloading the specimen which leads to re-closure of cracks

modifying the real state of the specimen. In addition, when being moved from the testing machine to the X-ray tomograph, the specimen need to be handled with care to avoid any creation of new cracks. In this section, works from the literature using X-ray in-situ mechanical testing on cementitious materials are discussed.

[Tsitova, 2022] studied during her PhD work, the microcracking in cementitious materials. This author carried out in-situ meso-flexural test on mortar in order to quantify damage via Digital Volume Correlation (DVC) with heterogeneous mechanical regularization. The author proposed a vertical 3-point bending set-up shown in figure 3.10 inspired from the various vertical 3-point and 4-point bending set-ups proposed by [Bouterf, 2014] who carried out X-ray in-situ mechanical testing on gypsum specimens. However, in the proposed vertical bending set-up, neither the actual bending force nor the deflection of the beam is controlled. In addition, depending on the length of the beam, buckling may occur.

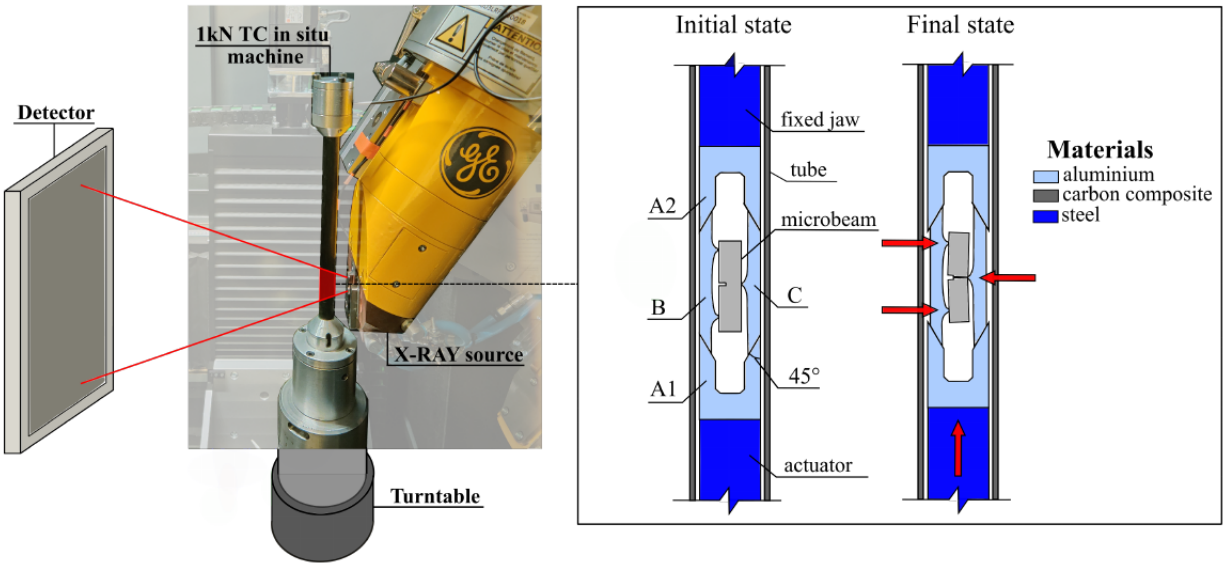

Figure 3.10: Schematic and actual views of the in situ three-point flexural set-up [Tsitova, 2022].

The achievable image resolution being inversely proportional to the largest cross sectional dimension traversed by the X-rays, a vertical configuration is preferable with respect to a horizontal one. Another type of vertical set-up is proposed by [Riccardi, 2020]. The author proposed a non-conventional bending layout shown in figure 3.11 that aims to describe the local mechanical behavior of a Fiber Reinforced Polymer (FRP) strengthened beam-column joint.

In this work, a new X-ray in-situ mechanical test is designed and detailed in the remaining of this chapter.

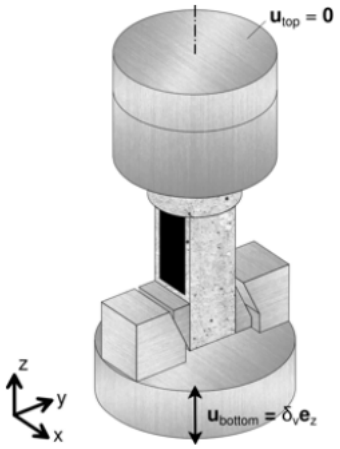

Figure 3.11: 3D sketch of the test configuration [Riccardi, 2020].

3.3 Materials, casting of specimens, and curing conditions

3.3.1 Materials

This study focuses on the understanding of the mechanical behavior of the fiberglass reinforced rendering mortar, as well as the cracking and reinforcement mechanisms. To this end, fiberglass reinforced mortar specimens are mechanically tested. The mortar used, is the industrial premix used as basecoat for ETICS described in section 2.3.1. The glass fiber reinforcement is an industrial glass fiber mesh designed and sold specifically for ETICS applications. The filaments of the glass fiber mesh are made out of E-glass type. The mesh is a leno woven fabric as shown in figure 3.12, and is coated with a styrene-butadiene copolymer which have alkali-resistance properties.

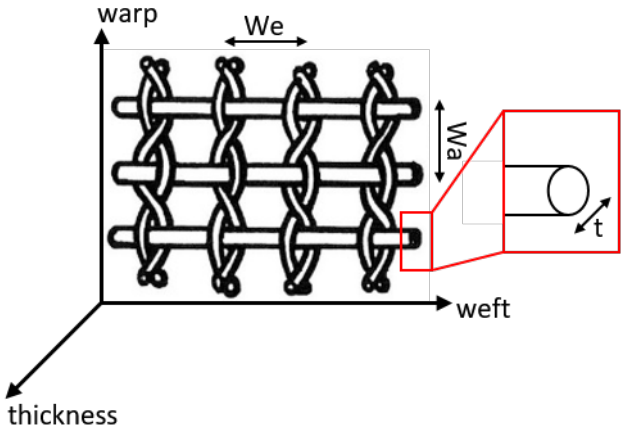

Figure 3.12: Schematic geometry of a leno woven fabric.

Two glass fiber mesh references M1 and M2 are investigated and are shown in figures 3.13a and 3.13b. Their properties are detailed in table 3.1, where the weft spacing (We) is the spacing in the weft direction, the warp spacing (Wa) is the spacing in the warp direction,

and the thickness (t) is the thickness of the mesh in the third direction (see figure 3.12). In addition, unidirectional reinforcement is investigated. To this end, some specimens are reinforced with longitudinal yarns only. The latter, is either weft yarns extracted from M1 fabric, either a roving yarn that has the same density as the M1 yarns and that has been impregnated in coating in the laboratory.

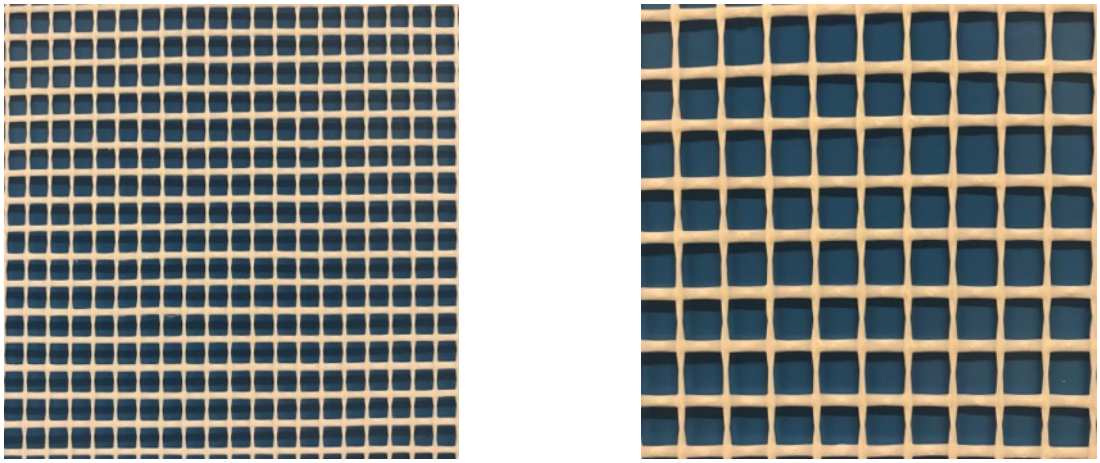

(a) (b)

Figure 3.13: The two investigated glass fiber meshes (a) M1 and (b) M2.

Table 3.1: Properties of meshes M1 and M2.

Mesh	**Warp spacing (Wa) [mm]**	**Weft spacing (We) [mm]**	**Thickness (t) [mm]**	**Weight [g/m^2]**
M1	3.5	3.8	0.52	160
M2	8	8	0.82	219

3.3.2 Casting of specimens

The mortar is mixed according to the mixing protocol detailed in table 2.1. The mortar is then cast into custom made molds to obtain 5 mm thickness prismatic glass fiber mesh reinforced mortar samples of 70 mm long and 12 mm wide. The manufacturer of the fiberglass meshes recommends placing the meshes within the external half of the 5 mm thickness layer of mortar applied on the ETICS. Thus, the fiberglass mesh is positioned at either 1 mm or 2 mm from the lower tensile surface (during the bending test) which corresponds to the unmolded free surface while casting to investigate two positions of the mesh within the thickness of the mortar. A schematic specimen geometry is shown in figure 3.14.

The custom-made molds need to ensure not only the dimensions of the specimens, but also an exact positioning of the fiberglass mesh within the thickness of the specimen. For this reason a 3 layer poly(methyl methacrylate) (PMMA) mold made by laser cutting is manufactured. The first layer is the base layer, the second layer ensures the 3 or 4 mm mortar thickness, and

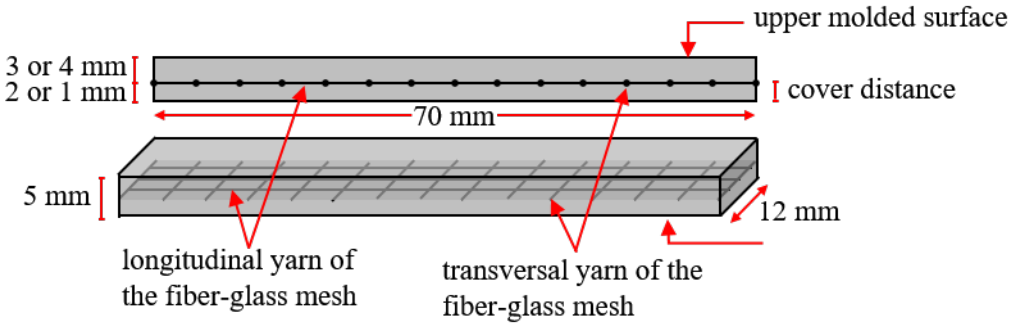

Figure 3.14: Schematic geometry of a fiberglass reinforced morter specimen.

the third layer ensures the 2 or 4 mm mortar thickness, respectively, for a total thickness of 5 mm as shown in figure 3.15.

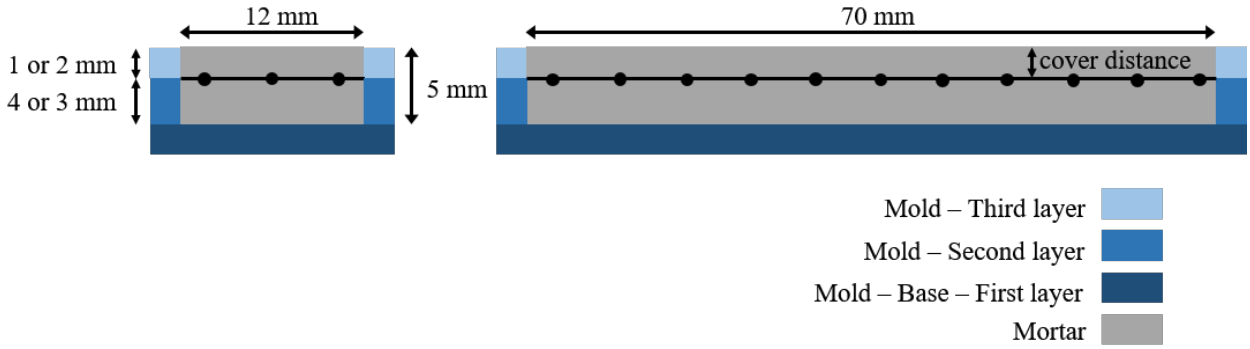

Figure 3.15: Schematic geometry of the custom made mold.

The specimens are tested in either 3-point or 4-point bending tests. Several parameters are investigated. For the specimens tested in 3-point bending, the influence of only the transversal yarn is investigated. The transversal yarn, which is a weft yarn in the case of 3-point bending, is placed either in the middle of the specimen directly under the upper central support, either no transversal yarn is placed in the middle of the length of the specimen meaning that the upper central support is placed between two tranversal yarns. Table 3.2 details the specimens tested in 3-point bending.

Table 3.2: Specimens tested in 3-point bending.

Mesh	**Transversal yarn**	**Cover distance** $[mm]$	**Transversal yarn in the middle of the specimen under the upper central support**	**Number of specimens**	**Denomination**
M1	Weft	2	Yes	1	M1-3P-M
M1	Weft	2	No	1	M1-3P

Several parameters are investigated in the case of the specimens tested in 4-point bending such as the distance between the mesh and the lower tensile surface (called thereafter the cover distance), the fabric properties (M1 and M2 that differs by their warp and weft spacing as well as their density), the longitudinal yarn (whether it is a weft or a warp or neither when the mesh is rotated at 45° (see figure 3.31)). A unidirectional reinforcement is also tested, weft yarns extracted from M1 fabric and laboratory impregnated roving are investigated as reinforcement to be compared to the bidirectional fabrics M1 and M2 in order to investigate the role of the transversal yarn. The specimens tested in 4-point bending are detailed in table 3.3.

Table 3.3: Specimens tested in 4-point bending.

Reinforcement	**Longitudinal yarn**	**Cover distance** $[mm]$	**Number of specimens**	**Denomination**
M1	Weft	2	2	M1-We-2
M1	Warp	2	2	M1-Wa-2
M1	NA Mesh rotated at 45°	2	2	M1-45-2
M1	Weft	1	2	M1-We-1
M2	Weft	2	2	M2-We-2
Longitudinal yarns only Yarns extracted from M1	Weft	2	2	M1-L-2
Longitudinal yarns only Yarns impregnated in the laboratory	NA	2	2	L-2

Curing conditions After casting, the specimens are protected in the molds with several layers of cellophane films during 24 hours until demolding. Then, the specimens are stored in drying conditions in desiccators containing a magnesium chloride saturated solution that regulates the relative humidity inside the desiccator at 65% for 28 days until the mechanical test. The temperature in the desiccators is around 23°C ± 2°C.

3.4 X-ray in-situ mechanical characterization

To understand the cracking mechanisms of the reinforced rendering mortar and the reinforcement mechanisms of the fiber-glass mesh, several specimens are tested mechanically using 3-point and 4-point bending. The tests are performed in-situ X-ray tomography allowing to obtain 3D information of the cracked specimen. However, since the achievable image resolution is inversely proportional to the largest cross sectional dimension traversed by the X-rays, a classical horizontal bending set-up is not optimal. Thus, new inclined 3-point and 4-point bending set-ups are developed and are detailed thereafter in this section. In addition to avoiding buckling, these tests provide the advantage of measuring the actual bending force undergone by the specimens compared to the existing in-situ tests (cf. 3.2.4.2).

3.4.1 Experimental methods

The rendering mortar is subject to drying shrinkage or hygral swelling in case of a decrease or increase of the relative humidity of the surrounding air, respectively. In real life scenarios, only the external surface of the mortar will exchange humidity with the surrounding air. Therefore, only the external surface of the mortar will shrink or swell causing a "curling" effect [Chilwesa et al., 2019] of the mortar layer as shown in figure 3.16. Similar resulting loads can be obtained with restrained thermal strains in case of an increase or decrease of the surrounding external temperatures caused by a difference in the thermal expansion coefficient between the mortar α_m and the expanded polystyrene α_p (in general $\alpha_p > \alpha_m$). For these reasons, we opted for bending tests on the reinforced rendering mortar samples to represent the loading conditions of a mortar in a real life application.

The cracks in a rendering mortar can be initiated on two different levels:

- On the mesoscale, where the heterogeneities of the mortar (porosity, sand particles, and the mesh) are the sources of stress concentrations.
- On the structural scale, where the geometrical singularities such as window corners and thermal joints take the lead of the stress concentration and crack initiation.

And so, 4-point bending tests, on one hand, are representative of the cracking that takes place on facades without geometrical singularities where the heterogeneities of the mortar are the main crack initiators. On the other hand, 3-point bending tests are representative of the cracking that occurs on the geometrical singularities where the stress is localized.

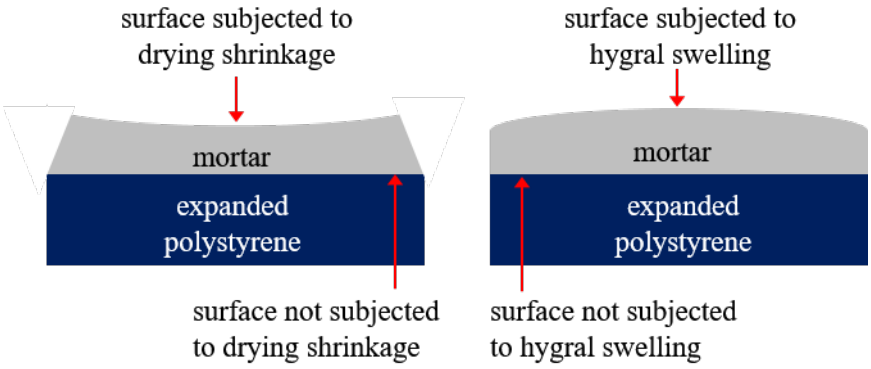

Figure 3.16: "Curling" effect in the rendering mortar in ETICS.

The dimensions of the specimen were chosen according to several parameters:

- The 5 mm thickness of the specimen is defined by the manufacturer of the mortar for industrial application in ETICS.
- The 12 mm width is chosen according to a minimum of 3 longitudinal yarns of the glass fiber mesh.

- The length is chosen to respect (i) the minimum slenderness of Euler-Bernoulli theory, thus a minimum of 50 mm is required, (ii) a minimum of 5 transversal yarns of the glass fiber mesh in the zone of interest (between the loading application points), thus 30 mm is required for the zone of interest, (iii) a minimum anchor length is required for the glass finer mesh (calculated according to a reference stress in the mesh supposing a perfect adhesion between the mortar and the glass fiber mesh), (iv) and a sufficient image resolution is required (the voxel size should be smaller than the visible crack width). Considering the 50 µm capacity of the human vision, at 1 m distance as a reference for a visible crack width of 50 µm, and a 3D image size around 1000 voxels, the maximum length allowed to be traversed by the X-rays should be 50 mm. Note that inclining the specimen allows to relax this constraint by choosing a sufficiently long specimen, hence respecting Euler-Bernoulli hypothesis, while decreasing the length traversed by the X-rays.

- All dimensions have to be greater than the Representative Elementary Volume (REV) dimensions. Nevertheless, the thickness of the material is defined by the industrial manufacturer.

Note that verifications of the inclined bending set-up have been carried-out using finite element calculations. On the other hand, a vertical bending setup has been considered (e.g. the vertical bending set-up shown in figure 3.10 and used by the the author [Tsitova, 2022]). Nevertheless, the applied forced is not measured and a buckling may occur for the chosen length of the specimen.

3.4.1.1 3-point bending experimental set-up

The specimen in this particular 3-point bending setup, unlike in traditional ones, is inclined. This change is what allowed us to obtain better quality images since the X-ray beam is traversing a smaller distance in the "scanned zone" shown in figure 3.17 compared to the total length of the specimen in case of a non-inclined bending setup. This can be related to the equations 3.1 and 3.2 whereas the larger x_i, the smaller the transmitted beam intensity I.

In figure 3.17 detailing the inclined 3-point bending set-up, the plate 7 is directly fixed to a 100 N load cell that will put the plate in an upward movement, hence the load is being transmitted to the specimen by the lower supports (element 2 of figure 3.17). Note that supports 2, 3, 4, and 5 of figure 3.17 are made of PMMA (poly(methyl methacrylate)) which has a density of about 1185 kg·m^{-3}. The density of the mortar being 1323 ± 5 kg·m^{-3} (mean value ± standard deviation) making it denser than the PMMA. Thus, the PMMA is more X-ray transparent.

The test is controlled by the displacement of the plate 7 at a rate of 1 µm.s^{-1}. The advantage of using a displacement controlled test compared to a load controlled one is that the former allows getting the post-peak curve and prevents creep strains during the scans that will complicate the analysis of displacement fields related to cracking. Two scans are done to compare the cracked stage of the sample to its slightly deformed elastic stage. Before each scan, a pause period is preferred to allow the material to relax. This relaxation period prevents differential strains (for instance between viscous cement paste and elastic aggregates)

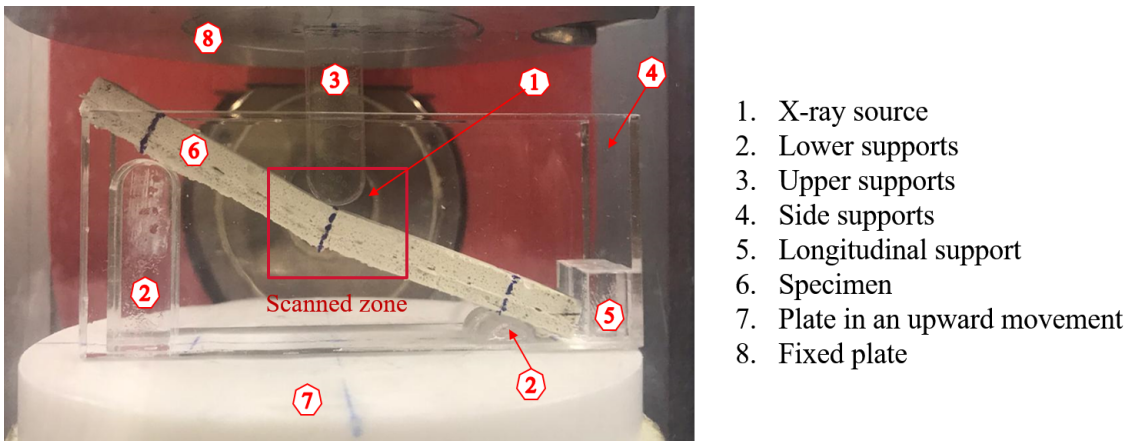

Figure 3.17: 3-point bending mechanical assembly.

that will occur during the scan hence limiting the blurred image. The in-situ inclined 3-point bending test is divided into 6 phases that are detailed in figure 3.18. The specimen is loaded until contact (phase1), the load is stopped and a relaxation period (phase 2) is required before the first scan (phase 3) of the slightly deformed non-cracked specimen. After the first scan, the specimen is loaded until the crack (phase 4) noticed by a sudden load drop, the load is stopped and a relaxation period (phase 5) is required before the scan of the cracked sample (phase 6).

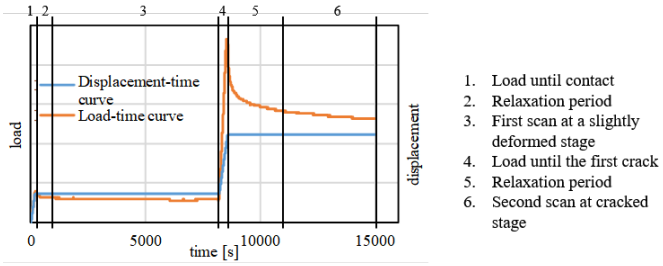

Figure 3.18: The schematic course of the 3-point bending test described with the load vs. time and displacement vs. time curves.

3.4.1.2 4-point bending experimental set-up

Similarly to the 3-point bending set-up, the 4-point bending set-up is also inclined and is detailed in figure 3.20. Note that all the pieces of the assembly are made using the 3D printing technique of ABS (Acrylonitrile Butadiene Styrene) which has a density of about 1055 kg.m^{-3}. The density of the mortar being 1323 $\pm$ 5 kg.m^{-3} (mean value $\pm$ standard deviation) making it denser than the ABS. Thus, the ABS is more X-ray transparent.

Depending on the availability of the X-ray tomograph, the tests are conducted either in the Laboratory of Mechanics of Paris-Saclay either in Saint-Gobain Research Paris. For this reason two different loading cells are used, either a 100 N load cell (the same used for the 3-point bending tests) fixed directly to the lower plate (element 5 of figure 3.20), either to a

20 kN load cell fixed to the upper plate of the set-up (element 6 of figure 3.20). In the case of the 20 kN load cell, since the accuracy of the load measurement is not sufficient to detect the variations of the load applied on the specimens, three 50 N sensors are placed underneath the set-up to measure the load as shown in figure 3.19. In addition, different image resolution has been adopted. The volumes obtained in Saint-Gobain Research Paris have a voxel size of around 15 µm and those obtained in Laboratory of Mechanics of Paris-Saclay have a voxel size of around 40 µm.

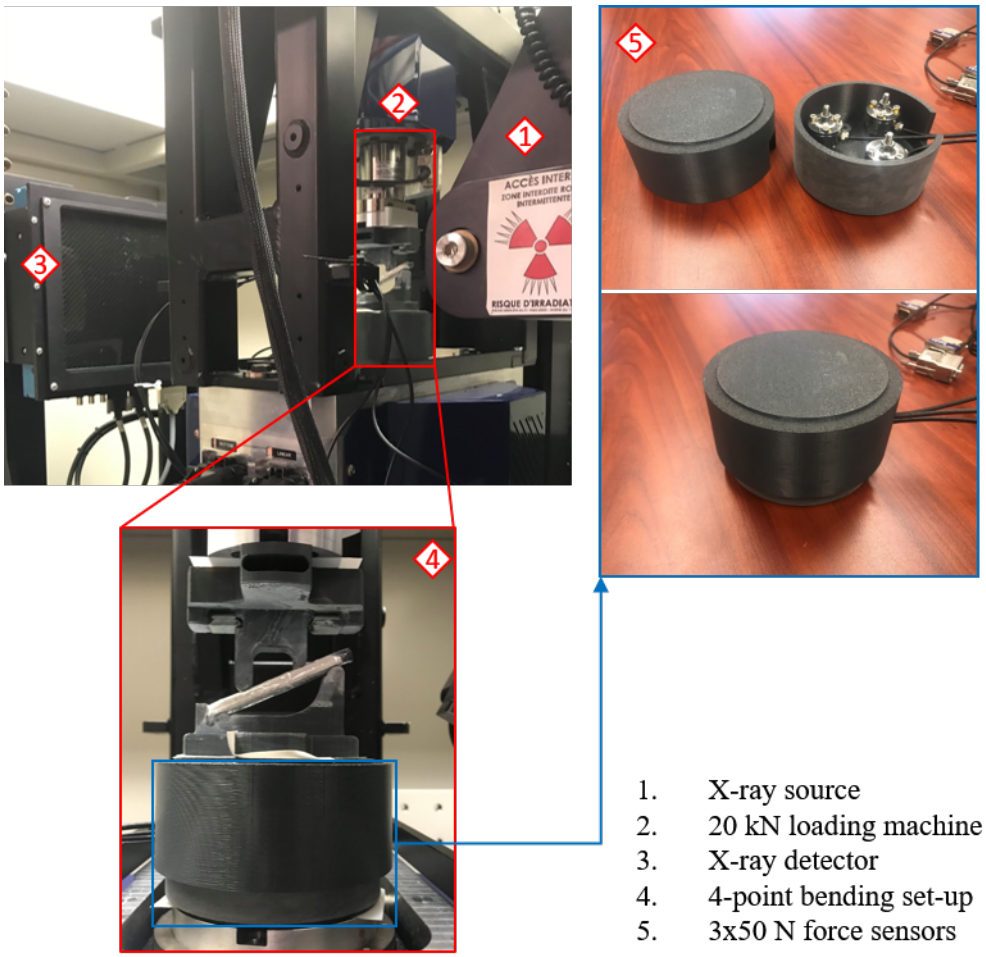

Figure 3.19: 4-point bending set-up in the X-ray tomograph of the Laboratory of Mechanics of Paris-Saclay.

In both cases, the test is displacement controlled at a rate of 1 µm.s^{-1}. The course of the test is similar to the 3-point bending test course shown in figure 3.18. However, since the specimen is expected to multi-crack under 4-point testing as opposed to the 3-point bending load, phases 4, 5, and 6 of figure 3.18 are repeated for every time a crack is detected noticed by a sudden load decrease. Thus, a first scan of the slightly deformed sample at its elastic stage is carried out (phase 3 of figure 3.18), then, a scan is carried out after the appearance of a crack during the multi-cracking phase. In addition, a continuous radiography acquisition (around 2 images/s) is performed during the whole loading history, thus allowing to obtain precious

2D information of the specimen evolution that can be analyzed by Digital Image Correlation (DIC). Note that during all tests (3-point and 4-point bending), the specimens are protected with cellophane film to prevent drying and avoid any strains caused by drying shrinkage.

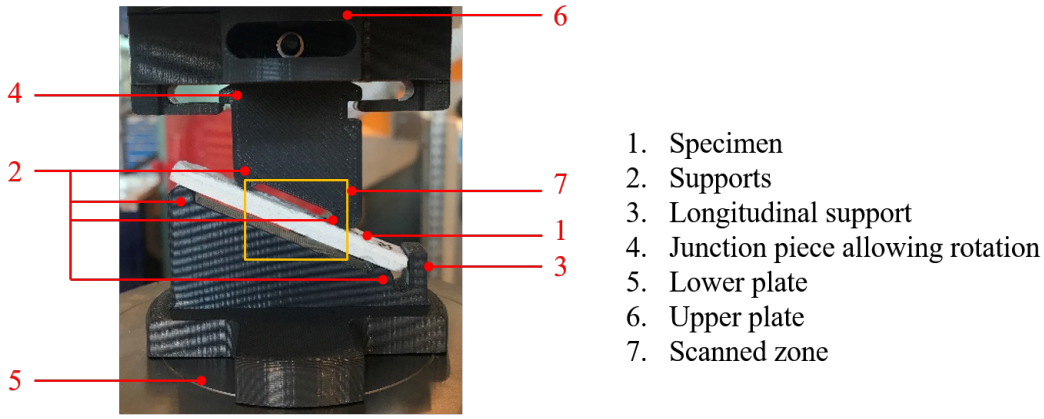

Figure 3.20: 4-point bending mechanical assembly.

3.4.2 Results and discussions

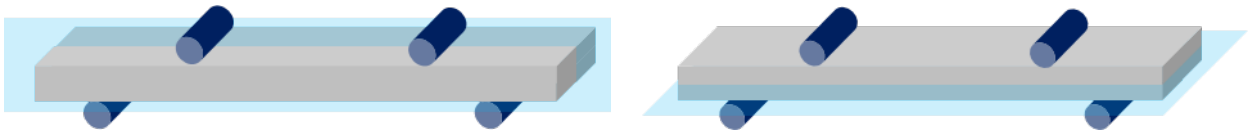

(a) (b)

Figure 3.21: Representation of a (a) vertical and (b) horizontal section inside the reconstructed 3D volume of the sample.

3.4.2.1 In-situ 3-point bending

In a 3-point bending test, considering a homogeneous sample, the crack initiation is theoretically known to be exactly under the middle-upper support where the moment is maximum. The crack will propagate, from the bottom surface in tension toward the upper surface, vertically due to the geometrical and mechanical symmetry of the classical 3-point bending set-up. This theoretical cracking pattern is not obtained in our 3-point bending tests. The crack trajectory is neither located under the middle-upper support nor vertical. It is slightly shifted from the center and inclined as shown in figure 3.22.

The theoretical cracking trajectory described above refers to a homogeneous material and therefore does not apply directly to heterogeneous materials. In heterogeneous materials, the mechanical properties (elastic constants, strength) are heterogeneous fields depending on the constituent phases spacial distribution. Such material field heterogeneity disturbs the

preferential sites for crack initiation and redirect its propagation. In the reinforced fiber-glass mortar samples, three main categories of heterogeneities exist at the millimeter scale: (macro)porosity, sand grains (two types of sand can be differentiated), and the fiber-glass mesh. Material field heterogeneity results in a broadening of stress distribution in random heterogeneous materials [Honorio et al., 2018]. The interface between inclusions and matrix is a zone sensible to stress concentration due to property mismatch. The crack in the mortar matrix is initiated wherever the local stress attains the mortar's tensile strength, hence not exactly on the lower surface of the sample as in homogeneous materials, but in a domain in the vicinity of the most tension-load zone (the size of this domain being related to the characteristic size of the heterogeneities). Figure 3.24 shows that under a given tensile load, stress concentration, due to the presence of a rigid inclusion (compared to mortar rigidity), perturbs cracking propagation differently from a softer inclusion (e.g. pore). Considering the quasi-brittle behavior of the mortar, the propagation of the crack once initiated is rapid. Since the acquisition of 3D X-ray images requires a steady-state of the scanned object hence cannot be carried out during the mechanical test but afterwards, the exact location of the crack initiation cannot be determined. The vertical sections shown in 3.22 show the critical influence of the porosity and sand grains on the trajectory of the crack: (i) it is clear how the crack preferentially passes through several porosities on its way; (ii) sand grains, on the other hand, are not crossed by the crack (the cracks are preferentially located at the cement paste/sand grains interface). The fiber-glass fabric plays an important role as well.

The cracks in both samples of figure 3.22 did not cross the fiber-glass mesh. The crack stopped at the level of the mesh in the case of the sample M1-30-M as shown in figure 3.22b. However, in the case of M1-3P sample, the vertical crack stops at the level of the mesh and split to propagate horizontally along the mesh as shown in figure 3.22a. The fiberglass mesh stops the crack propagation and thus limits the crack opening. This first reinforcement mechanism directly influences the durability of the ETICS. As discussed in the introduction, the potential water leakage is limited by the smaller crack opening. In the reinforced mortar, emerging cracks should not easily attain the thermal insulator since they do not propagate through the entire thickness of the mortar. This is confirmed by the horizontal sections located above the mesh in figure 3.23, since no cracks are visible above the mesh.

Further, the analysis of specimen M1-3P-M of figures 3.22b and 3.23b suggests a potential influence of the transversal yarn on the localization of the crack since the crack is located on the middle transversal yarn. Nevertheless, this observation does not apply on the M1-3P sample, the crack is located between two transversal yarns as shown in figures 3.22a and 3.23a. It is difficult to presume, based on the 3-point bending test, that the transversal yarn will locate the crack in the mortar because of the maximal bending moment in the middle of the sample. This potential mechanism, that will be further investigated using 4-point bending (results of 4-point bending tests are discussed in the next section 3.4.2.2), might have a relevant impact on the cracking pattern.

3.4.2.2 In-situ 4-point bending

In a 4-point bending test, considering the constant bending moment between the two upper supports, the crack can be initiated on the lower tensile surface anywhere between the two

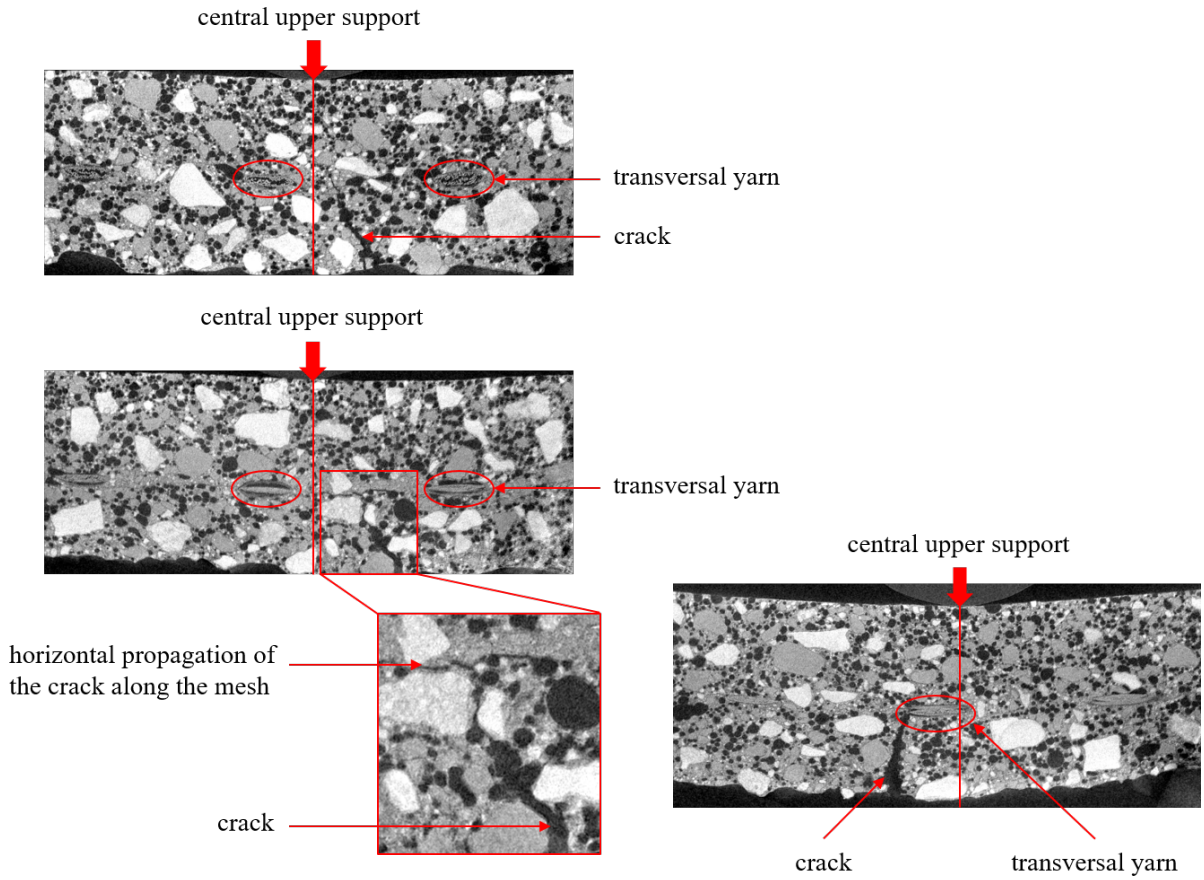

(a) M1-3P (b) M1-3P-M

Figure 3.22: Vertical sections inside the reconstructed volume of the cracked samples (a) M1-3P and (b) M1-3P-M.

upper supports. The crack will propagate, from the bottom surface in tension toward the upper surface, vertically due to the geometrical and mechanical symmetry of the classical 4-point bending set-up. However, as discussed above for the three point bending tests in the previous section 3.4.2.1, the inclusionary heterogeneities can induce stress concentrations within the tensile zone as shown in figure 3.24. In this section, vertical and horizontal sections of the specimens (see figure 3.21) tested in 4-point bending are shown. The effect of the mesh (i.e M1, M2, or the longitudinal yarns), of the cover distance (the distance between the mesh and the lower tensile surface), and the direction of the mesh within the specimen (i.e. the weft yarn in longitudinal direction, the warp yarn in the longitudinal direction, or neither the mesh is rotated at 45° within the specimen) on the cracking of the reinforced mortar specimens, in terms of the first cracking load, the number of cracks, and the localization of the cracks, are investigated. The aim is to understand the cracking mechanisms of the reinforced mortar and the reinforcement mechanisms of the fiberglass mesh. Table 3.4 details the first crack load (mean value ± standard deviation), the number of cracks, and the localization of the cracks with respect to the transversal yarn of the specimens. The force vs. time curves of the tests of some of the specimens is shown in figure 3.25.

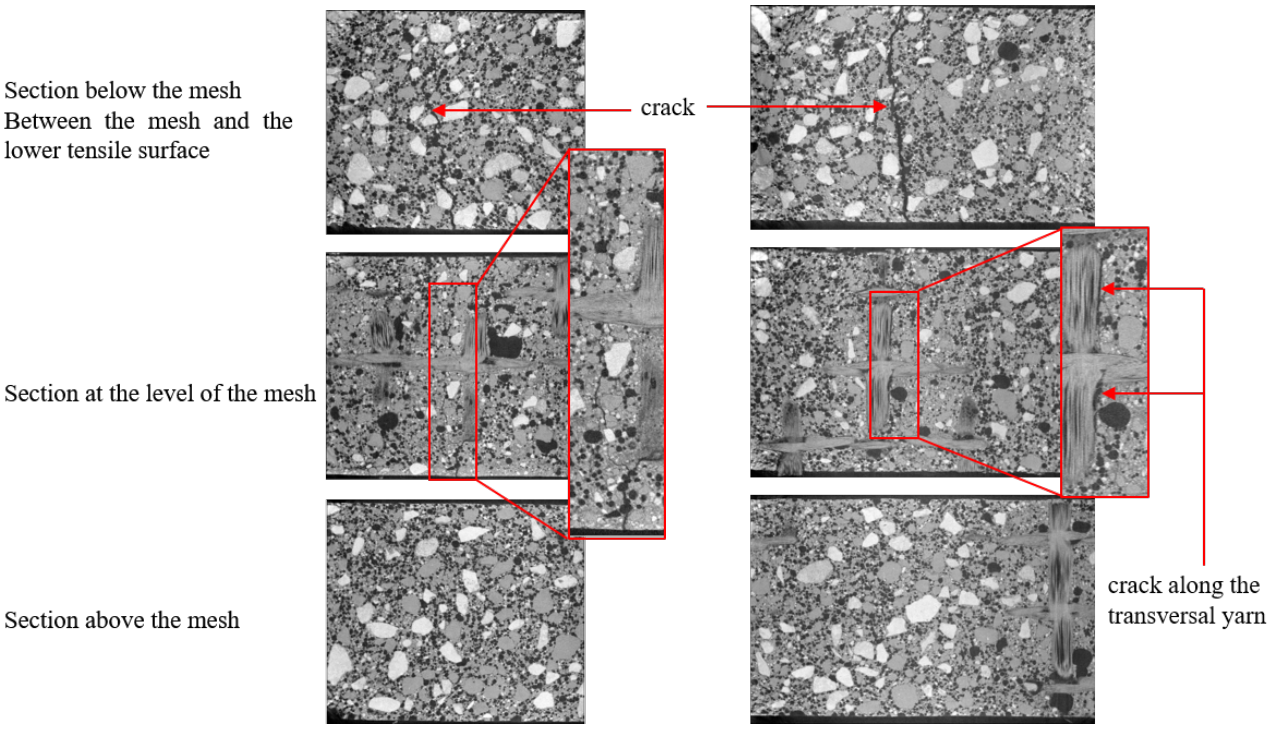

(a) M1-3P (b) M1-3P-M

Figure 3.23: Horizontal sections inside the reconstructed volume of the cracked samples (a) M1-3P and (b) M1-3P-M.

Table 3.4: First crack force (mean value ± standard deviation), the number of cracks (at the end of the test when the specimen touches the lower plate), and the location of the crack with respect to the transversal yarns in the tested specimens.

Specimen	**Number of specimens**	**First crack force [N]**	**Number of cracks**	**Cracks located on a transversal yarn**
M1-We-2	4	11.02 ± 1.94	2	mainly located on a transversal yarn
M1-Wa-2	1	11.6	1	located on a transversal yarn
M1-45-2	2	11.1 ± 0.84	1	NA
M1-We-1	3	16.48 ± 4.9	3	mainly located on a transversal yarn
M2-We-2	2	10.33 ± 1.37	2	not located on a transversal yarn
M1-L-2	2	12.18 ± 1.57	2	NA
L-2	2	13.93 ± 2.43	1	NA

Effect of fabric properties: To study the effect of the mesh, specimens reinforced with fabric M1 (i.e. M1-We-2) are compared to those reinforced with fabric M2 (i.e. M2-We-2).

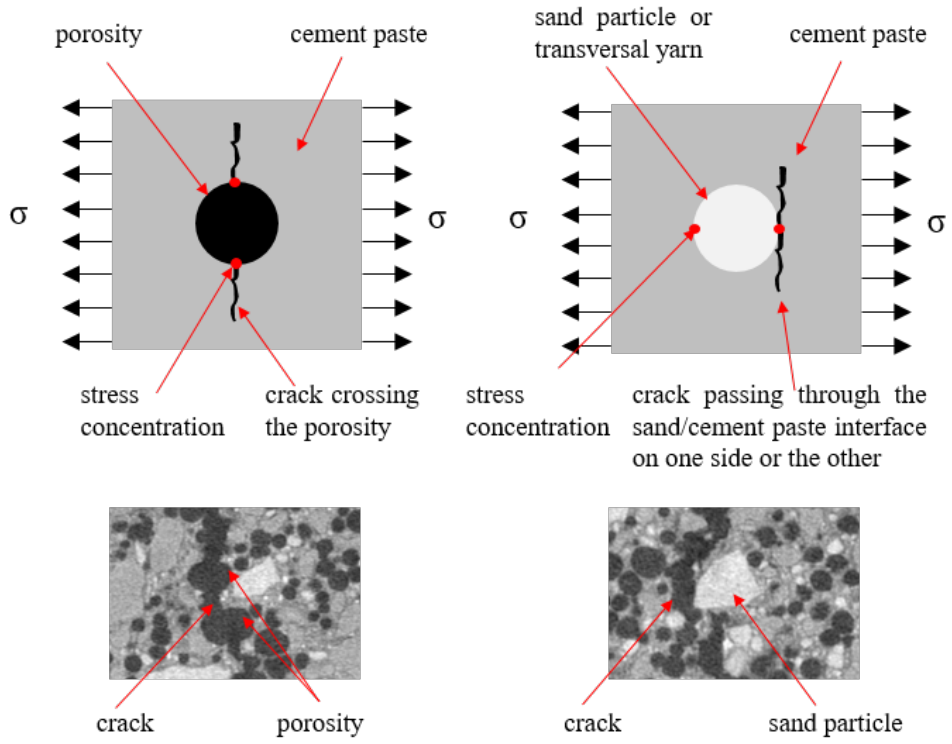

Figure 3.24: Representation of the stress concentration caused by the heterogeneities in the mortar.

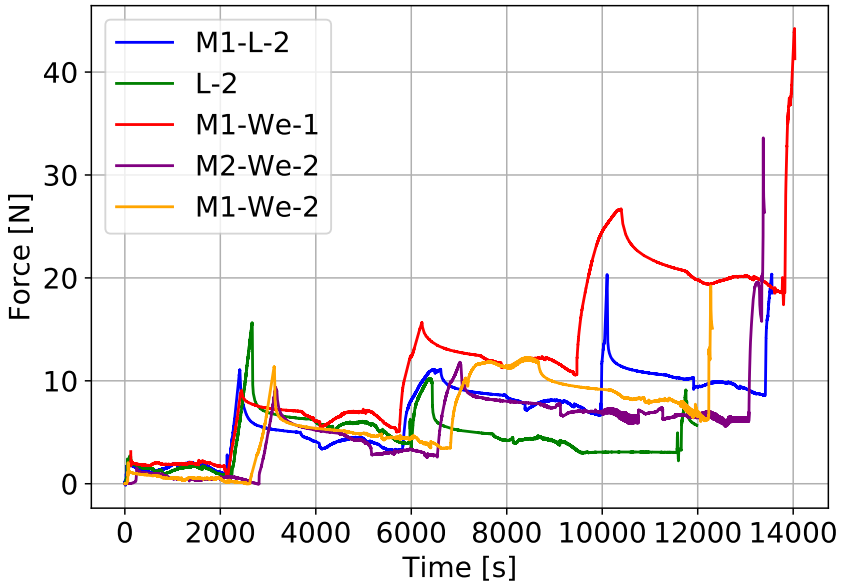

Figure 3.25: Force vs. time curves of some of the tested specimens in 4-point bending.

The main differences between fabrics M1 and M2 are the density of the fabric and the weft and warp spacing. M2 is denser than M1 (see table 3.1) hence the yarns of M2 fabric are

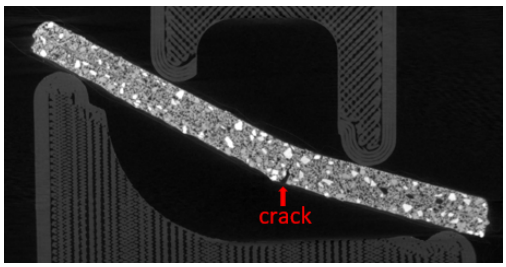

(a) Vertical section - Specimen 1

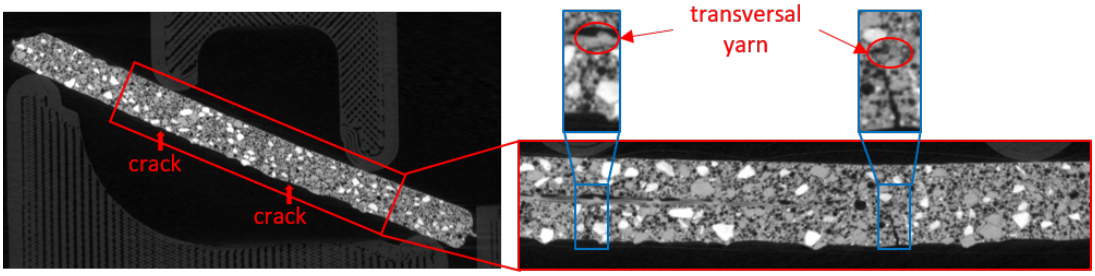

(b) Vertical section - Specimen 2

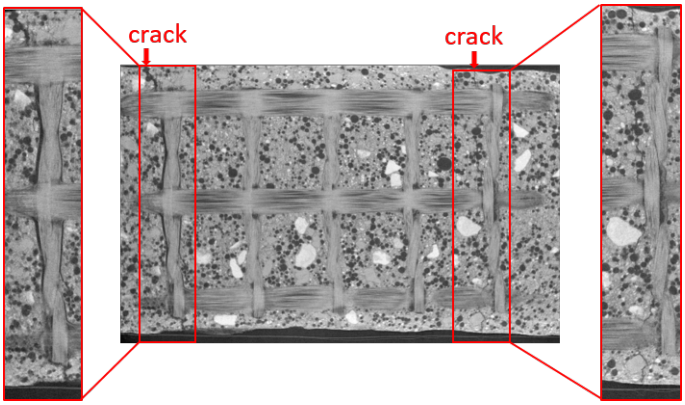

(c) Horizontal section - Specimen 3

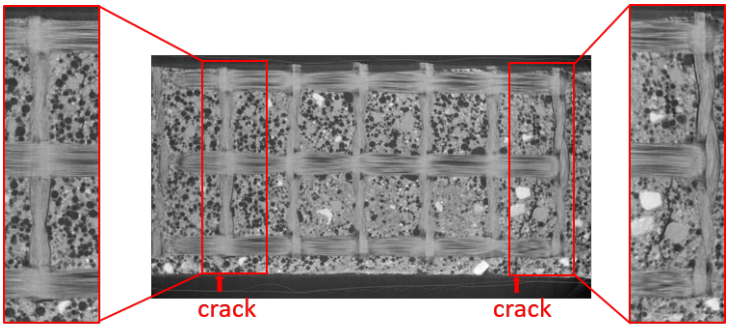

(d) Horizontal section - Specimen 4

Figure 3.26: Sections inside the reconstructed volume of the cracked M1-We-2 samples: (a) Vertical section - Specimen 1, (b) Vertical section - Specimen 2, (c) Horizontal section - Specimen 3, and (d) Horizontal section - Specimen 4.

thicker. In addition, the spacing between the weft yarns and warp yarns is greater in the case of M2 fabric (see table 3.1 and figure 3.13).

- When comparing the first crack force of specimens M1-We-2 and M2-We-2 detailed in table 3.4, although the difference is not significant given the standard deviation, it is noticed that the first crack force of specimens M2-We-2 is slightly lower than that of M1-We-2 (10.33 ± 1.37 for M2-We-2 compared to 11.02 ± 1.94 for M1-We-2). An analytical calculation detailed in section 3.4.2.4, shows that the greater the section of the longitudinal yarn (i.e. the greater the thickness of the mesh), the greater the first crack bending moment (see figure 3.40a). In the case of the tested specimens, the hypothesis considered for the analytical calculation are not applicable. This result shows that a thicker mesh, if used to delay the appearance of cracks in the rendering mortar, will not provide the desired outcome. In the literature as in the work of [Yao et al., 2015], the textile reinforced mortar shows a first crack stress that is significantly greater than that of a plain mortar. Although the reinforcing fabric may delay the appearance of the crack in reinforced mortars when compared to a non-reinforced mortar, a greater reinforcement ratio (a thicker and denser fabric) does not provide a greater tensile strength to composite materials when compared to a lighter fabric.

- On the other hand, as shown in table 3.4 and in figures 3.26 and 3.27, both M1-We-2 and M2-We-2 specimens exhibits 2 cracks during the tests. This means that both fabrics provide somewhat the same load transmission between the matrix and the mesh. The transversal yarns provide mechanical anchorage that can increase the load transmission. The transversal yarns of M2 are thicker than M1 fabric. Thus, the anchorage effect provided by the tranversal yarns of M2 fabric is expected to be more important. However, the latter seems to be weakened by the smaller number of transversal yarns in M2-We-2 specimens compared to M1-We-2 specimens (the warp spacing of M2 fabric is greater than that of M1 fabric). The crack width model of the ACI code [Frosch, 1999] illustrates the influence of the transversal bar spacing on the crack spacing and width (cf. appendix C.

Effect of the transversal yarn: The transversal yarn may play a double role within the specimen. On one hand, it can provide a mechanical anchorage in the matrix that prevents sliding of the textile and promotes the load transmission between the matrix and the fabric. This is particularly important for obtaining multiple small-width cracks as opposed to one wide crack obtained when the load transmission between the mortar and the fabric is weak. On the other hand, the transversal yarn can also act as a defect in the matrix and induce stress concentrations (see figure 3.24) affecting negatively the tensile strength of the composite.
To study the effect of the transversal yarn, M1-We-2 specimens reinforced with M1 fabric, M1-L-2 specimens reinforced with longitudinal weft yarns extracted from the fabric M1, L-2 specimens reinforced with longitudinal roving yarns (impregnated with the same coating in the laboratory and having the same density as the M1 weft yarn) are tested.

- Table 3.4 detailing the first crack force of the tested specimens, shows that the first crack force of specimens M1-L-2 and specimens L-2 (12.18 ±1.57 N and 13.93 ± 2.43 N

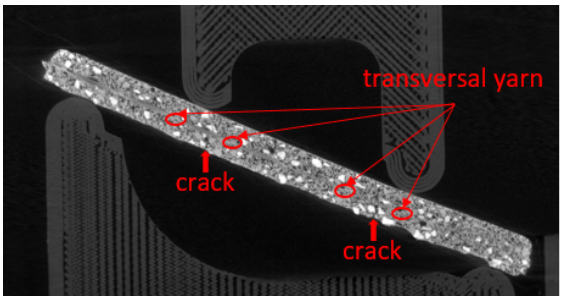

(a) Vertical section - Specimen 1

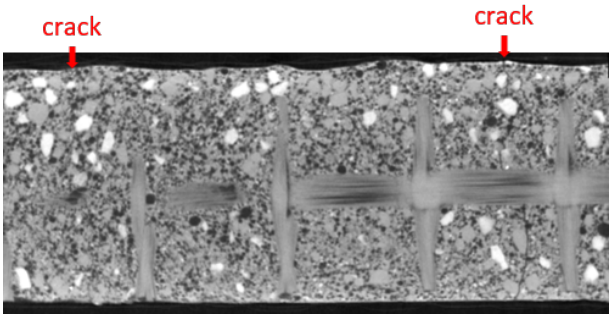

(b) Horizontal section - Specimen 1

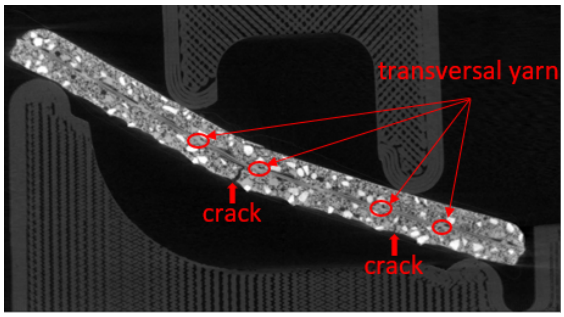

(c) Vertical section - Specimen 2

Figure 3.27: Sections inside the reconstructed volume of the cracked M2-We-2 samples: (a) vertical section - Specimen 1, (b) horizontal section - Specimen 1, and (c) vertical section - Specimen 2.

respectively) is greater than that of M1-We-2 specimens (11.02 ± 1.94 N). This observation suggests that the presence of the transversal yarn (the case of M1-We-2 specimens as opposed to M1-L-2 and L-2 specimens) induces weak point and stress concentration that can decrease the tensile strength of the composite. However, the difference is not significant given the scatter of the first crack force measurement. The transversal yarn does not seem to affect the first crack load. The stress concentration induced by the transversal yarn is most likely to be blurred by the numerous stress concentrations of the heterogeneities.

- Specimens M1-We-2 exhibit 2 cracks during the load with the exception of specimen 1 as shown in figure 3.26. On the contrary, specimens L-2 exhibit only one crack during the load as shown in figure 3.30. The absence of the transversal yarns in the case of L-2 specimens results in the appearance of only one crack during a 4-point bending load. This highlights the important role of the transversal yarns as mechanical anchorage increasing the load transmission between the mortar and the fabric favoring the appearance of multiple cracks.
  Specimens M1-L-2 shown in figure 3.29 exhibits 2 cracks. However, it is noticed that the second crack appeared at a late stage during the loading (high deflection and a very wide first crack). The absence of the transversal yarn is somewhat compensated by the morphology of the weft yarn of the M1 fabric. Figure 3.28a shows the intersection of

the weft and the warp yarns of the M1 mesh. It is noticed that the thickness of the weft yarn at the intersection is the smallest. Thus, the weft yarns extracted from the M1 fabric, as opposed to the smooth roving yarns, present a systematically variable thickness creating a rough surface noticed in figure 3.28b. The rough surface increases the load transmission allowing the appearance of the late second crack.

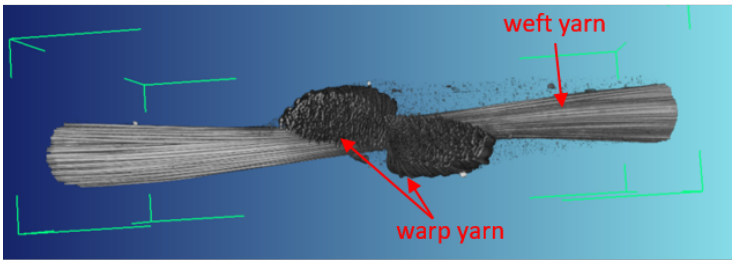

(a)

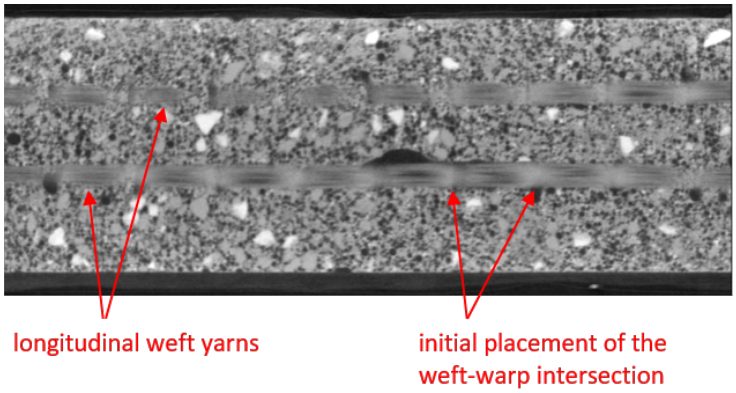

(b)

Figure 3.28: (a) 3D X-ray reconstructed volume of a warp-weft intersection of M1 fabric (after thresholding to eliminate the coating); (b) Horizontal section inside the reconstructed volume of a M1-L-2 sample.

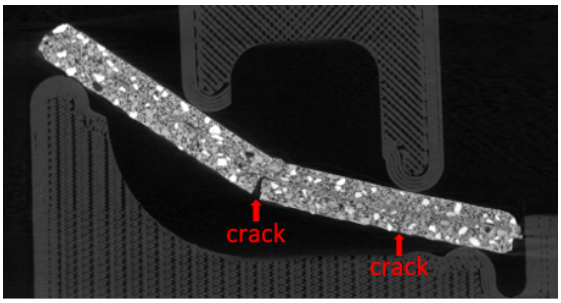

(a) Specimen 1

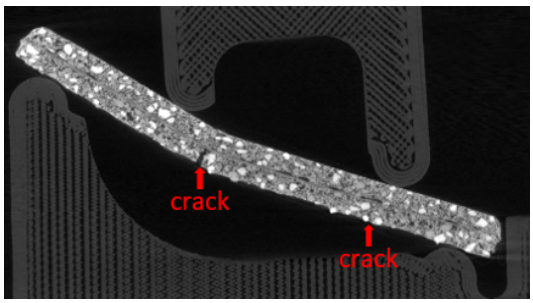

(b) Specimen 2

Figure 3.29: Vertical sections inside the reconstructed volume of the cracked M1-L-2 samples: (a) Specimen 1 and (b) Specimen 2.

In addition, the transversal yarn may have an effect on the localization of the crack. In the case of M1-We-2 specimens, as shown in figures 3.26b and 3.26c, the cracks are located on the level of the transversal yarns. In figure 3.26d, it is noticed that cracks are located on the transversal yarns, however they are not aligned on them as they are inclined in the horizontal surface. This is also the case for the M1-Wa-2 specimen shown in figure 3.33. Although not perfectly aligned on the transversal yarn, the crack is localized on the latter. In the case of M1-We-1 specimens that exhibits 3 cracks, as shown in figures 3.35a and 3.35c, two of the cracks are located on transversal yarns while the third is not. Generally, the transversal yarns seem to localize the cracks. Nevertheless, it is not the case for M2-We-2 specimens. Figures 3.27a, 3.27b, and 3.27c show that none of the cracks is located on the transversal yarns. It is expected that, since the thicker transversal yarns of the mesh M2 induce higher stress concentrations, the tranversal yarns will localize the cracks. However, the spacing between the warp transversal yarns of M2 fabric is greater than that of M1 fabric, leaving more room for the heterogeneities of the mortar to influence the crack localization and propagation.

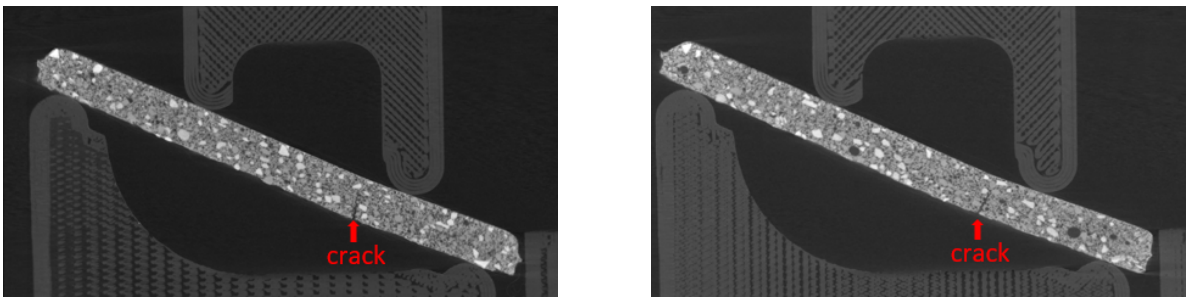

(a) Specimen 1 (b) Specimen 2

Figure 3.30: Vertical sections inside the reconstructed volume of the cracked L-2 samples: (a) Specimen 1 and (b) Specimen 2.

Effect of the mesh direction within the specimen: M1 fabric has been placed in 3 different directions within the specimens. The weft yarns are placed in the longitudinal direction in M1-We-2 specimens, the warp yarns are placed in the longitudinal direction in M1-Wa-2 specimens, and M1 fabric is rotated at 45° in M1-45-2 specimens as shown in figure 3.31.

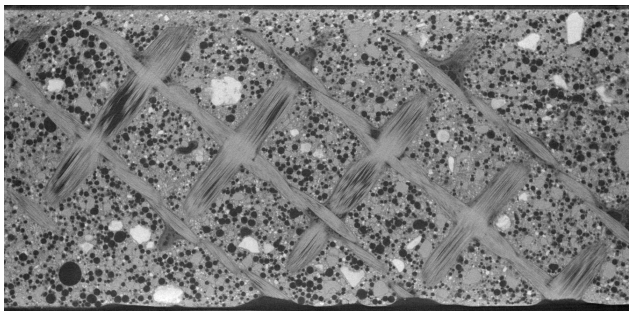

Figure 3.31: Horizontal section inside the reconstructed volume of a M1-45-2 sample.

- The direction of the mesh does not seem to have an impact on the first crack force as shown in table 3.4 (11.02 ± 1.94 N for M1-We-2 specimens, 11.6 N for M1-Wa-2 specimen, and 11.1 ± 0.84 N for M1-45-2 specimens).

- Regarding the number of cracks during the bending load, the weft yarn in the longitudinal direction, as it is the case for M1-We-2 (figure 3.26), induces the more cracks compared to other direction of the mesh (specimens M1-Wa-2 in figure 3.33 and M1-45-2 in figure 3.34). In the case of M1-45-2 specimens, the mesh is solicited in shearing which is its weak point. For this reason, after the first crack when the load is transmitted to the mesh, the latter falls apart which is translated in the absence of the post-crack stiffening usually observed in TRMs as shown in figure 3.32. On the other hand, the absence of the multi-cracking in the case of M1-Wa-2 specimens can be explaned by the differnce in the yarn morphology between the weft and warp yarns. However, since only one M1-Wa-2 specimen has been tested, this conclusions can not be confirmed.

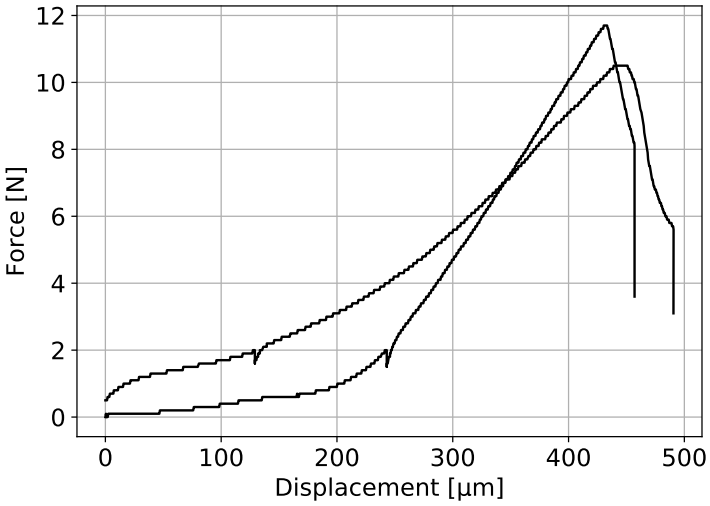

Figure 3.32: Force vs. displacement of M1-45-2 specimens.

Effect of the cover distance: To study the effect of the cover distance, the same fabric M1 is placed at either 2 mm from the lower tensile surface (specimens M1-We-2) or 1 mm from the lower tensile surface (specimens M1-We-1).

- The first crack load of the M1-We-1 specimens is greater than that of M1-We-2 specimens (16.48 ± 4.9 N and 11.02 ± 1.94 N respectively as shown in table 3.4). A simple analytical calculation detailed in section 3.4.2.4 shows that the first crack bending moment increases when the cover distance decreases (when the reinforcement is placed closer to the tensile surface)(see figure 3.40b). This suggests that, to delay the appearance of cracks in the rendering mortar, the reinforcing fabric needs to be placed the closest possible to the external surface [1]. However, the scatter related to the first crack force shows that the

[1]Note that as sufficient cover distance is needed to cover the mesh and allow a matrix/fabric load transmission

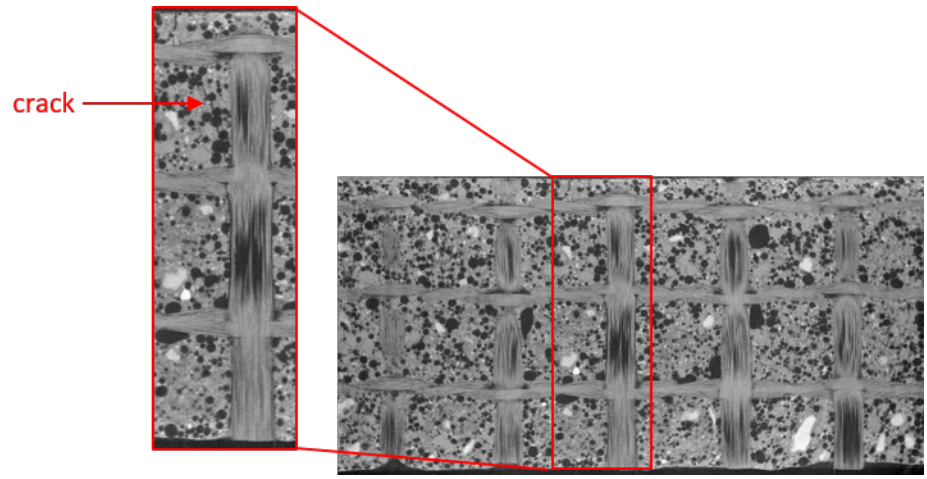

(a) On the level of the mesh

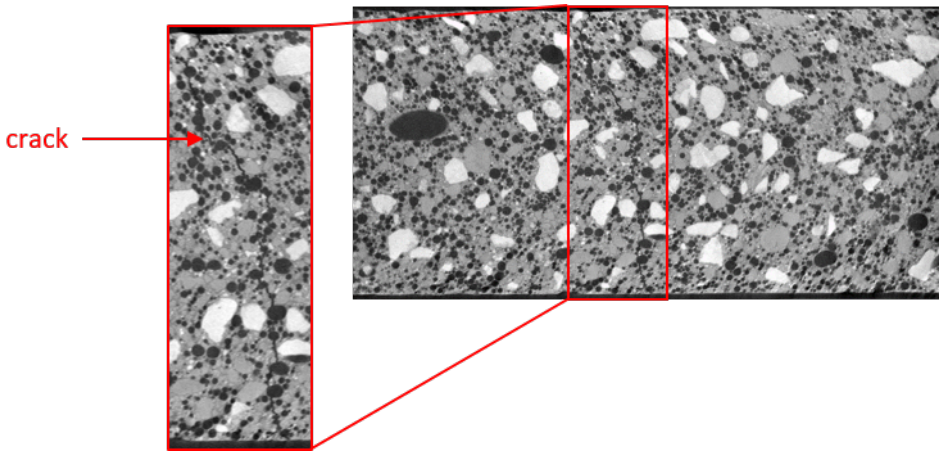

(b) Underneath the mesh (between the mesh and the lower tensile surface)

Figure 3.33: Horizontal sections inside the reconstructed volume of the cracked M1-Wa-2 sample: (a) on the level of the mesh and (b) underneath the mesh (between the mesh and the lower tensile surface).

heterogeneous microstructure of the mortar (some heterogeneities can attain the order of size of a mm) plays an important role as well. A large porosity in the tensile zone for example can lower the tensile strength of the composite despite the presence of the mesh close enough to the tensile surface.

- Specimens M1-We-1 exhibit 3 cracks each during the load as shown in figure 3.35. On the other side, specimens M1-We-2 exhibit only 2 cracks each as shown in figure 3.26. This information is also summarized in table 3.4. This shows that when placed closer to the lower tensile surface, the mesh enhances the multi-cracking of the specimen. According to the crack prediction of the Model Code [Taerwe et al., 2013] and to the Eurocode 2 [EN, 1992] detailed in appendix C, the crack spacing is proportional to the cover distance and the crack width is proportional to crack spacing. This means, that when the reinforcement is placed closer to tensile surface, the number of cracks is greater

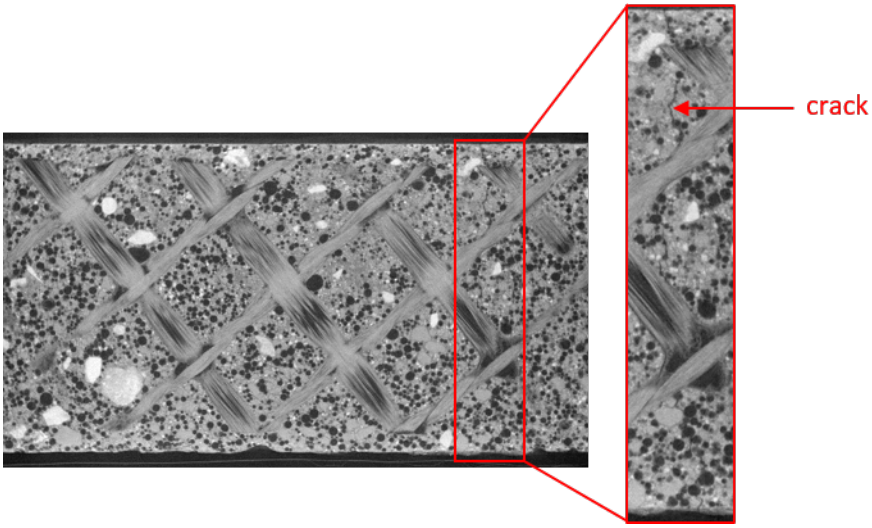

(a) Specimen 1

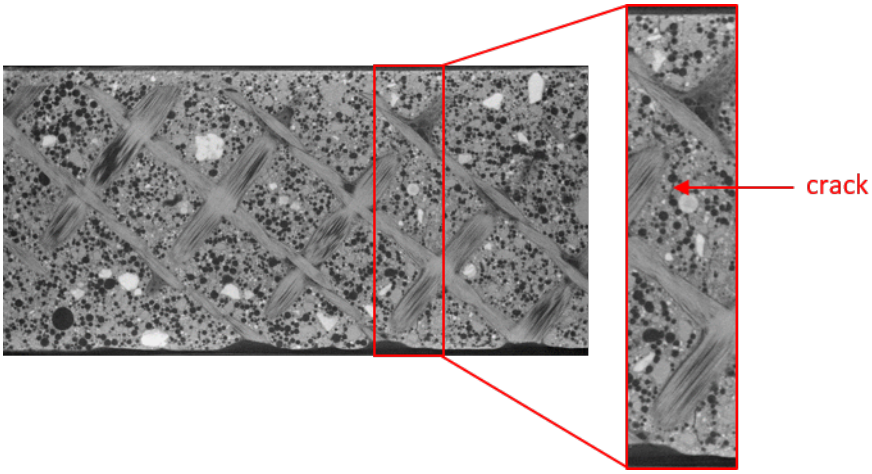

(b) Specimen 2

Figure 3.34: Horizontal sections inside the reconstructed volume of the cracked M1-45-2 samples: (a) specimen 1 and (b) specimen 2.

hence the crack spacing is smaller resulting in smaller crack width. For this reason, and since the multi-cracking favors smaller crack width, the mesh is preferred to be placed as closer as possible to the tensile surface.

Propagation of the crack: In most of the cases, the crack does not cross the mesh. The latter has the ability to stop the propagation of the mesh at its level thus limits the crack opening. This reinforcement mechanism directly influences the durability of the ETICS since the potential water leakage is limited by the smaller crack opening. In the reinforced mortar, emerging cracks should not easily attain the thermal insulator since they do not propagate through the entire thickness of the mortar. However, in some cases, as in the case of a M1-We-2 specimen shown in figure 3.36, the crack traversed the glass fiber mesh trough the thickness of the mortar, but never attained the upper surface. Nevertheless, the glass fiber mesh decreased

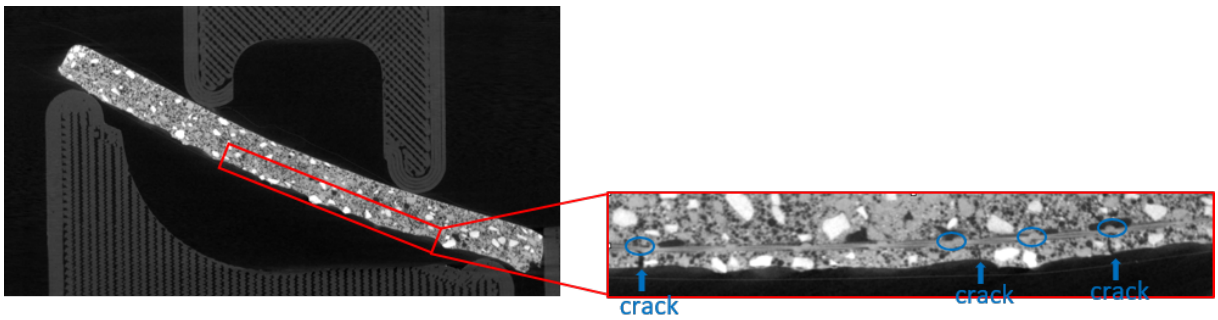

(a) Vertical section - Specimen 1

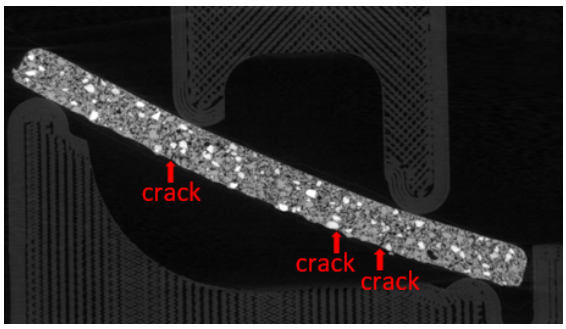

(b) Vertical section - Specimen 3

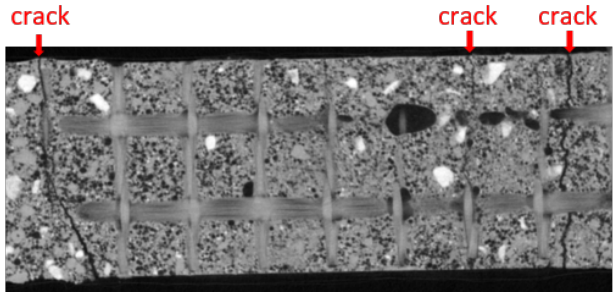

(c) Horizontal section - Specimen 3

Figure 3.35: Sections inside the reconstructed volume of the cracked M1-We-1 samples: (a) vertical section - Specimen 1, (b) vertical section - Specimen 3, and (c) horizontal section - Specimen 3.

significantly the crack opening (by 50% from 140 µm just beneath the mesh to 70 µm just above the mesh). This shows again the efficiency of the mesh to limit the crack propagation and reduce crack widths increasing the durability of ETICS.

3.4.2.3 Digital Image Correlation

During each of the loading periods of the experiments, radiographs are collected to obtain continuous 3D information averaged on the width of the specimen rather than the 3D volume obtained only when the loading is stopped. The radiographs are then processed by the Digital Image Correlation (DIC) method. The aim of this procedure is to investigate whether it is possible to determine the crack initiation location (i.e. the lower tensile surface or the mesh).

Image correlation consists in calculating the displacement field u in pixels x in the region of interest (ROI) by comparing a reference image $f(x)$ and a deformed image $g(x)$ [Hild and Roux, 2008]. $u(x)$ is calculated in equation 3.4 based on the conservation of gray levels expressed in equation 3.3. In the present study, DIC is carried out using Correli-RT3 [Tomičevć et al., 2013] developed at LMPS Laboratory. It performs global DIC analysis using finite element mesh with linear triangular elements and introduces mechanical regularization [Tomičevć et al., 2013] which makes it possible to track subpixel displacements. The regularization acts as a mechanical filter on the displacement field to erase high-frequency fluctuations. The advan-

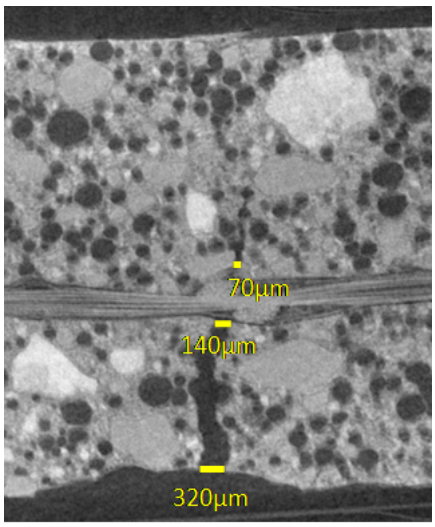

Figure 3.36: Vertical section inside the reconstructed volume of a cracked M1-We-2 sample showing the crack propagation and width in the thickness of the specimen.

tages and limitations of DIC and DVC (Digital Volume Correlation) are detailed in [Sutton, 2013].

$$f(x) = g(x + u(x)) \tag{3.3}$$

$$u(x) = \arg\min_{u} f(x) \left\| g(x + u(x)) - f(x) \right\|_{ROI}^{2} \tag{3.4}$$

DIC results of a M1-L-2 sample are shown in figures 3.37 and 3.38. It is noticed in figure 3.37 the vertical displacement field showing the deformed stage of the beam in bending. This verifies that the inclination added to the bending tests does not affect the displacement of the beam.

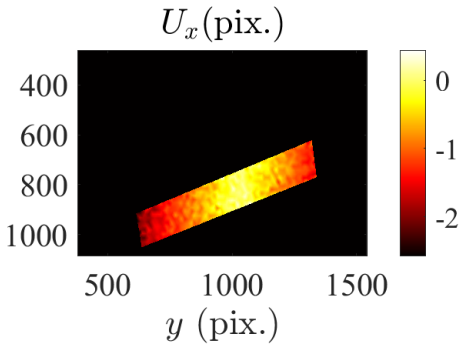

Figure 3.37: Vertical displacement fields U_x obtained by DIC.

Figure 3.38 shows the horizontal displacement U_y at three different stages of the test. At the very beginning of the test when the specimen is slightly deformed and uncracked in figure 3.38a, the horizontal displacement is homogeneous and corresponds to very small rigid body displacements as well as noise. Figure 3.38b show the horizontal displacement when the

displacement discontinuity representing the crack is first obtained. However, it is not clear whether the crack is initiated on the lower tensile surface or elsewhere. Few images later at the end of the test, the displacement discontinuity is obvious in figure 3.38c confirming the presence of the crack.

It seems difficult using this technique to be able to detect the initiation location of the crack, and that for several reasons. First, the radiographs acquisition frequency is around 2 images/s. Given the fragile behavior of the mortar, the crack initiation and propagation is instantaneous making the image acquisition frequency not sufficient to detect the moment of initiation of the crack. Second, the 2D information obtained in the radiograph is a mean value of the gray level in the width of the specimen (on the propagation path of the X-ray), thus containing 3D information. When a crack is first initiated, the gray level variation related to the appearance of the crack is lost in the mean value of the gray level. The crack should be transversely traversing and perfectly aligned with the path of the X-ray in order to induce a detectable gray level variation. Further, the image resolution is around 40 µm. The crack width need to be greater than the image resolution in order to be detectable which is not the case at the beginning of the crack initiation.

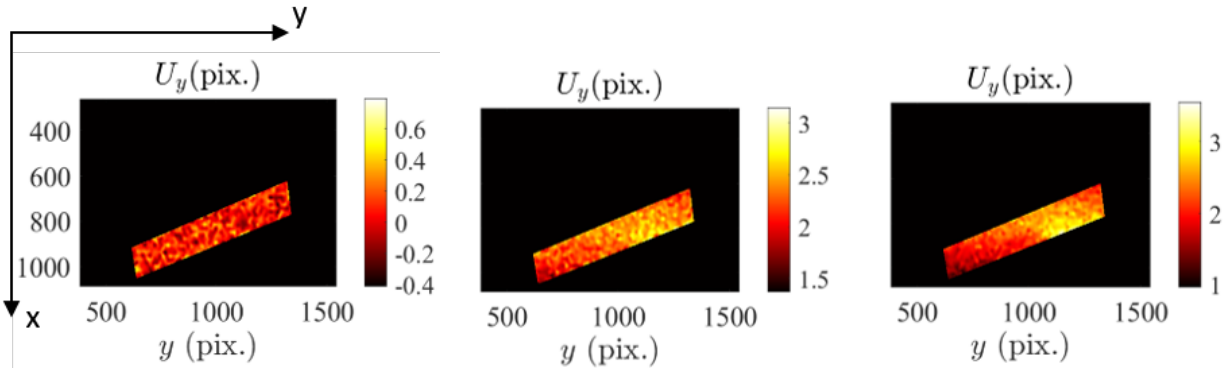

(a) Elastic slightly deformed stage (b) The first detection of the crack (c) Cracked stage

Figure 3.38: Horizontal displacement fields U_y obtained by DIC.

3.4.2.4 Comprehension elements: Analytical calculation

This analytical calculation considers the composite material as the combination of the mortar as a homogeneous material and a longitudinal reinforcement as a homogeneous material. The adhesion between the mortar and the reinforcement is considered to be perfect. Euler-Bernoulli hypothesis is considered and all materials are considered elastic. The stress profile along the cross section of the composite beam in bending is shown in figure 3.39 where:

h	is the thickness of the beam (5 mm in the case of the studied specimens)
b	is the width of the beam (12 mm in the case of the studied specimens)
c	is the cover distance
h_1	is the distance between the reinforcement (the mesh) and the neutral axix
h_2	is the distance between the neutral axis and the upper surface in compression
T_s	is the mortar's tensile strength
σ_c	is the compressive stress on the upper surface
σ_m	is the stress in the mortar in contact with the reinforcement
σ_{mesh}	is the stress in the reinforcing mesh
E_m	is the mortar's Young modulus
E_{mesh}	is fiberglass mesh Young's modulus
S_{mesh}	is the cross section of the longitudinal reinforcement

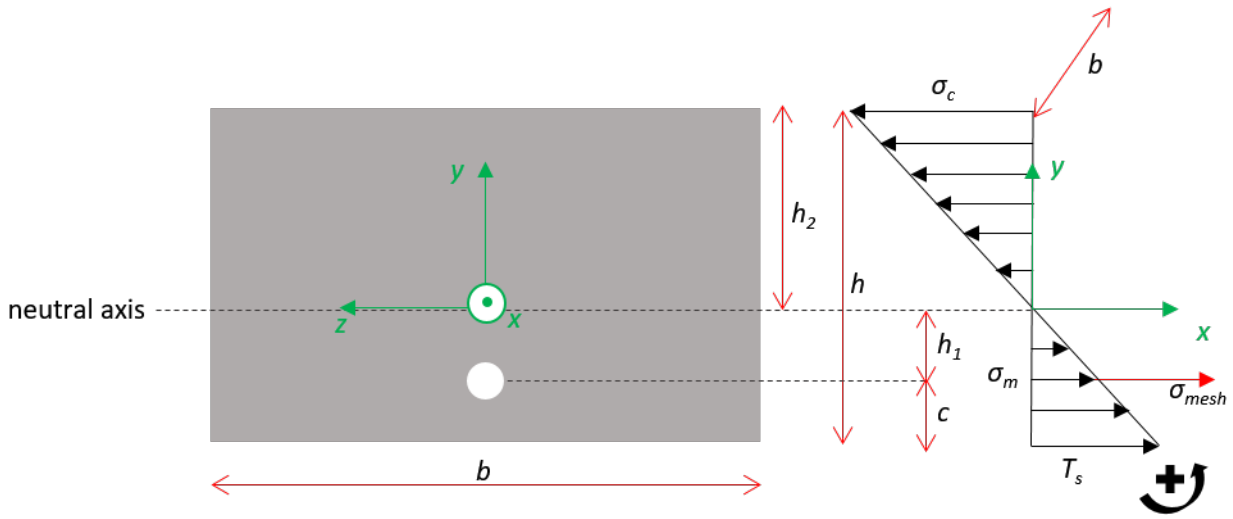

Figure 3.39: Stress profile in section of a reinforced mortar specimen in bending.

The analytical solution of the unknown variables h_1, h_2, σ_{mesh}, σ_m, σ_c and the first crack beding moment M are given in the equations below respectively:

$$h_1 = \frac{-2bcE_m h + bE_m h^2}{2(bE_m h + E_{mesh}S_{mesh})} \tag{3.5}$$

$$h_2 = \frac{bE_m h^2 - 2cE_{mesh}S_{mesh} + 2hE_{mesh}S_{mesh}}{2(bE_m h + E_{mesh}S_{mesh})} \tag{3.6}$$

$$\sigma_{mesh} = \frac{-2bcE_{mesh}T_s h + bE_{mesh}T_s h^2}{bE_m h^2 + 2cE_{mesh}S_{mesh}} \tag{3.7}$$

$$\sigma_m = \frac{T_s h_1}{c + h_1} \tag{3.8}$$

$$\sigma_c = \frac{T_s(bE_m h^2 - 2cE_{mesh}S_{mesh} + 2hE_{mesh}S_{mesh})}{bE_m h^2 + 2cE_{mesh}S_{mesh}} \tag{3.9}$$

$$M = \sigma_{mesh} S_{mesh} h_1 + T_s \frac{b}{3} + \sigma_c \frac{b}{3} \tag{3.10}$$

Figures 3.40a and 3.40b shows the plot of the first crack bending moment vs. the longitudinal reinforcement cross section (for a given cover distance) and the cover distance respectively (for a given reinforcement cross section). The first crack bending moment increases when the longitudinal yarns cross section increases hence when the mesh is thicker for a given cover distance, and it decreases when the cover distance increases hence when the mesh is placed closer to the lower tensile surface for a given reinforcement ratio.

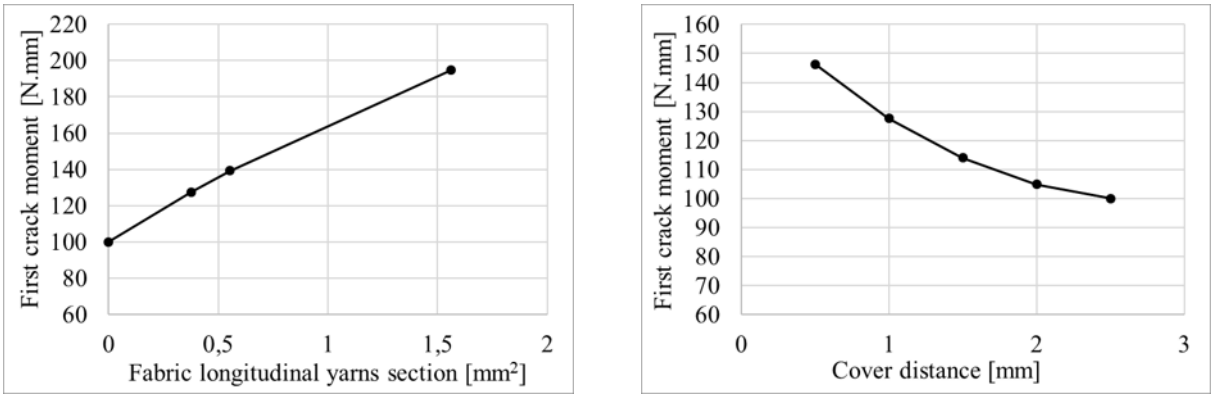

(a) For a given cover distance

(b) For a given longitudinal yarns section

Figure 3.40: First crack bending moment vs. (a) the longitudinal yarns section for a given cover distance and (b) the cover distance for a given longitudinal yarns section.

3.4.2.5 Unveiling the role of the mesh and heterogeneities with Finite Element simulations

In order to give additional elements of understanding on the effect of the transversal yarn on the stress distribution in the composite, 2D Finite Element simulations are carried out on Cast3M [Combescure et al., 1982]. A beam having the same dimensions of the tested specimens (5 mm thickness and 70 mm long) is meshed with triangular quadratic elements (TRI6). The mortar is considered to be homogeneous and reinforced with 3 node-bar elements (BAR3) representing the reinforcing longitudinal yarn. The transversal yarns are meshed with TRI6 elements as two tangent circles on both sides of the longitudinal yarn. Figure 3.41a shows the mesh of the geometry showing 3 cases where on the center the mortar is considered fully homogeneous, on the left an empty inclusion is considered representing a porosity in the mortar, and on the right a rigid inclusion meshed with TRI6 elements representing a sand grain in the mortar. The effect of the transversal yarns on the stress distribution in the mortar is studied in the presence of these inclusions and according to the cover distance (c). The latter is considered to be 2 mm representing a case where the mesh is "far" from the tensile surface and 0.5 mm representing a case where the mesh is "close" to the tensile surface. To take some hypothesis on the other side from the previous analytical, no adhesion is implemented between the mortar and longitudinal reinforcement. The longitudinal reinforcement (red line

in figure 3.41a) is linked to the transversal yarns represented with the black circles in figure 3.41a with only one point. All materials are considered elastic with corresponding properties (Young's modulus and Poisson's ratio). The simulations are carried out in plain stress and until reaching the mortar's tensile strength considered to be 2 MPa for these calculations. The Young's modulus is taken equal to 2.5 GPa for the mortar and 70 GPa for the sand grain and the fiberglass mesh.

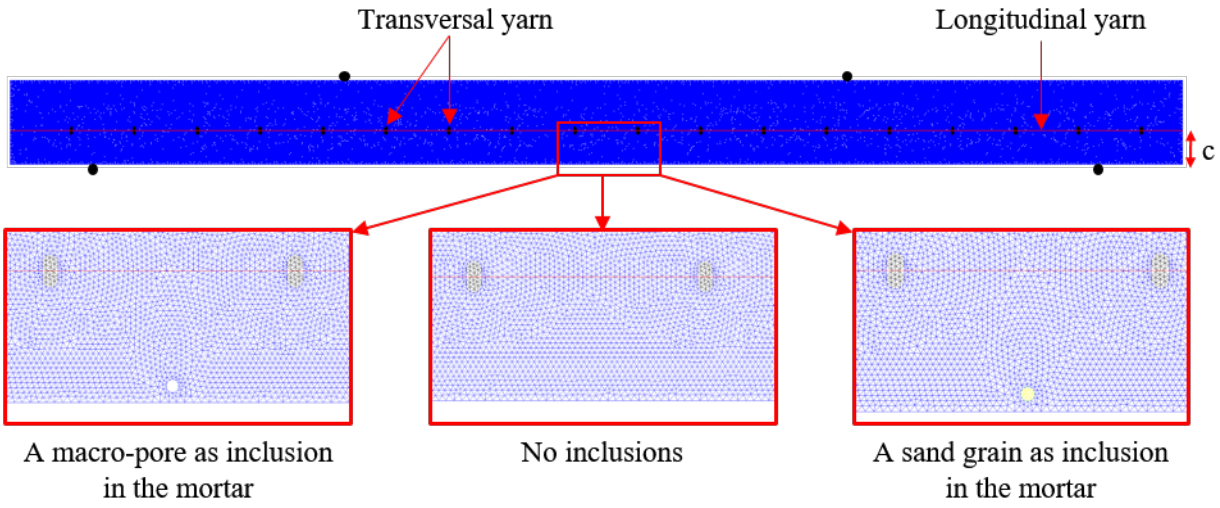

(a) Mesh of the fiberglass reinforced mortar specimen in 4-point bending

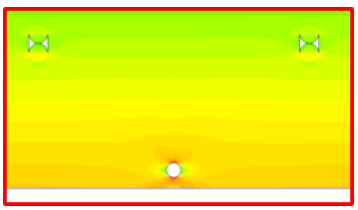

(b) $c = 2$ mm with a macro-pore

(c) $c = 2$ mm without inclusion

(d) $c = 2$ mm with a sand grain

(e) $c = 0.5$ mm with a macro-pore

(f) $c = 0.5$ mm without inclusion

(g) $c = 0.5$ mm with a sand grain

Figure 3.41: (a) Mesh of the fiberglass reinforced mortar specimen in 4-point bending; stress distribution for (b) 2 mm cover distance with a macro-pore, (c) 2 mm cover distance without inclusion, (d) 2 mm cover distance with a sand grain, (e) 0.5 cover distance with a macro-pore, (f) 0.5 mm cover distance without inclusion, and (g) 0.5 mm cover distance with a sand grain.

When the mesh is "far" from the lower tensile surface at a 2 mm distance, stress concentrations created around the transversal yarns remain still lower than the stress on the lower tensile surface, as shown in figure 3.41c. This means that the crack will initiate on lower tensile surface and propagate toward the transversal yarn. However, when an inclusion is added (a porosity in figure 3.41b or a sand grain in figure 3.41d), the higher stress concentrations are located around the inclusion that takes the lead of crack initiation. This shows the effect on only one inclusion in the mortar. Considering the total field of heterogeneities in the mortar, it is clear how the stress concentrations induced by the transversal yarns can be blurred by the surrounding heterogeneities.

On the other hand, when the mesh is "close" to the lower tensile surface at 0.5 mm, the stress concentration around the transversal yarn is the highest even when considering inclusions in the mortar as shown in figures 3.41e, 3.41f, and 3.41g. This shows that the transversal yarns have a greater potential of influencing the crack initiation and/or localization when the mesh is closer to tensile surface. Nevertheless, only one inclusion is considered in these calculations. Indeed, when considering the full field of heterogeneities in the mortar, the influence of the transversal yarn on the crack initiation and/or localization is disturbed by the surrounding stress concentrations induced by the inclusions.

These calculations have shown the complexity of the cracking mechanisms in the rendering mortar given its strongly heterogeneous character. In addition, the lower tensile surface of the mortar (or the external surface of the rendering mortar in real applications) is not smooth. The roughness of the surface created by sand grains as shown in figure 3.35a for example results in small thickness variation in the tensile zone affecting the stress distributions and the crack initiation.

3.5 Conclusion

This chapter deals with the mechanical behavior of the fiberglass mesh reinforced rendering mortar used in ETICS. The rendering mortar undergoes thermal and hygral strains, which when restrained, may lead to stresses that can attain the tensile strength of the material causing the mortar cracking. The cracking in the mortar may be initiated on two different levels: (i) on the mesoscale, where the heterogeneities of the mortar (porosity, sand particles, and the mesh) are the only source of stress concentration and/or (ii) on the structural scale, where the geometrical singularities such as window corners and thermal joints take the lead of the stress concentration and crack initiation. To understand the cracking mechanisms in the mortar and the reinforcement mechanisms of the fiberglass mesh, and to represent the two levels of cracking in the mortar, 3-point and 4-point bending tests are carried out. 4-point bending tests, on one hand, are representative of the cracking that takes place on facades without geometrical singularities where the heterogeneities of the mortar are the main crack initiators. On the other hand, 3-point bending tests are representative of the cracking that occurs on the geometrical singularities where the stress is localized. These tests are carried out in-situ X-ray tomography allowing to visualize the cracks within the 3D volume of the specimen rather than the surface of the specimen when using classical 2D imaging techniques.

The bending set-up needed to be adapted for X-ray tomography leading the newly developed inclined bending set-ups.

The 3D images of the samples revealed a material crowded with different types of heterogeneities. Each of which can have an impact on the cracking pattern. In 3-point bending tests, the theoretical cracking pattern is changed. The crack that should have appeared vertically in the middle of samples is shifted and inclined. This observation is mainly due to the competition between several phenomena: the maximal bending moment in the middle of the sample, the stress concentration induced by the heterogeneities in the mortar, the presence of the transversal yarn, and the real thickness of the mortar beneath the fiber-glass fabric caused by an uneven and coarse lower surface. Two main observations have been made. First, the porosities and the sand part particles dictate the trajectory of the crack. The crack will pass through the porosities and encounter the sand particles on its way up towards the fiber-glass mesh. Second, the fiber-glass mesh stops the propagation of the crack. The crack will not propagate through the entire thickness of the mortar, thus limiting its opening. Therefore, the fiber-glass mesh plays an important role in the durability of the ETICS by reducing the potential water leakage within the thermal insulator.

In 4-point bending, several parameters have been investigated such as the mesh properties, the transversal yarn, the direction of the mesh within the specimen, and the cover distance. The main conclusions regarding each parameter are the following:

- The thicker mesh (M2) did not provide a greater tensile strength for the composite, nor affected the number of crack induced during the test compared to the lighter fabric (M1). In addition, as opposed to M1 fabric, the transversal yarns of M2 fabric did not localize the crack despite their greater thickness. This can be explained by the larger weft distance on the case of M2 fabric leaving more room for other heterogeneities (i.e. porosity and sand grains) to influence the crack initiation.
- Despite the stress concentrations induced by the transversal yarn, the presence of the latter does not decrease the tensile strength of the composite. Further, the presence of the transversal yarn is essential to ensure the load transmission between the matrix and the mesh through its anchorage effect. The transversal yarns induce the multi-cracking in mortar, thus decreasing the crack widths.
- The direction of the mesh within the specimen (the weft yarn in the longitudinal direction, the warp yarn in the longitudinal direction, or the mesh rotated at 45°) did not affect the tensile strength of the composite. However, after the first crack, the mesh at 45° did not provide any post-cracking stiffness resulting from the weak resistance of the mesh regarding a shear loading.
- The cover distance is an important factor to consider. It has been shown that the closer the mesh to the lower tensile surface, the greater the tensile strength of the composite and the greater the number of cracks obtained. Thus, to ensure a greater resistance for the composite and a stronger multi-cracking behavior (meaning smaller crack widths), the mesh must be placed as closer as possible to the external surface in real life applications.

DIC method has been deployed on the radiographs collected during the load in order to investigate whether it is possible to determine the initiation location of the crack in the purpose of giving more information about the cracking mechanisms in the mortar. Using this technique, it was not possible to detect the initiation of the crack given the fragile behavior of the mortar. For this specific purpose, DIC showed some limitations such as the acquisition frequency of the radiographs and the image resolution compared the crack width when first initiated.

Chapter 4

Conclusion

In this work, the fiberglass mesh reinforced rendering mortar has been studied. It is used as a protection layer for ETICS which is recommended, particularly in refurbishment, to decrease the energy demand of buildings thus increasing the thermal comfort of the residents, reducing their energy bills, decreasing the energy dependency, and reducing the greenhouse gas emissions.

Studying the mechanical behavior of the fiberglass mesh reinforced rendering mortar is significant because defects such as cracking impair the performance of the reinforced mortar with also nefast consequences for the ETICS. Being a cementitious material, the mortar is in constant hygral and thermal exchange with the surrounding environment in addition to its chemical evolution due to the hydration reaction. These complex hygro-thermal loading lead to strains in the mortar which, when restrained, lead to stress that may attain the tensile strength of the material causing the mortar cracking. The glass fiber mesh is thus proposed as a solution to control cracking. The cracking in the rendering mortar may occur on two scales. On one hand, on the structural scale where window corners, thermal joints, and wall corners act as geometrical singularities that concentrate stress and eventually initiate cracks. On the other hand, in the plain zones, the heterogeneities in the mortar, including the fiberglass mesh, can act as stress concentration elements, taking the lead for crack initiation and/or localization.

The behavior of the composite material is strongly dependent on the behavior of each of its components (i.e. the mortar and the fiberglass mesh) in addition to the mortar/mesh interface qualities. In this work, the behavior of the non-reinforced rendering mortar has been investigated and has been the subject of chapter 2. In addition, cracking mechanisms of the fiberglass mesh reinforced mortar as well as the reinforcement mechanisms of the fiberglass mesh with regard to cracking within the mortar have been studied in 3.

4.1 Main conclusions

Chapter 2 investigated the early-age hygro-chemical behavior as well as the mechanical behavior of the rendering mortar. The early-age characterization showed a significant influence of the mixing protocol on the early-age response regarding weight loss and shrinkage strains.

These results suggest that ensuring an adequate reproducible and repeatable [1] mixing protocol with minimum human intervention is critical to limit the scatter and material response variability. The early-age characterization showed that a repeatable mixing protocol with minimum human intervention is needed to limit the scatter in the early-age measurements such as weight loss and shrinkage strains. In addition, the scale effect on the drying is highlighted placing in advance the coupling between the hydration of the material and the drying. Isothermal calorimetry showed that the hydration reaction of the rendering mortar is fast and most of the hydration reaction occurs during the first 24 hours of the life of the rendering mortar. In addition, it has been shown that drying of the rendering mortar is relatively fast (around 2 days) for a 5 mm thickness mortar.

Regarding the mechanical properties, the effect of coupling between the hydration and drying has been studied showing that the earlier the starting age of drying, the stronger the hydration/drying competition leading to weaker mechanical properties. In addition, the effect of drying on the mechanical properties of the mortar has been investigated. Drying have a positive impact on the mechanical resistance of the studied industrial rendering mortar: the stronger the drying the greater the flexural resistance of the material, explained by the presence of latex polymer particles and cellulose ethers that coalesce and form films binding the mineral grains during drying. Further, to study the reversibility of the strength gain due to drying, the effect of rehumidification has been investigated showing only a partial loss of the mortar's resistance due to the dissolution of the ether films that are not resistant to water as opposed to the polymer films. Finally, the evolution of the mechanical properties of the rendering mortar with time showed that the tensile strength of the mortar is somewhat stable between 3 days age and 90 days age probably due to the highly rapid hydration reaction of the studied rendering mortar.

The conclusions of chapter 2 suggests that, when combined, specific conditions can provide optimal mechanical properties for the mortar especially in terms of tensile strength. The mortar is to be stored in water or in autogenous conditions to prevent drying during the highly active period of the hydration reaction then allowed to dry to develop its full potential resistance. However, in a real life scenario, these conditions are unrealistic. Note that drying allow the mortar to attain greater resistance thus it is preferred.

Chapter 3 dealt with the behavior of the fiberglass mesh reinforced rendering mortar. To properly investigate the cracking mechanisms, whether in the stress concentration zones or in the plane zones, 3-point and 4-point bending tests have been carried out. 3-point bending tests, on one hand, are representative of the cracking in the stress concentration zones due to the maximum bending moment induced in the center of the specimen. On the other hand, 4-point bending tests, inducing a constant bending moment between the two upper supports, are representative of the cracking in the plane zones where no structural stress concentrations are induced. All the tests were carried out in-situ X-ray tomography allowing to monitor the evolution of the state of the specimens via (i) 2D radiographs during the loading periods allowing to obtain continuous information to be analyzed using DIC and (ii) 3D scans after each

[1] these concepts are not synonyms

crack when the loading is stopped allowing to obtain a 3D image of the sample at different stages.

The 3-point bending tests revealed the influence of the mortar heterogeneities on the crack localization and trajectory. The porosities and the sand grains dictate the trajectory of the crack. The crack will pass through the porosities and counter the sand particles on its way up towards the fiberglass mesh. A first reinforcement mechanism has been noticed, the fiberglass mesh stops the propagation of the crack which will not propagate through the entire thickness of the mortar, thus limiting its opening. Therefore, the fiberglass mesh plays an important role in the durability of the ETICS by reducing the potential water leakage towards the thermal insulator.

In 4-point bending, the influence of the mesh properties, the transversal yarn, the direction of the mesh within the specimen, and the cover distance have been studied. It has been shown that a thicker mesh does not necessarily provide a higher tensile strength for the composite, and thicker transversal yarns, when combined with a large yarn spacing, do not influence the localization of the cracks because of the heterogeneous stress fields created by the heterogeneities of the mortar. In addition, the presence of the transversal yarns has been shown to be essential to ensure the load transmission between the matrix and the mesh through its anchorage effect resulting in multi-cracking in the mortar thus in the reduction of crack widths. Further, it has been shown that cover distance plays an important role. To amplify the multi-cracking and to provide greater resistance for the composite, the mesh is recommended to be placed as close as possible to the tensile surface (external surface in ETICS) considering drying shrinkage as the main source of cracking. Finally, DIC did not allow the detection of the initiation point of the cracks.

4.2 Perspectives

Considering the mechanical behavior of the rendering mortar, the increase of its tensile strength was mainly attributed to the presence of cellulose ethers and polymer latex particles in the industrial premix. To confirm this explanation, the mechanical behavior of a normalized mortar in wet and dry conditions can be compared to that of a modified mortar with different ratios of polymer latex and/or cellulose ethers.

For the identification of the crack initiation source within the fiberglass mesh rendering mortar, experimental and numerical approaches are proposed.
To detect the crack initiation experimentally, Distributed Fiber Optic Sensors (DFOS) [Zdanowicz et al., 2022] may be used to measure strain fields locally allowing to detect locally (on the mesh when the fiber optical sensor is glued on the textile) the crack initiation as well as the potential debonding at the mortar/fabric interface. On the other hand, acoustic emissions, when small sensors distributed on the surface of the specimens as in, may be useful to a higher resolution for the detection of the crack initiation [Boniface et al., 2020]. These two devices have been recently bought by the laboratory. They could be used inside the X-ray tomograph. Numerically, the X-ray 3D images can be used (threshold and Finite element mesh as in [Tsi-

tova, 2022]) to validate a mechanical model that takes into account the heterogeneity of the material, the interfaces of the inclusions, and the cracking patterns observed experimentally. After validation, the mechanical model can be used to carry out a large number of numerical simulations (Monte Carlo) on randomly generated microstructures which take into account the PSD of sand grains and of the pores. This allows to identify numerically in a probabilistic approach the sources of crack initiation, the first crack load, and crack widths for a given force or displacement imposed after cracking.

To investigate the reinforcement mechanisms of the fiber glass mesh, an uniaxial loading has been used through 3-point and 4-point bending. However, the mortar in real life application as well as the fiberglass mesh acts bidirectionally. A bi-axial loading such as plate bending can be carried out.

Thermal strains in the mortar can also induce cracking. The thermal expansion coefficient of the insulator, which features a high thermal gradient, is around 6 times greater than that of the mortar. The risks of cracking associated to thermal strains in ETICS should be studied.

To maximize the tensile strength as well as the multi-cracking behavior of the reinforced mortar, it is recommended to place the mesh as close as possible to the external surface in ETICS considering the drying shrinkage as the main source of cracking. However, the PSD of sand grains in section 2.3.1 shows that around $22wt.\%$ of sand grains have a particle size greater than 0.63 mm. When the mesh is placed at a 1 mm cover distance, $22wt.\%$ of the sand grains have a diameter that exceeds the half of the cover distance. It can be suggested to modify the grain distribution of the premix.

To further decrease the environmental impact of construction and/or thermal insulation rennovations, eco-friendly materials can be studied to replace the glass in the fiberglass mesh reinforcement. The use of jute fiber [Zakaria et al., 2017] or flax textile [Julija, 2020] may be an eco-friendly alternative. In addition, recycled sand from concrete recycling may be used to replace the sand in the rendering mortar premix.

Appendix A

Drying model

Drying in mature cement-based materials can be accurately modeled using mass balance equations for liquid water, water vapor, and dry air. It is a very complex phenomenon, since it involves permeation, diffusion, adsorption/desorption, and condensation/evaporation [Mainguy, 1999, Mainguy et al., 2001, Thiery et al., 2007].
If porosity is assumed to be constant, gas (dry air and water vapor) permeation is neglected, and temperature is assumed to be constant, the Richard-Fick model can be used [Hilaire, 2014, Soleilhet, 2018, Ma et al., 2020, Carette et al., 2020]. Using the saturation degree S_l as a primary variable [Sleiman et al., 2020, Adia et al., 2020, Kinda et al., 2020], the main mass balance equations lead to equation A.1

$$\frac{\partial S_l}{\partial t} = \nabla(D(S_l)\nabla S_l) \tag{A.1}$$

where D is the global equivalent diffusion coefficient depending non-linearly on liquid water saturation degree (S_l). The global equivalent diffusion coefficient is given by:

$$D(S_l) = \frac{1}{1-\frac{\rho_v}{\rho_l}}\frac{\partial P_c}{\partial S_l}\left[\frac{K^{eff}(S_l)}{\phi\mu_l} + D^{eff}(S_l)\left(\frac{M_v}{\rho_l RT}\right)^2 P_{vsat}\exp\left(P_c\frac{M_v}{\rho_l RT}\right)\right] \tag{A.2}$$

with ϕ the porosity of the material, K^{eff} the effective permeability of the liquid water, D^{eff} the effective vapor water diffusion coefficient, and P_c the capillary pressure; ρ_l, ρ_v, μ_l are respectively the density of the liquid water, the density of water vapor, and the dynamic viscosity of the liquid water; T is the temperature, and R the perfect gas constant; P_{vsat} and M_v are respectively the saturating water vapor pressure and the molar mass of water. The first term in equation A.2 represents the water liquid permeation mechanism and the second term represents the water vapor diffusion.

Using the Boltzmann transform:

$$u = \frac{x^2}{Dt} \tag{A.3}$$

Equation A.1 becomes in the case of 1D diffusion and constant global equivalent diffusivity:

$$u \cdot \frac{\partial S_l}{\partial u} + 2 \cdot \frac{\partial^2 S_l}{\partial u^2} = 0 \tag{A.4}$$

Therefore, the solution depends only on the variable u. The calculation of the weight loss evolution in semi-infinite or finite media with different boundary conditions leads to the schematic evolution displayed in Figure A.1 [Crank, 1979]. Curve 1 (in red) corresponds to a semi-infinite medium with a Dirichlet-type boundary condition (i.e. S_l = cst at the boundary). The slope is proportional to the square root of the equivalent diffusivity. Thus, it gives information about the porosity (size, connectivity etc.). Besides, for a finite medium (curve 2 in blue), the evolution remains linear up to the beginning of the drying in the core. Finally, if a convective-type boundary condition is used (to take into account evaporation and/or diffusion of vapor water in the boundary layer), a S-type curve is obtained (curve 3 in green). In cement-based materials, such behavior is observed for small thickness and/or high value of equivalent diffusivity (high water to cement ratio for instance resulting in large connected pores) [Kinda et al., 2020], which is the case of rendering mortars.

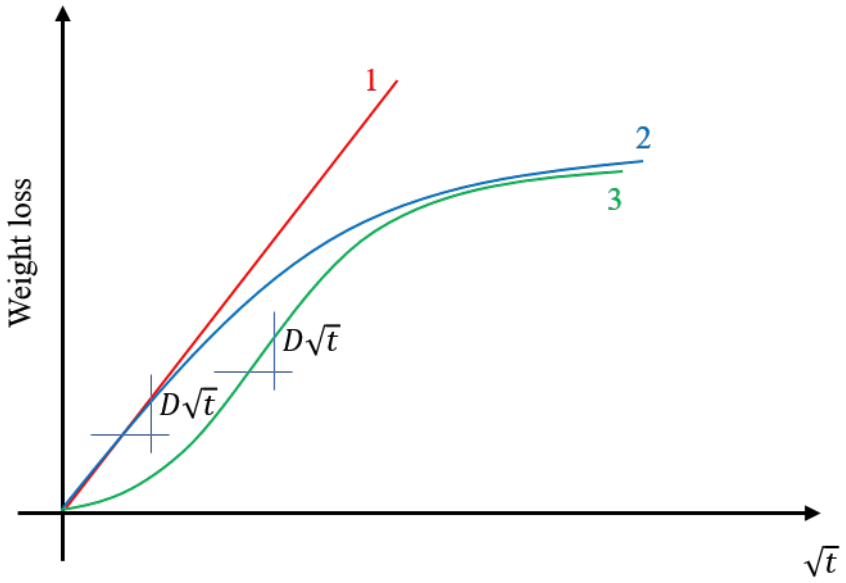

Figure A.1: Schematic evolution of weight loss vs. $\sqrt{t}$ in the case of semi-infinite or finite media

The Boltzmann transform (equation A.4) implies also that the use of an equivalent radius (R_{eq}) leads to the same weight loss evolution if plotted with respect to $\frac{\sqrt{t}}{R_{eq}}$. All these elements are being used to analyze the experimental results.

Appendix B

Stress in mortar

The risk of cracking of the mortar by drying shrinkage comes from several sources (cf. chapter 1):

- Mortar heterogeneity (differential strains between cement paste and sand grains, presence of defects such as porosity);
- Differential strains between the fiberglass mesh and the mortar;
- Differential strains between the mortar and the insulation (fixed on a bearing wall);
- Stress concentration zones (joint between insulation blocks, window corners etc.). This point will not be studied hereafter.

The elastic mechanical properties of the mortar, the fiberglass mesh, the insulator, and the wall are reported in table B.1. The volume fraction of the fiberglass mesh is considered to be 1% and the drying shrinkage strains of the mortar is taken a constant and equal to -1·10^{-3}. When the drying shrinkage strains are totally restrained, the tensile stress in the mortar (neglecting the evolution of mechanical properties of the mortar and creep strains) is given by:

$$\sigma = -\frac{E_m}{\varepsilon_{ds}} = 3MPa \tag{B.1}$$

where E_m is the mortar's Young's modulus and ε_{ds} is the drying shrinkage strains in the mortar.

Table B.1: Properties of ETICS elements

	Wall	**Insulator**	**Mortar**	**Fiberglass mesh**
Young's modulus E [GPa]	20	3×10^{-3}	3	70
Poisson's Ratio ν	0.2	0.4	0.2	0.2

It is noticed that the stresses are greater than the tensile strength of the rendering mortar. It should be noted that the carried out bending tests give a value of equivalent bending tensile strength. The uniaxial tensile strength is lower than the measured value.

B.1 Heterogeneous mortar

Finite Element simulations considering a heterogeneous mortar in the ETICS system have been carried out on Cast3M. The mortar undergoes either a thermal or a hygral loading. The mesh of the ETICS is shown in figure B.1.

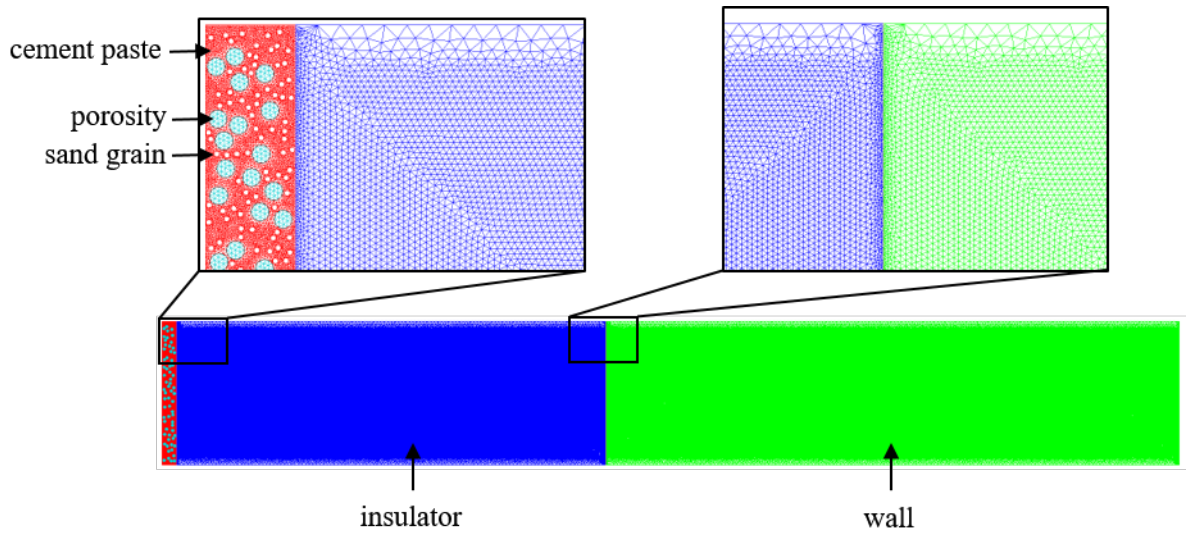

Figure B.1: The of the ETICS considering a heterogeneous mortar

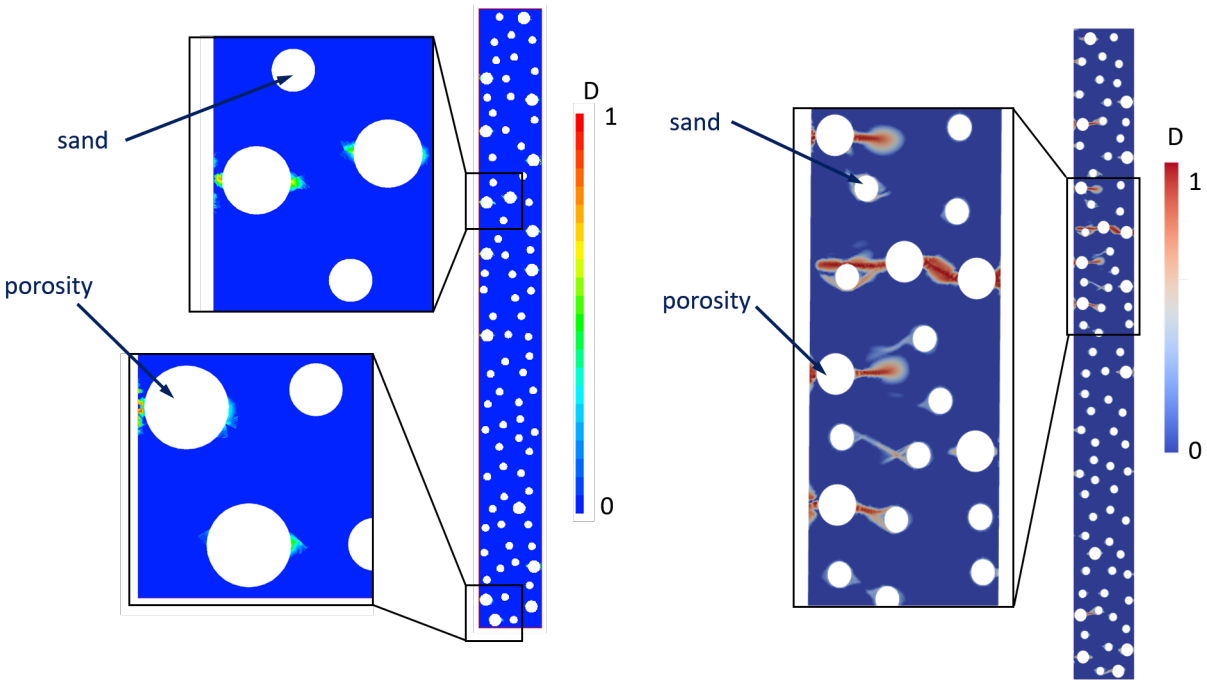

(a) Thermal loading

(b) Hygral loading

Figure B.2: (a) Stress profile σ_{yy} within the thickness of the mortar. (b) Displacement U_y with respect to the vertical axis y.

The thermal loading is induced by a temperature change. The initial temperature of all the system is considered to be 20°C. The external temperature imposed at the external surface of the mortar is then considered to be -25°C. On the other hand, the hygral loading is drying of the mortar from an initial imposed relatibe humidity at 99% to a relative humidity of 50%. For both thermal and hygral loading, the Mazars damage model [Mazars, 1984] is used. The damage field D is shown in figure B.2a in the case of the thermal load, and in figure B.2b in the case of the hygral load. Is is notice that the damage field is mainly induced by the inclusions (pores and sand grains) proving the effect of the heterogeneities on the crack initiation by inducing stress concentrations. In addition the hyfral loading induces more damage than the thermal loading.

B.2 Differential strains between the mortar and the thermal insulator

The simulations are carried out using the CAST3M finite element code. The studied system and the associated mesh are represented in figure B.3. It is composed of the rendering mortar, an insulator (here expanded polystyrene), taking into account connection to the load-bearing wall using an adhesive considered to be the rendering mortar.

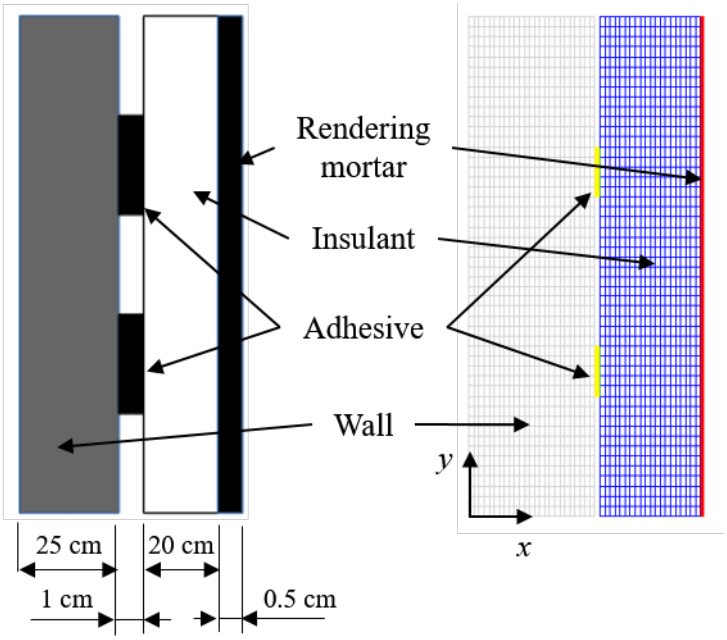

Figure B.3: The studied system and the mesh

Different scenarios are considered in the numerical simulations. The influence of the insulation-wall connection on the stresses generated in the mortar is considered. The fiberglass mesh as well as the evolution of mechanical properties during hydration are not taken into account. The behavior of each material is assumed to be elastic. Figure B.5 groups the different cases, where the mesh, the deformation and the maximum principal stress are reported:

- Case 1 (figure B.4a) assumes a bond between the load-bearing wall and the insulation using the rendering mortar as adhesive. The maximum principal stress σ_{Pmax} is around 0.12 MPa, which is significantly lower than the tensile strength of the mortar.
- The increase in bonding length in case 2 (figure B.4b) leads to a slight increase in stress.
- Assuming a perfect connection between the insulation and the load-bearing wall in case 3 (figure B.4c), the maximum principal stress reaches a value of 0.21 MPa. It is still significantly lower than the tensile strength of the mortar.
- In the case 4 (figure B.4d), where it is assumed that there is no adhesion between the insulation and the load bearing wall, the maximum principal stress becomes of the same order of magnitude as in the case 1 where the insulation is bonded to the interior wall. The deformation is different in this case being similar to a bending deformation.

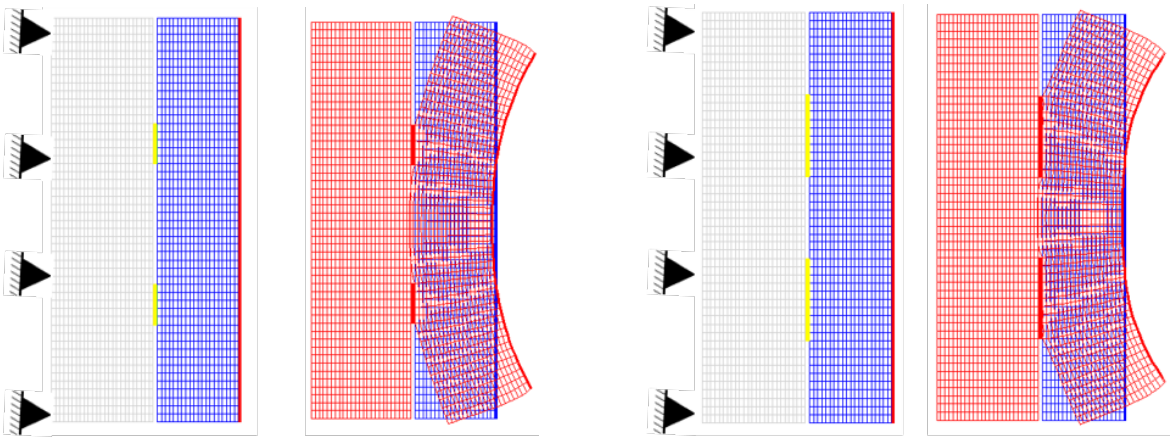

(a) Case 1 : $\sigma_{Pmax} = 0.12$ MPa

(b) Case 2 : $\sigma_{Pmax} = 0.14$ MPa

(c) Case 3 : $\sigma_{Pmax} = 0.21$ MPa

(d) Case 4 : $\sigma_{Pmax} = 0.14$ MPa

Figure B.4: The deformation and the stress in the mortar in the 4 different cases considered.

The stress profile in the central zone of the mortar shows that the stresses σ_{yy} are linear in the thickness of the mortar (B.5a), which corresponds to a linear deformation (elastic

behavior), an assumption made in the case of the Euler-Bernoulli theory. However, the stress profile is not symmetrical which is representative of a compound bending stress. On the other hand, the horizontal displacement U_x is plotted in the figure B.5b along the vertical axis. A parabolic interpolation leads to a linear regression coefficient R^2 very close to 1, which is characteristic of a 4-point bending test.

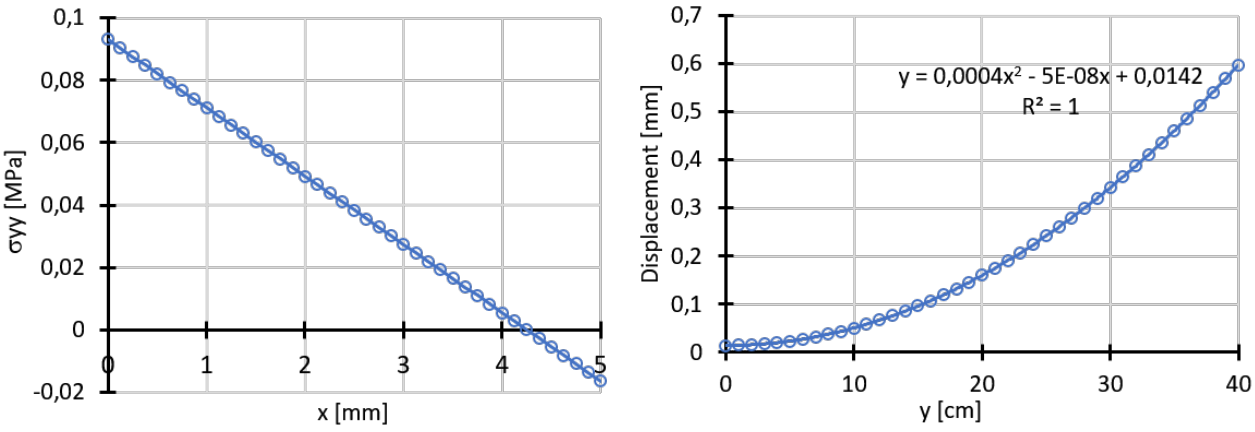

(a) (b)

Figure B.5: (a) Stress profile σ_{yy} within the thickness of the mortar. (b) Displacement U_y with respect to the vertical axis y.

B.3 Differential strains between the rendering mortar and the fiberglass mesh

All materials are assumed to have isotropic linear elastic behavior. A parallel model is considered as shown in figure B.6. In the case where only incompatibilities are studied, we obtain the equilibrium equation below:

$$\sigma = f_{mesh}\sigma_{mesh} + f_m\sigma_m \tag{B.2}$$

where f_{mesh} is the volume fraction of the fiberglass mesh, f_m is the volume fraction of the mortar, σ_{mesh} is the stress in the fiberglass mesh, and σ_m is the stress in the mortar.
Using the behavioral laws, we obtain the expression of the stress developed in the mortar σ_m in equation B.3 and the fiberglass mesh σ_{mesh} in equation B.4:

$$\sigma_m = -\frac{E_m \cdot E_{mesh}}{E} \cdot \varepsilon_{ds} = 0.6MPa \tag{B.3}$$

$$\sigma_{mesh} = \frac{E_{mesh} \cdot E_m}{E} \cdot \varepsilon_{ds} = -57MPa \tag{B.4}$$

where E_mesh, E_m, and E are the Young's modulus of, respectively, the fiberglass mesh, the mortar, and the composite fiberglass reinforced mesh (calculated with the parallel model).

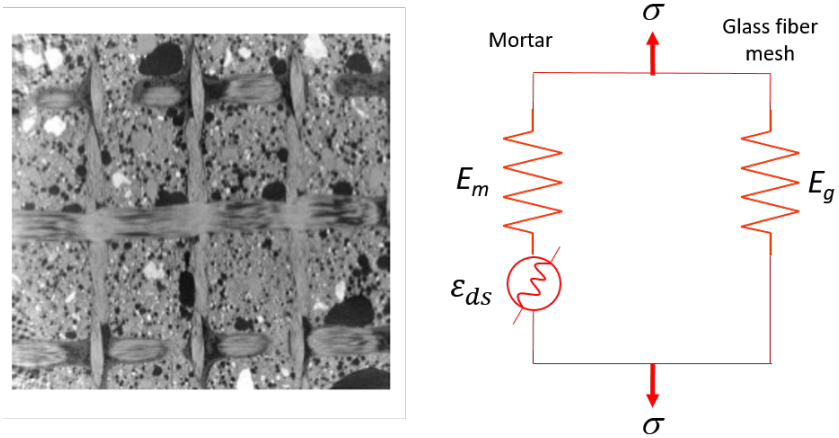

Figure B.6: Parallel model: rendering mortar and the fiberglass mesh

It is observed that the mortar is in tension, the stress value remains lower than the tensile strength of the mortar, but it is significant compared to the values obtained previously in the Finite Element calculations taking into account the geometry of the wall. The fiberglass mesh is in compression.

Appendix C

Crack prediction in Eurocode 2, Model Code MC2010, and ACI code

C.1 Eurocode 2

To calculate a predicted crack width, the crack spacing must first be calculated. The crack spacing is defined as the distance between two adjacent cracks. In the Eurocode 2 [EN, 1992], the maximum crack spacing $S_{r,max}$ is given by:

$$S_{r,max} = k_3 c + k_1 k_2 k_4 \Phi / \rho_{p,eff} \tag{C.1}$$

where:

- Φ is the bar diameter or the equivalent bar diameter,
- c is the cover to the longitudinal reinforcement,
- k_1 is a coefficient that takes into account the bond properties of the reinforcement,
- k_2 is a coefficient that takes into account the distribution of strain, and
- k_3 and k_4 are coefficients that may be selected by the country.

Crack width w_k is thus calculated by:

$$w_k = S_{r,max}(\varepsilon_{sm} - \varepsilon_{cm}) \tag{C.2}$$

where:

- ε_{sm} is the mean strain in the reinforcement, and
- ε_{cm} is the mean strain in the concrete between cracks.

C.2 MC2010

In the Model Code MC2010 [Taerwe et al., 2013] the crack width is calculated as follows:

$$w_d = \beta_w \cdot k_{1/r} \cdot s_m(\varepsilon_{sm} - \varepsilon_{cm} - \eta_r \varepsilon_{cs}) \tag{C.3}$$

where:

- β_w is a factor to convert the mean crack width to the maximum crack width (According to [Caldentey et al., 2019], it can be taken equal to 1.7),
- $k_{1/r}$ is a factor to take in account the curvature of the concrete element,
- s_m is the mean crack spacing of the element,
- ε_{sm} is the average steel strain over the length s_m, and
- ε_{cm} is the average concrete strain over the length s_m.

The mean crack spacing is thus taken equal to:

$$s_m = k_c \cdot c + k_{\Phi/\rho} \cdot k_{fl} \cdot k_b \cdot \frac{f_{ctm}}{\tau_{bms}} \cdot \frac{\phi_s}{\rho_{s,ef}} \tag{C.4}$$

where:

- k_c is an empirical parameter to take account of the concrete cover (It can be taken equal to 1.5),
- c is the maximum concrete cover.,
- $k_{\phi/\rho}$ is an empirical parameter to take account of the bond (It can be taken equal to 0.25),
- k_b is a parameter that takes account of the casting position,
- f_{ctm} is the mean tensile strength of concrete,
- τ_{bms} is a structural parameter (the newest version of the Eurocode suggests taking it equal to 7.2),
- ϕ_s is the steel reinforcements diameter, and
- $\rho_{s,ef}$ is the reinforcement ratio corresponding to the tensile face under consideration of the effective section.

C.3 ACI code

The crack width model illustrates crack spacing and width as funtions of the transversal reinforcement spacing. Thus, cracking can be controlled by limiting the transversal reinforcement spacing and maximum bar spacings can be determined by limiting the crack widths to acceptable limits [Frosch, 1999]. The maximum crack width is thus calculated by:

$$w_c = 2 \cdot \frac{f_s}{E_s} \cdot \beta \sqrt{d_c^2 + (\frac{s}{2})^2} \tag{C.5}$$

where:

- s is the maximum permissible bar spacing [in],
- w_c is the limiting crack width [in],
- $E_s = 29000$ ksi,
- $f_s = 1.0 + 0.08 d_c$, and
- d_c is the bottom cover measured from center of lowest bar [in].

Bibliography

[Acker, 1988] Acker, P. (1988). *Comportement mécanique du béton: apports de l'approche physico-chimique*. Number 152.

[Acker, 1991] Acker, P. (1991). Retraits et fissurations du béton: causes, mécanismes, modèles.

[Adia et al., 2020] Adia, J.-L. D., Koala, H., Kinda, J., Sanahuja, J., and Charpin, L. (2020). Concrete drying modelling in a variable temperature environment. In *RILEM Spring Convention and Conference*, pages 47–58. Springer.

[Amaro et al., 2013] Amaro, B., Saraiva, D., de Brito, J., and Flores-Colen, I. (2013). Inspection and diagnosis system of etics on walls. *Construction and Building Materials*, 47:1257–1267.

[AQC, 2019] AQC (2019). Enveloppes et revêtements extérieurs : Rénovation de systèmes d'isolation thermique par l'extérieur (etics) existants. Technical Report D.09, Agence Qualité Construction.

[Bader, 1997] Bader, M. (1997). An introduction to composite materials.

[Balayssac et al., 2011] Balayssac, J., Nicot, P., Ruot, B., Devès, O., and Détriché, C. (2011). Influence of admixtures on the cracking sensitivity of mortar layers applied to a mineral substrate. *Construction and Building Materials*, 25(6):2828–2836.

[Baquerizo et al., 2016] Baquerizo, L. G., Matschei, T., and Scrivener, K. L. (2016). Impact of water activity on the stability of ettringite. *Cement and Concrete Research*, 79:31–44.

[Baquerizo et al., 2015] Baquerizo, L. G., Matschei, T., Scrivener, K. L., Saeidpour, M., and Wadsö, L. (2015). Hydration states of afm cement phases. *Cement and Concrete Research*, 73:143–157.

[Barhum and Mechtcherine, 2013] Barhum, R. and Mechtcherine, V. (2013). Influence of short dispersed and short integral glass fibres on the mechanical behaviour of textile-reinforced concrete. *Materials and structures*, 46(4):557–572.

[Barluenga and Hernandez-Olivares, 2004] Barluenga, G. and Hernandez-Olivares, F. (2004). Sbr latex modified mortar rheology and mechanical behaviour. *Cement and Concrete Research*, 34(3):527–535.

[Baroghel-Bouny, 1994] Baroghel-Bouny, V. (1994). Caractérisation des pâtes de ciment et des bétons-méthodes, analyse, interprétations.

[Baron, 1982] Baron, J. (1982). *Le béton hydraulique : connaissance et pratique*. Presses de l'Ecole nationale des ponts et chaussées.

[Barreira and de Freitas, 2015] Barreira, E. and de Freitas, V. P. (2015). *External Thermal Insulation Composite Systems (ETICS): An Evaluation of Hydrothermal Behavior*. Springer. 71 pages.

[Bazant and Wittmann, 1982] Bazant, Z. P. and Wittmann, F. H. (1982). Creep and shrinkage in concrete structures.

[Benboudjema, 2002] Benboudjema, F. (2002). *Modélisation des déformations différées du béton sous sollicitations biaxiales. Application aux enceintes de confinement de bâtiments réacteurs des centrales nucléaires*. PhD thesis, Université de Marne la Vallée.

[Benboudjema et al., 2005] Benboudjema, F., Meftah, F., and Torrenti, J.-M. (2005). Interaction between drying, shrinkage, creep and cracking phenomena in concrete. *Engineering structures*, 27(2):239–250.

[Bentur, 2000] Bentur, A. (2000). Role of interfaces in controlling durability of fiber-reinforced cements. *Journal of materials in civil engineering*, 12(1):2–7.

[Bentz et al., 1994] Bentz, D., Martys, N. S., Stutzman, P., Levenson, M., Garboczi, E., Dunsmuir, J., and Schwartz, L. (1994). X-ray microtomography of an astm c109 mortar exposed to sulfate attack. *MRS Online Proceedings Library*, 370(1):77–82.

[Bentz, 1997] Bentz, D. P. (1997). Three-dimensional computer simulation of portland cement hydration and microstructure development. *J. Am. Ceram. Soc.*, 80(1):3–21.

[Bentz et al., 2000] Bentz, D. P., Quenard, D., Kunzel, H. M., Baruchel, J., Peyrin, F., Martys, N. S., and Garboczi, E. (2000). Microstructure and transport properties of porous building materials. ii: Three-dimensional x-ray tomographic studies. *Materials and Structures*, 33(3):147–153.

[Bernachy-Barbe et al., 2020] Bernachy-Barbe, F., Sayari, T., Dewynter-Marty, V., and l'Hostis, V. (2020). Using x-ray microtomography to study the initiation of chloride-induced reinforcement corrosion in cracked concrete. *Construction and Building Materials*, 259:119574.

[Berthereau and Dallies, 2008] Berthereau, A. and Dallies, E. (2008). Fibres de verre de renforcement.

[Betioli et al., 2009] Betioli, A., Gleize, P., Silva, D., John, V., and Pileggi, R. (2009). Effect of hmec on the consolidation of cement pastes: isothermal calorimetry versus oscillatory rheometry. *Cement and concrete Research*, 39(5):440–445.

[Bisschop et al., 2001] Bisschop, J., Pel, L., and Van Mier, J. (2001). Effect of aggregate size and paste volume on drying shrinkage microcracking in cement-based composites. *Creep, shrinkage and durability mechanics of concrete and other quasi-brittle materials*, pages 75–80.

[Bolte and Cordelières, 2006] Bolte, S. and Cordelières, F. P. (2006). A guided tour into subcellular colocalization analysis in light microscopy. *Journal of microscopy*, 224(3):213–232.

[Bompadre and Donnini, 2021] Bompadre, F. and Donnini, J. (2021). Surface modification of glass textile for the reinforcement of a cement-based composite: A review. *Applied Sciences*, 11(5):2028.

[Boniface et al., 2020] Boniface, A., Saliba, J., Sbartaï, Z. M., Ranaivomanana, N., and Balayssac, J.-P. (2020). Evaluation of the acoustic emission 3d localisation accuracy for the mechanical damage monitoring in concrete. *Engineering Fracture Mechanics*, 223:106742.

[Boughriet, 2018] Boughriet, R. (2018). Isolation thermique par l'extérieur : une opportunité de travaux à ne pas négliger. last accessed 18/04/2022.

[Bouterf, 2014] Bouterf, A. (2014). *Comportement mécanique de la plaque de plâtre étudié par tomographie et essais mécaniques in-situ*. PhD thesis, École normale supérieure de Cachan-ENS Cachan.

[Brisard et al., 2020] Brisard, S., Serdar, M., and Monteiro, P. J. (2020). Multiscale x-ray tomography of cementitious materials: A review. *Cement and Concrete Research*, 128:105824.

[Brooks and Neville, 1977] Brooks, J. and Neville, A. (1977). A comparison of creep, elasticity and strength of concrete in tension and in compression. *Magazine of Concrete research*, 29(100):131–141.

[Bucher et al., 2017] Bucher, R., Vidal, T., Sellier, A., and Verdier, J. (2017). Effet du séchage sur les propriétés mécaniques des matériaux cimentaires. In *CFM 2017-23ème Congrès Français de Mécanique*. AFM, Maison de la Mécanique, 39/41 rue Louis Blanc-92400 Courbevoie.

[Bureau et al., 2001] Bureau, L., Alliche, A., Pilvin, P., and Pascal, S. (2001). Mechanical characterization of a styrene–butadiene modified mortar. *Materials Science and Engineering: A*, 308(1-2):233–240.

[Burlion et al., 2006] Burlion, N., Bernard, D., and Chen, D. (2006). X-ray microtomography: application to microstructure analysis of a cementitious material during leaching process. *Cement and Concrete Research*, 36(2):346–357.

[Burlion et al., 2005] Burlion, N., Bourgeois, F., and Shao, J.-F. (2005). Effects of desiccation on mechanical behaviour of concrete. *Cement and concrete composites*, 27(3):367–379.

[Butcher, 1958] Butcher, W. (1958). The effect of air drying before test: 28-day strength of concrete. *Constructional Rev*, pages 31–32.

[Butler et al., 2010] Butler, M., Mechtcherine, V., and Hempel, S. (2010). Durability of textile reinforced concrete made with ar glass fibre: effect of the matrix composition. *Materials and structures*, 43(10):1351–1368.

[Büttner et al., 2008] Büttner, T., Keil, A., and Raupach, M. (2008). Improvement of the load-bearing capacity and durability of textile-reinforced concrete due to the use of polymers. In *15th Congress of the Glassfibre Reinforced Concrete Association International, Prague, Czech Republic*, pages 20–23.

[Caldentey et al., 2019] Caldentey, A. P., García, R., Gribniak, V., and Rimkus, A. (2019). Tension vs. flexure: Reasons to modify the formulation of mc 2010 for cracking.

[Carette et al., 2020] Carette, J., Soleilhet, F., Benboudjema, F., Ma, X., Nahas, G., Abahri, K., Darquennes, A., and Bennacer, R. (2020). Identifying the mechanisms of concrete drying: An experimental-numerical approach. *Construction and Building Materials*, 230:117001.

[Chan, 2021] Chan, N. (2021). *Étude de la variabilité expérimentale et modélisation discrète du comportement des matériaux cimentaires : effet combiné du séchage et d'un chargement mécanique*. Theses, Université Paris-Saclay.

[Chandra and Ohama, 1994] Chandra, S. and Ohama, Y. (1994). *Polymers in concrete*. CRC press.

[Charmeau et al., 1999] Charmeau, J.-Y., Gerin, P. A., Vovelle, L., Schirrer, R., and Holl, Y. (1999). Adhesion of latex films. part iii. surfactant effects at various peel rates. *Journal of adhesion science and technology*, 13(2):203–215.

[Chen, 2017] Chen, Y. (2017). *Damage mechanisms in SiC/SiC composite tubes: three-dimensional analysis coupling tomography imaging and numerical simulation*. PhD thesis, Universite de Paris-Est.

[Chilwesa et al., 2019] Chilwesa, M., Facconi, L., Minelli, F., Reggia, A., and Plizzari, G. (2019). Shrinkage induced edge curling and debonding in slab elements reinforced with bonded overlays: Influence of fibers and sra. *Cement and Concrete Composites*, 102:105–115.

[Cohen and Peled, 2012] Cohen, Z. and Peled, A. (2012). Effect of nanofillers and production methods to control the interfacial characteristics of glass bundles in textile fabric cement-based composites. *Composites Part A: Applied Science and Manufacturing*, 43(6):962–972.

[Colombo et al., 2013] Colombo, I. G., Magri, A., Zani, G., Colombo, M., and Di Prisco, M. (2013). Erratum to: Textile reinforced concrete: experimental investigation on design parameters. *Materials and structures*, 46(11):1953–1971.

[Combescure et al., 1982] Combescure, A., Hoffmann, A., and Pasquet, P. (1982). The castem finite element system. In *Finite Element Systems*, pages 115–125. Springer.

[Contamine et al., 2011] Contamine, R., Larbi, A. S., and Hamelin, P. (2011). Contribution to direct tensile testing of textile reinforced concrete (trc) composites. *Materials Science and Engineering: A*, 528(29-30):8589–8598.

[Coussot, 2005] Coussot, P. (2005). Rheometry of pastes, suspensions, and granular materials: applications in industry and environment.

[Crank, 1979] Crank, J. (1979). *The mathematics of diffusion*. Oxford university press.

[da Silva and Lordsleem Jr, 2021] da Silva, J. L. and Lordsleem Jr, A. C. (2021). Influence of mixer type and mixing time on the multipurpose mortars properties. *Case Studies in Construction Materials*, 15:e00562.

[De França et al., 2019] De França, M. S., Cazacliu, B., Cardoso, F. A., and Pileggi, R. G. (2019). Influence of mixing process on mortars rheological behavior through rotational rheometry. *Construction and Building Materials*, 223:81–90.

[De Sa, 2007] De Sa, C. (2007). *Etude hydro-mécanique et thermo-mécanique du béton. Influence des gradients et des incompatibilités de déformation*. PhD thesis, École normale supérieure de Cachan-ENS Cachan.

[Dong et al., 2020] Dong, Z., Deng, M., Zhang, C., Zhang, Y., and Sun, H. (2020). Tensile behavior of glass textile reinforced mortar (trm) added with short pva fibers. *Construction and Building Materials*, 260:119897.

[Donnini et al., 2017] Donnini, J., y Basalo, F. D. C., Corinaldesi, V., Lancioni, G., and Nanni, A. (2017). Fabric-reinforced cementitious matrix behavior at high-temperature: Experimental and numerical results. *Composites Part B: Engineering*, 108:108–121.

[EAE, 2021] EAE (2021). European association for external thermal insulation composite systems: Benefits for the environment, the economy and the people. last accessed 18/04/2022.

[Eloukabi et al., 2013] Eloukabi, H., Sghaier, N., Nasrallah, S. B., and Prat, M. (2013). Experimental study of the effect of sodium chloride on drying of porous media: The crusty–patchy efflorescence transition. *International Journal of Heat and Mass Transfer*, 56(1-2):80–93.

[EN, 1992] EN, B. (1992). 1-1: 2004: Eurocode 2: Design of concrete structures-part 1-1: General rules and rules for buildings. *British Standards Institution, London*.

[EOTA, 2013] EOTA (2013). Etag 004: Guideline for european technical approval of external thermal insulation composite systems with rendering.

[Flatt et al., 2011] Flatt, R. J., Scherer, G. W., and Bullard, J. W. (2011). Why alite stops hydrating below 80% relative humidity. *Cement and Concrete Research*, 41(9):987–992.

[Folic and Radonjanin, 1998] Folic, R. J. and Radonjanin, V. S. (1998). Experimental research on polymer modified concrete. *Materials Journal*, 95(4):463–469.

[Frosch, 1999] Frosch, R. J. (1999). Another look at cracking and crack control in reinforced concrete. *Structural Journal*, 96(3):437–442.

[Galimshina et al., 2021] Galimshina, A., Moustapha, M., Hollberg, A., Padey, P., Lasvaux, S., Sudret, B., and Habert, G. (2021). What is the optimal robust environmental and cost-effective solution for building renovation? not the usual one. *Energy and Buildings*, 251:111329.

[Gao et al., 2004] Gao, S., Mäder, E., and Plonka, R. (2004). Coatings for glass fibers in a cementitious matrix. *Acta Materialia*, 52(16):4745–4755.

[Garboczi and Bullard, 2004] Garboczi, E. J. and Bullard, J. W. (2004). Shape analysis of a reference cement. *Cement and concrete research*, 34(10):1933–1937.

[Genovés et al., 2017] Genovés, V., Gosálbez, J., Carrión, A., Miralles, R., and Payá, J. (2017). Ultrasonic broadband signals monitoring of glass-fiber reinforced cement (grc) bending tests. *Cement and Concrete Composites*, 80:55–63.

[Gerin et al., 1999] Gerin, P. A., Grohens, Y., Schirrer, R., and Holl, Y. (1999). Adhesion of latex films. part iv. dominating interfacial effect of the surfactant. *Journal of adhesion science and technology*, 13(2):217–236.

[Gopinath et al., 2018] Gopinath, S., Gettu, R., and Iyer, N. R. (2018). Influence of prestressing the textile on the tensile behaviour of textile reinforced concrete. *Materials and Structures*, 51(3):1–12.

[Goto, 2006] Goto, T. (2006). *Influence des paramètres moléculaires du latex sur l'hydratation, la rhéologie et les propriétés mécaniques des composites ciment/latex*. PhD thesis, Université Pierre et Marie Curie-Paris VI.

[Hansen, 1986] Hansen, T. C. (1986). Physical structure of hardened cement paste. a classical approach. *Materials and Structures*, 19(6):423–436.

[Hanson, 1968] Hanson, J. (1968). Effects of curing and drying enviroments on splitting tensile strength of concrete. In *Journal Proceedings*, volume 65, pages 535–543.

[He et al., 2010] He, H., Guo, Z., Stroeven, P., Stroeven, M., and Sluys, L. J. (2010). Strategy on simulation of arbitrary-shaped cement grains in concrete. *Image Analysis & Stereology*, 29(2):79–84.

[Hearn, 1999] Hearn, N. (1999). Effect of shrinkage and load-induced cracking on water permeability of concrete. *Materials Journal*, 96(2):234–241.

[Hegger and Voss, 2008] Hegger, J. and Voss, S. (2008). Investigations on the bearing behaviour and application potential of textile reinforced concrete. *Engineering structures*, 30(7):2050–2056.

[Herwegh et al., 2006] Herwegh, M., Zurbriggen, R., Scrivener, K., De Gasparo, A., Kighelman, J., and Jenni, A. (2006). A comparison between tile adhesive mortars (cta) and self-leveling compounds (slc): What can we learn about the role of polymers in thin-bed mortars? *Proceedings of the 16th IBAUSIL, Weimar, paper*, pages 2–1059.

[Hilaire, 2014] Hilaire, A. (2014). Étude des déformations différées des bétons en compression et en traction, du jeune âge au long terme. *Application aux enceintes de confinement. These de doctorat, École normale supérieure de Cachan.*

[Hild and Roux, 2008] Hild, F. and Roux, S. (2008). Correliq4: A software for finite element displacement field measurements by digital image correlation. *Rapport interne LMT Cachan*, 269:195.

[Homoro et al., 2020] Homoro, O., Michel, M., and Baranger, T. (2020). Improvement of the mechanical properties of a glass multifilament yarn reinforced ettringitic matrix using an innovative pre-impregnation process. *European Journal of Environmental and Civil Engineering*, pages 1–16.

[Honorio et al., 2018] Honorio, T., Brochard, L., and Bary, B. (2018). Statistical variability of mechanical fields in thermo-poro-elasticity: Multiscale analytical estimations applied to cement-based materials at early-age. *Cement and Concrete Research*, 110:24–41.

[Honorio et al., 2022] Honorio, T., Carasek, H., and Cascudo, O. (2022). Water self-diffusion in csh: Effect of confinement and temperature studied by molecular dynamics. *Cement and Concrete Research*, 155:106775.

[Honorio et al., 2021] Honorio, T., Maaroufi, M., Al Dandachli, S., and Bourdot, A. (2021). Ettringite hysteresis under sorption from molecular simulations. *Cement and Concrete Research*, 150:106587.

[Hordijk and Reinhardt, 1990] Hordijk, D. and Reinhardt, H. (1990). Fracture of concrete in uniaxial tensile experiments as influenced by curing conditions. *Engineering Fracture Mechanics*, 35(4-5):819–826.

[Houst, 1997] Houst, Y. F. (1997). Carbonation shrinkage of hydrated cement paste. In *Proc. 4th CANMET/ACI International Conference on Durability of Concrete*, number CONF, pages 481–491. CANMET, Ottawa, Canada.

[Hwa, 1964] Hwa, J. C. (1964). Mechanism of film formation from latices. phenomenon of flocculation. *Journal of Polymer Science Part A: General Papers*, 2(2):785–796.

[Idiart, 2009] Idiart, A. E. (2009). *Coupled analysis of degradation processes in concrete specimens at the meso-level*. Universitat Politècnica de Catalunya.

[Jayatilaka, 1979] Jayatilaka, A. d. S. (1979). *Fracture of engineering brittle materials*. Applied Science Publishers.

[Jézéquel and Collin, 2007] Jézéquel, P.-H. and Collin, V. (2007). Mixing of concrete or mortars: dispersive aspects. *Cement and Concrete Research*, 37(9):1321–1333.

[Joshi and Butola, 2013] Joshi, M. and Butola, B. (2013). Application technologies for coating, lamination and finishing of technical textiles. In *Advances in the dyeing and finishing of technical textiles*, pages 355–411. Elsevier.

[Julija, 2020] Julija (2020). Innorenew coe: Flax textile to make concrete more eco-friendly.

[Justnes and Øye, 1990] Justnes, H. and Øye, B. (1990). The microstructure of polymer cement mortars. *Nordic concrete research*, (9):69–80.

[Kaci, 2021] Kaci, Y. (2021). *Hydratation des liants ternaires à base de GGBS et impact sur les mécanismes de fonctionnement des rétenteurs d'eau.* Theses, Université Paris-Saclay.

[Kardon, 1997] Kardon, J. B. (1997). Polymer-modified concrete. *Journal of Materials in Civil Engineering*, 9(2):85–92.

[Keddie and Routh, 2010] Keddie, J. and Routh, A. F. (2010). *Fundamentals of latex film formation: processes and properties.* Springer Science & Business Media.

[Khayat, 1998] Khayat, K. H. (1998). Viscosity-enhancing admixtures for cement-based materials—an overview. *Cement and Concrete Composites*, 20(2-3):171–188.

[Kinda et al., 2020] Kinda, J., Charpin, L., Thion, R., Adia, J.-L., Bourdot, A., Michel-Ponnelle, S., and Benboudjema, F. (2020). Effect of relative humidity on cement paste: Experimental assessment and numerical modelling. In *RILEM Spring Convention and Conference*, pages 123–130. Springer.

[Knapen and Gemert, 2009] Knapen, E. and Gemert, D. (2009). Effect of under water storage on bridge formation by water-soluble polymers in cement mortars. *Construction and Buildings Materials*, 23:3420–3425.

[Knapen and Van Gemert, 2009] Knapen, E. and Van Gemert, D. (2009). Cement hydration and microstructure formation in the presence of water-soluble polymers. *Cement and concrete Research*, 39(1):6–13.

[Knaus and Bauer-Heim, 2003] Knaus, S. and Bauer-Heim, B. (2003). Synthesis and properties of anionic cellulose ethers: influence of functional groups and molecular weight on flowability of concrete. *Carbohydrate Polymers*, 53(4):383–394.

[Kolodzie, 1980] Kolodzie, S. (1980). Analysis of pore throat size and use of the waxman-smits equation to determine ooip in spindle field, colorado. In *SPE annual technical conference and exhibition.* OnePetro.

[Kroetsch and Wang, 2008] Kroetsch, D. and Wang, C. (2008). Particle size distribution. *Soil sampling and methods of analysis*, 2:713–725.

[Kumar and Bhattacharjee, 2003] Kumar, R. and Bhattacharjee, B. (2003). Porosity, pore size distribution and in situ strength of concrete. *Cement and concrete research*, 33(1):155–164.

[Kvande et al., 2018] Kvande, T., Bakken, N., Bergheim, E., and Thue, J. V. (2018). Durability of etics with rendering in norway—experimental and field investigations. *Buildings*, 8(7):93.

[Köhler, 2008] Köhler, N. (2008). Fortfarande fuktiga fasader—nio månader efter larmet [moisture in façades—nine months afterwards the moisture alarm]. *Byggindustrin: Stockholm, Sweeden*, page 14–19.

[Lachemi et al., 2004] Lachemi, M., Hossain, K., Lambros, V., Nkinamubanzi, P.-C., and Bouzoubaa, N. (2004). Performance of new viscosity modifying admixtures in enhancing the rheological properties of cement paste. *Cement and concrete research*, 34(2):185–193.

[Laubie et al., 2017a] Laubie, H., Monfared, S., Radjai, F., Pellenq, R., and Ulm, F.-J. (2017a). Disorder-induced stiffness degradation of highly disordered porous materials. *Journal of the Mechanics and Physics of Solids*, 106:207–228.

[Laubie et al., 2017b] Laubie, H., Radjai, F., Pellenq, R., and Ulm, F.-J. (2017b). Stress transmission and failure in disordered porous media. *Physical review letters*, 119(7):075501.

[Lerouge, 2019] Lerouge, T. (2019). *Transferts (imbibition, séchage) dans des matériaux biporeux multifonctionnels*. Theses, Université Paris-Est.

[Liao et al., 2001] Liao, P.-S., Chen, T.-S., Chung, P.-C., et al. (2001). A fast algorithm for multilevel thresholding. *J. Inf. Sci. Eng.*, 17(5):713–727.

[Lin and Huang, 2010] Lin, S.-T. and Huang, R. (2010). Effect of viscosity modifying agent on plastic shrinkage cracking of cementitious composites. *Materials and structures*, 43(5):651–664.

[Lisø and Kvande, 2007] Lisø, K. R. and Kvande, T. (2007). *Klimatilpasning av bygninger [Climate Adaptation of Buildings]*. SINTEF byggforsk [Building and Infrastructure].

[Lu et al., 2006] Lu, S., Landis, E., and Keane, D. (2006). X-ray microtomographic studies of pore structure and permeability in portland cement concrete. *Materials and structures*, 39(6):611–620.

[Ma et al., 2020] Ma, X., Carette, J., Benboudjema, F., and Bennacer, R. (2020). Optimization of experiment methodology based on identification of parameters in concrete drying. *Construction and Building Materials*, 256:119421.

[Mainguy, 1999] Mainguy, M. (1999). *Modeles de diffusion non linéaire en milieux poreux. Applications a la dissolution et au séchage des matériaux cimentaires*. PhD thesis, Ecole Nationale des Ponts et Chaussées.

[Mainguy et al., 2001] Mainguy, M., Coussy, O., and Baroghel-Bouny, V. (2001). Role of air pressure in drying of weakly permeable materials. *Journal of engineering mechanics*, 127(6):582–592.

[Malbois, 2019] Malbois, M. (2019). *Analyse multi-echelle des déformations différées dans les matériaux cimentaires sous dessiccation ou réaction sulfatique interne*. PhD thesis, Université Paris-Saclay.

[MaM, 2017] MaM (2017). Markets and markets: Fiberglass fabric market. last accessed 18/04/2022.

[Mauroux, 2011] Mauroux, T. (2011). *Impact du séchage sur les propriétés d'adhérence entre un mortier et un support: influence de l'adjuvantation par des éthers cellulose*. PhD thesis, Université de La Rochelle.

[Mazars, 1984] Mazars, J. (1984). *Application de la mécanique de l'endommagement au comportement non linéaire et à la rupture du béton de structure*. PhD thesis, Universite Pierre et Marie Curie - Paris 6.

[Mechtcherine et al., 2020] Mechtcherine, V., Michel, A., Liebscher, M., Schneider, K., and Großmann, C. (2020). Mineral-impregnated carbon fiber composites as novel reinforcement for concrete construction: Material and automation perspectives. *Automation in Construction*, 110:103002.

[Messori et al., 2018] Messori, M., Nobili, A., Signorini, C., and Sola, A. (2018). Mechanical performance of epoxy coated ar-glass fabric textile reinforced mortar: Influence of coating thickness and formulation. *Composites Part B: Engineering*, 149:135–143.

[Mills, 1960] Mills, R. (1960). Strength-maturity relationship for concrete which is allowed to dry. In *RILEM Int. Symp. on Concrete and Reinforced Concrete in Hot Country, Haîfa, Israël*.

[Mobasher, 2011] Mobasher, B. (2011). *Mechanics of fiber and textile reinforced cement composites*. CRC press.

[MTE, 2020] MTE (2020). Ministère de la transition écologique : Exigences réglementaires thermiques pour les bâtiments existants. last accessed 18/04/2022.

[MTE, 2021] MTE (2021). Ministère de la transition écologique : Plan de rénovation énergétique des bâtiments.

[Mäder et al., 2004] Mäder, E., Plonka, R., Schiekel, M., and Hempel, R. (2004). Coatings on alkali-resistant glass fibres for the improvement of concrete. *Journal of Industrial Textiles - J IND TEXT*, 33:191–207.

[Neville, 2000] Neville, A. N. (2000). *Propriétés des bétons*. Eyrolles.

[Nilica and Harmuth, 2005] Nilica, R. and Harmuth, H. (2005). Mechanical and fracture mechanical characterization of building materials used for external thermal insulation composite systems. *Cement and Concrete Research*, 35(8):1641–1645.

[Ohama, 1998] Ohama, Y. (1998). Polymer-based admixtures. *Cement and concrete composites*, 20(2-3):189–212.

[Ohama, 2020] Ohama, Y. (2020). Properties of concrete-polymer composites. In *Polymers in Concrete*, pages 111–146. CRC Press.

[Ōhama et al., 1964] Ōhama, Y., Ibe, H., Mine, H., and Kato, K. (1964). Cement mortars modified by sb latexes with variable bound styrene. *Rubber Chemistry and Technology*, 37(3):758–769.

[Paiva et al., 2009] Paiva, H., Esteves, L., Cachim, P., and Ferreira, V. (2009). Rheology and hardened properties of single-coat render mortars with different types of water retaining agents. *Construction and Building Materials*, 23(2):1141–1146.

[Paiva et al., 2006] Paiva, H., Silva, L., Labrincha, J., and Ferreira, V. (2006). Effects of a water-retaining agent on the rheological behaviour of a single-coat render mortar. *Cement and Concrete Research*, 36(7):1257–1262.

[Palacios-Munoz et al., 2019] Palacios-Munoz, B., Peuportier, B., Gracia-Villa, L., and López-Mesa, B. (2019). Sustainability assessment of refurbishment vs. new constructions by means of lca and durability-based estimations of buildings lifespans: A new approach. *Building and Environment*, 160:106203.

[Pascal et al., 2004] Pascal, S., Alliche, A., and Pilvin, P. (2004). Mechanical behaviour of polymer modified mortars. *Materials Science and Engineering: A*, 380(1-2):1–8.

[Paul, 1977] Paul, A. (1977). Chemical durability of glasses; a thermodynamic approach. *Journal of materials science*, 12(11):2246–2268.

[Peng, 2009] Peng, C. (2009). *Apports de l'analyse microtomographique dans la modélisation des effets du séchage des matériaux à matrice cimentaire*. PhD thesis, Lille 1.

[Pereira et al., 2018] Pereira, C., de Brito, J., and Silvestre, J. D. (2018). Contribution of humidity to the degradation of façade claddings in current buildings. *Engineering Failure Analysis*, 90:103–115.

[Peschard, 2003] Peschard, A. (2003). *Aspects physico-chimiques de l'interaction ciment-polysaccharides dans les enduits. Effets des polysaccharides sur l'hydratation du ciment*. PhD thesis, Saint-Etienne, EMSE.

[Pihlajavaara, 1974] Pihlajavaara, S. (1974). A review of some of the main results of a research on the ageing phenomena of concrete: Effect of moisture conditions on strength, shrinkage and creep of mature concrete. *Cement and Concrete Research*, 4(5):761–771.

[Pourchez et al., 2009] Pourchez, J., Grosseau, P., and Ruot, B. (2009). Current understanding of cellulose ethers impact on the hydration of c3a and c3a-sulphate systems. *Cement and Concrete Research*, 39(8):664–669.

[Pourchez et al., 2010] Pourchez, J., Grosseau, P., and Ruot, B. (2010). Changes in c3s hydration in the presence of cellulose ethers. *Cement and Concrete Research*, 40(2):179–188.

[Powierza et al., 2019] Powierza, B., Stelzner, L., Oesch, T., Gollwitzer, C., Weise, F., and Bruno, G. (2019). Water migration in one-side heated concrete: 4d in-situ ct monitoring of the moisture-clog-effect. *Journal of Nondestructive Evaluation*, 38(1):1–11.

[Qomi et al., 2021] Qomi, M. J. A., Brochard, L., Honorio, T., Maruyama, I., and Vandamme, M. (2021). Advances in atomistic modeling and understanding of drying shrinkage in cementitious materials. *Cement and Concrete Research*, 148:106536.

[Rampini et al., 2019] Rampini, M. C., Zani, G., Colombo, M., and di Prisco, M. (2019). Mechanical behaviour of trc composites: Experimental and analytical approaches. *Applied Sciences*, 9(7):1492.

[Ren et al., 2018] Ren, W., Yang, Z., Sharma, R., McDonald, S. A., and Mummery, P. M. (2018). Three-dimensional in situ xct characterisation and fe modelling of cracking in concrete. *Complexity*, 2018.

[Riccardi, 2020] Riccardi, F. (2020). *Experimental and numerical investigation of the interaction between concrete and FRP reinforcement anchorages.* PhD thesis, Université Paris-Saclay.

[Roubin et al., 2019] Roubin, E., Ando, E., and Roux, S. (2019). The colours of concrete as seen by x-rays and neutrons. *Cement and Concrete Composites*, 104:103336.

[Saija, 1995] Saija, L. M. (1995). Waterproofing of portland cement mortars with a specially designed polyacrylic latex. *Cement and concrete research*, 25(3):503–509.

[Sakai and Sugita, 1995] Sakai, E. and Sugita, J. (1995). Composite mechanism of polymer modified cement. *Cement and concrete research*, 25(1):127–135.

[Samuelson, 2002] Samuelson, I. (2002). *Fukt och mögelskador Hammarby Sjöstad [Moisture- and Mould Damage in Hammarby Sjøstad].*

[Samuelson et al., 2007] Samuelson, I., Mjörnell, K., and Jansson, A. (2007). Fuktskador i putsade, odränerade träregelväggar[defect on timber framework walls with etics]-lägesrapport oktober 2007.

[Scheffler et al., 2009] Scheffler, C., Gao, S., Plonka, R., Mäder, E., Hempel, S., Butler, M., and Mechtcherine, V. (2009). Interphase modification of alkali-resistant glass fibres and carbon fibres for textile reinforced concrete i: Fibre properties and durability. *Composites Science and Technology*, 69(3-4):531–538.

[Shaker et al., 1997] Shaker, F., El-Dieb, A., and Reda, M. (1997). Durability of styrene-butadiene latex modified concrete. *Cement and concrete Research*, 27(5):711–720.

[Shen and Chen, 2007] Shen, L. and Chen, Z. (2007). Critical review of the impact of tortuosity on diffusion. *Chemical Engineering Science*, 62(14):3748–3755.

[Shim, 2013] Shim, E. (2013). Bonding requirements in coating and laminating of textiles. In *Joining textiles*, pages 309–351. Elsevier.

[Shin and Santamarina, 2011] Shin, H. and Santamarina, J. C. (2011). Desiccation cracks in saturated fine-grained soils: particle-level phenomena and effective-stress analysis. *Géotechnique*, 61(11):961–972.

[Silva and Monteiro, 2006] Silva, D. A. and Monteiro, P. J. (2006). The influence of polymers on the hydration of portland cement phases analyzed by soft x-ray transmission microscopy. *Cement and Concrete Research*, 36(8):1501–1507.

[Silva et al., 2014] Silva, F. d. A., Butler, M., Hempel, S., Toledo Filho, R. D., and Mechtcherine, V. (2014). Effects of elevated temperatures on the interface properties of carbon textile-reinforced concrete. *Cement and Concrete Composites*, 48(Complete):26–34.

[Sing, 1991] Sing, K. S. (1991). Characterization of porous solids: An introductory survey. In *Studies in Surface Science and Catalysis*, volume 62, pages 1–9. Elsevier.

[Singh et al., 2003] Singh, N., Mishra, P., Singh, V., and Narang, K. (2003). Effects of hydroxyethyl cellulose and oxalic acid on the properties of cement. *Cement and Concrete Research*, 33(9):1319–1329.

[Sleiman et al., 2020] Sleiman, H. C., Briffaut, M., Dal Pont, S., Tengattini, A., and Huet, B. (2020). Influence of common simplifications on the drying of cement-based materials up to moderate temperatures. *International Journal of Heat and Mass Transfer*, 150:119254.

[Soleilhet, 2018] Soleilhet, F. (2018). *Etudes expérimentales et numériques des matériaux cimentaires sous sollicitations hydro-mécaniques*. PhD thesis, Université Paris-Saclay (ComUE).

[Soroka, 1979] Soroka, I. (1979). *Portland cement paste and concrete*. Macmillan International Higher Education.

[Stock et al., 2002] Stock, S., Naik, N., Wilkinson, A., and Kurtis, K. (2002). X-ray microtomography (microct) of the progression of sulfate attack of cement paste. *Cement and Concrete Research*, 32(10):1673–1675.

[Stora et al., 2008] Stora, E., Bary, B., and He, Q.-C. (2008). On estimating the effective diffusive properties of hardened cement pastes. *Transport in porous media*, 73(3):279–295.

[Su et al., 1996] Su, Z., Sujata, K., Bijen, J., Jennings, H., and Fraaij, A. (1996). The evolution of the microstructure in styrene acrylate polymer-modified cement pastes at the early stage of cement hydration. *Advanced Cement Based Materials*, 3(3-4):87–93.

[Sujjavanich and Lundy, 1998] Sujjavanich, S. and Lundy, J. R. (1998). Development of strength and fracture properties of styrene-butadiene copolymer latex-modified concrete. *Materials Journal*, 95(2):131–143.

[Sundar, 2020] Sundar, D. (2020). What are the different types of glass fiber?

[Sutton, 2013] Sutton, M. A. (2013). Computer vision-based, noncontacting deformation measurements in mechanics: a generational transformation. *Applied Mechanics Reviews*, 65(5).

[Swanson, 1981] Swanson, B. (1981). A simple correlation between permeabilities and mercury capillary pressures. *Journal of Petroleum Technology*, 33(12):2498–2504.

[Taerwe et al., 2013] Taerwe, L., Matthys, S., et al. (2013). *Fib model code for concrete structures 2010*. Ernst & Sohn, Wiley.

[Tazawa et al., 1995] Tazawa, E.-i., Miyazawa, S., and Kasai, T. (1995). Chemical shrinkage and autogenous shrinkage of hydrating cement paste. *Cement and concrete research*, 25(2):288–292.

[Thiery et al., 2007] Thiery, M., Baroghel-Bouny, V., Bourneton, N., Villain, G., and Stéfani, C. (2007). Modélisation du séchage des bétons: analyse des différents modes de transfert hydrique. *Revue européenne de génie civil*, 11(5):541–577.

[Tlaiji et al., 2020] Tlaiji, T., Vu, X. H., Michel, M., Ferrier, E., and Larbi, A. S. (2020). Physical, chemical and thermomechanical characterisation of glass textile-reinforced concretes (trc): Effect of elevated temperature and of cementitious matrix nature on properties of trc. *Materials Today Communications*, 25:101580.

[Tomičevć et al., 2013] Tomičevć, Z., Hild, F., and Roux, S. (2013). Mechanics-aided digital image correlation. *The Journal of Strain Analysis for Engineering Design*, 48(5):330–343.

[Torrenti, 1987] Torrenti, J.-M. (1987). *Comportement multiaxial du béton: aspects expérimentaux et modélisation*. PhD thesis, Ecole Nationale des Ponts et Chaussées.

[Toutlemonde, 1994] Toutlemonde, F. (1994). *Résistance au choc des structures en béton: du comportement du matériau au calcul des ouvrages*. PhD thesis, Marne-la-vallée, ENPC.

[Tsitova, 2022] Tsitova, A. (2022). *Multiscale experimental and numerical study of creep and microcracking in cementitious materials*. PhD thesis, Université Paris-Saclay.

[Van Brakel and Heertjes, 1974] Van Brakel, J. and Heertjes, P. (1974). Analysis of diffusion in macroporous media in terms of a porosity, a tortuosity and a constrictivity factor. *International Journal of Heat and Mass Transfer*, 17(9):1093–1103.

[Van Gemert et al., 2005] Van Gemert, D., Czarnecki, L., Maultzsch, M., Schorn, H., Beeldens, A., Łukowski, P., and Knapen, E. (2005). Cement concrete and concrete–polymer composites: Two merging worlds: A report from 11th icpic congress in berlin, 2004. *Cement and Concrete Composites*, 27(9-10):926–933.

[Van Vliet and Van Mier, 2000] Van Vliet, M. R. and Van Mier, J. G. (2000). Experimental investigation of size effect in concrete and sandstone under uniaxial tension. *Engineering fracture mechanics*, 65(2-3):165–188.

[Vollpracht et al., 2016] Vollpracht, A., Lothenbach, B., Snellings, R., and Haufe, J. (2016). The pore solution of blended cements: a review. *Materials and Structures*, 49(8):3341–3367.

[Wadsö, 2005] Wadsö, L. (2005). Applications of an eight-channel isothermal conduction calorimeter for cement hydration studies. *Cement international*, (5):94–101.

[Walker and Bloem, 1957] Walker, S. and Bloem, D. L. (1957). Effects of curing and moisture distribution on measured strength of concrete. In *Highway Research Board Proceedings*, volume 36.

[Weyer et al., 2005] Weyer, H., Müller, I., Schmitt, B., Bosbach, D., and Putnis, A. (2005). Time-resolved monitoring of cement hydration: Influence of cellulose ethers on hydration kinetics. *Nuclear Instruments and Methods in Physics Research Section B: Beam Interactions with Materials and Atoms*, 238(1-4):102–106.

[Wittmann, 1968] Wittmann, F. (1968). Surface tension skrinkage and strength of hardened cement paste. *Matériaux et Construction*, 1(6):547–552.

[Wittmann, 1982] Wittmann, F. (1982). Creep and shrinkage mechanisms in creep and shrinkage in concrete structures, edited by zp bazant and fh wittmann.

[Wittmann, 1985] Wittmann, F. H. (1985). Deformation of concrete at variable moisture content. *Mechanics of geomaterials*, pages 425–459.

[Xu et al., 2021] Xu, K., Tremsin, A. S., Li, J., Ushizima, D. M., Davy, C. A., Bouterf, A., Su, Y. T., Marroccoli, M., Mauro, A. M., Osanna, M., et al. (2021). Microstructure and water absorption of ancient concrete from pompeii: An integrated synchrotron microtomography and neutron radiography characterization. *Cement and Concrete Research*, 139:106282.

[Yao et al., 2015] Yao, Y., Silva, F., Butler, M., Mechtcherine, V., and Mobasher, B. (2015). Tension stiffening in textile-reinforced concrete under high speed tensile loads. *Cement and Concrete Composites*, 64:49–61.

[Yin et al., 2015] Yin, S., Xu, S., and Wang, F. (2015). Investigation on the flexural behavior of concrete members reinforced with epoxy resin-impregnated textiles. *Materials and Structures*, 48(1):153–166.

[Yurtdas, 2003] Yurtdas, I. (2003). *Couplage comportement mécanique et dessiccation des matériaux à matrice cimentaire: étude expérimentale sur mortiers*. PhD thesis, Lille 1.

[Yurtdas et al., 2006] Yurtdas, I., Peng, H., Burlion, N., and Skoczylas, F. (2006). Influences of water by cement ratio on mechanical properties of mortars submitted to drying. *Cement and Concrete Research*, 36(7):1286–1293.

[Zakaria et al., 2017] Zakaria, M., Ahmed, M., Hoque, M. M., and Islam, S. (2017). Scope of using jute fiber for the reinforcement of concrete material. *Textiles and Clothing Sustainability*, 2(1):1–10.

[Zdanowicz et al., 2022] Zdanowicz, K., Gebauer, D., Koschemann, M., Speck, K., Steinbock, O., Beckmann, B., and Marx, S. (2022). Distributed fiber optic sensors for measuring strains of concrete, steel, and textile reinforcement: Possible fields of application. *Structural Concrete*.

université PARIS-SACLAY

ÉCOLE DOCTORALE
Sciences mécaniques et énergétiques, matériaux et géosciences (SMEMAG)

Titre: Mécanique des matériaux composites hétérogènes à base cimentaire renforcés par des grilles de fibre de verre

Mots clés: Grille de fibre de verre, Mortier de façade, ITE, Matériaux cimentaires composites, Fissuration, Tomographie aux rayons X

Résumé: De nos jours, l'énergie est devenue un besoin fondamental dont la demande ne cesse de croître. Cette dernière est essentielle pour le bien-être et la survie des humains et sa disponibilité est cruciale pour l'économie et la croissance nationales. Les crises sociales, géopolitiques et écologiques se traduisant respectivement par un manque de confort thermique dans les habitations combiné à des factures d'énergie coûteuses pour les ménages à faible revenu, la dépendance énergétique notamment en termes d'energies fossiles, et le réchauffement climatique, exigent une réduction importante de la consommation d'énergie. En France, les systèmes de chauffage des bâtiments représentent 45% de la consommation totale d'énergie et sont responsables de 27% des émissions de gaz à effet de serre. L'isolation thermique dans laquelle s'inscrit l'Isolation Thermique par l'Extérieur (ITE) permet de réduire considérablement la consommation d'énergie ainsi que les émissions de CO_2 tout en augmentant le confort thermique des habitants et en réduisant leur facture d'énergie. Le mortier de façade renforcé par la grille de fiber de verre est utilisé comme couche de protection externe des ITEs. Cependant, de nombreux défauts peuvent compromettre la performance des ITEs, en particulier la fissuration du mortier de façade. Le mortier à base cimentaire subit des déformations chimiques, thermiques et hydriques qui, lorsqu'elles sont restraintes, induisent des contraintes qui peuvent atteindre la résistance en traction du matériau conduidant à la fissuration du mortier. La grille de fibre de verre est proposée comme une solution pour la fissuration. Le comportement du mortier composite renforcé est une combinaison du comportement de chacun de ses composants, le mortier et la grille de fibre de verre. Le premier est un matériau qui évolue chimiquement et qui peut être affecté par son environnement comme son état hydrique. Le comportement du mortier de façade est donc étudié en fonction de son âge et ses conditions de conservation parmi d'autres paramètres. D'autre part, cette étude vise à comprendre les mécanismes de renfort de la grille de fibre de verre dans le mortier vis-à-vis de la fissuration. Des essais de flexion 3 et 4 points sont réalisés in-situ dans le tomographe à rayons X et plusieurs paramètres de renforcement sont considérés. La tomographie permet de dévoiler le rôle de la grille de fibre de verre sur la localisation et la propagation des fissures dans le mortier renforcé.

université PARIS-SACLAY

ÉCOLE DOCTORALE
Sciences mécaniques et énergétiques, matériaux et géosciences (SMEMAG)

Title: Mechanical behavior of heterogeneous composite materials reinforced by fiber glass mesh
Keywords: Fiberglass mesh, Rendering mortar, Cement-based composite, Cracking, X-ray tomography

Abstract:

In our times, energy has become essential for the welfare and the survival of humans and its availability is crucial for the national economy and growth. The social, geopolitical, and ecological, crises reflected respectively in the lack of thermal comfort in homes combined with expensive energy bills of the low-income households, the energy dependency especially in terms of fossil fuels, and the global warming demand the reduction of the energy consumption. In France, the heating systems of buildings represent 45% of the total energy consumption and are responsible for 27% of greenhouse gas emissions. Thermal insulation including the External Thermal Insulation Composite System (ETICS) has a big impact on the energy consumption and CO_2 emissions increasing, at the same time, the thermal comfort of the residents and decreasing their energy bills. The fiberglass mesh reinforced rendering mortar is used as the external protective layer of ETICS. Many defects may attain the ETICS including the cracking of the rendering mortar. These defects may impair the thermo-mechanical performance of the ETICS. The cement-based mortar undergoes chemical, thermal, and hygral strain which, when restrained, cause stress that may attain the tensile strength of the material and cause the mortar cracking. The fiberglass mesh is proposed as a solution for cracking. The behavior of the composite reinforced mortar is a combination of the behavior of each of its components, the mortar and the fiberglass mesh. The former is a chemically evolving material which may also be affected by other conditions such as its hygral conditions. The behavior of the rendering mortar is thus investigated with respect to its age and its curing conditions among other parameters. In a second part, going further in the comprehension of the reinforced mortar mechanical behavior, this study focuses on the fundamental understanding of the reinforcement mechanisms of the fiberglass mesh within the mortar with respect to cracking. X-ray tomography in-situ 3-point and 4-point bending tests are carried out and several reinforcement parameters are considered. The tomography scans enable unveiling the role of the glass fiber mesh on crack localization and crack propagation in reinforced mortar. This work provides physical insights on the reinforcement mechanisms of fiberglass mesh on mortars contributing to the optimization of the cement-based reinforced composites especially in ETICS.